



저작자표시-비영리-변경금지 2.0 대한민국

이용자는 아래의 조건을 따르는 경우에 한하여 자유롭게

- 이 저작물을 복제, 배포, 전송, 전시, 공연 및 방송할 수 있습니다.

다음과 같은 조건을 따라야 합니다:



저작자표시. 귀하는 원저작자를 표시하여야 합니다.



비영리. 귀하는 이 저작물을 영리 목적으로 이용할 수 없습니다.



변경금지. 귀하는 이 저작물을 개작, 변형 또는 가공할 수 없습니다.

- 귀하는, 이 저작물의 재이용이나 배포의 경우, 이 저작물에 적용된 이용허락조건을 명확하게 나타내어야 합니다.
- 저작권자로부터 별도의 허가를 받으면 이러한 조건들은 적용되지 않습니다.

저작권법에 따른 이용자의 권리는 위의 내용에 의하여 영향을 받지 않습니다.

이것은 [이용허락규약\(Legal Code\)](#)을 이해하기 쉽게 요약한 것입니다.

[Disclaimer](#)

**Ph.D. DISSERTATION**

**Metal-Organic Frameworks Derived  
Heterogeneous Materials: Toward  
High-Performance Electrochemical  
Applications of Aluminum- and  
Lithium-Ion Storage**

**By**

**Kaiqiang Zhang**

**January 2020**

**DEPARTMENT OF MATERIALS SCIENCE AND ENGINEERING**

**COLLEGE OF ENGINEERING**

**SEOUL NATIONAL UNIVERSITY**

# **Metal-Organic Frameworks Derived Heterogeneous Materials: Toward High- Performance Electrochemical Applications of Aluminum- and Lithium-Ion Storage**

Advisor: Prof. Ho Won Jang

by

Kaiqiang Zhang

A thesis submitted to the Graduate Faculty of Seoul National University  
in partial fulfillment of the requirements  
for the Degree of Doctor of Philosophy  
Department of Materials Science and Engineering

January 2020

Approved

by

Chairman of Advisory Committee:

Vice-Advisory Committee:

Advisory Committee:

Advisory Committee:

Advisory Committee:

## Abstract

---

This thesis presents materials design and synthesis of electrodes for electrochemical energy storage applications and of nano-catalysts for hydrogenation of nitroarenes to aminoarenes using different synthesis methods and characterization strategies.

The use of clean energy sources, such as wind energy and solar power, to attain the required sustainability and environmental friendliness is one possible solution toward solving the current fossil fuel energy crisis. However, the sporadic quality of renewable energy is a common obstacle in the use of current clean energy resources. To address this issue, electrochemical batteries and capacitors have been considered as useful solutions for reliable power supply. Thus, several energy storage materials for the applications of Li-ion batteries, Li-ion capacitors, and Al-ion batteries have been introduced with a focus on nano-materials synthesized via wet-chemical methods.

Lithium-ion batteries (LIBs) are considered to be theoretically promising with regard to large-scale energy storage and conversion systems. However, a significant problem is the lack of cost-efficient high-performance cathode materials for LIBs. Prussian blue analogs (PBAs) are attractive electrode material candidates for LIBs and are garnering significant interest due to their tunable pore size and intriguing electrochemical properties.

PBAs formed with hexacyanide linkers have been studied for decades. The framework crystal structure of PBAs mainly benefits from the six-fold coordinated cyano functional groups. In-plane tetracyanonickelate was utilized to engineer an organic linker and design a family of four-fold coordinated PBAs (FF-PBAs;  $\text{Fe}^{2+}\text{Ni}(\text{CN})_4$ ,  $\text{MnNi}(\text{CN})_4$ ,  $\text{Fe}^{3+}\text{Ni}(\text{CN})_4$ ,  $\text{CuNi}(\text{CN})_4$ ,  $\text{CoNi}(\text{CN})_4$ ,  $\text{ZnNi}(\text{CN})_4$ , and  $\text{NiNi}(\text{CN})_4$ ), which showed an interesting two-dimensional (2D) crystal structure. It was found that these FF-PBAs could be utilized as cathode materials of Li-ion batteries, and the Ni/Fe<sup>2+</sup> system exhibited superior electrochemical properties compared to the others with a capacity of 137.9 mA h g<sup>-1</sup> at a current density of 100 mA g<sup>-1</sup>. Furthermore, after a 5000-cycle long-term repeated charge/discharge measurement, the Ni/Fe<sup>2+</sup> system displayed a capacity of 60.3 mA h g<sup>-1</sup> with a coulombic efficiency of 98.8% at a current density of 1000 mA g<sup>-1</sup>. In addition, the capacity of 86.1% was preserved at 1000 mA g<sup>-1</sup> as compared with that at 100 mA g<sup>-1</sup>, implying a good rate capability. These potential capacities can be ascribed to an in situ reduction of Li<sup>+</sup> in the interlayer of Ni/Fe<sup>2+</sup> instead of the formation of other compounds with the host material according to ex situ XRD characterization. These specially designed FF-PBAs are expected to inspire new concepts in electrochemistry and other applications requiring 2D materials.

Afterward, a border-rich iron (Fe<sup>3+</sup>) hexacyanocobaltate (FeHCCo) PBA is synthesized via a facile and low-cost co-precipitation method and evaluated as a cathode material for LIBs. The PBA delivered reversible capacities corresponding to 136 and 57 mAh g<sup>-1</sup> at 0.63 and 6.25 C,

respectively. Furthermore, a lithiation capacity of  $116 \text{ mAh g}^{-1}$  at  $1.25 \text{ C}$  was maintained with a Coulombic efficiency of  $99.6\%$ . The high electrochemical performance can be attributed to the highly reversible open-framework crystal texture of border-rich FeHCCo, which may provide new insights on the application of PBAs as viable electrode materials in rechargeable LIBs.

Furthermore, a PBA, zinc hexacyanocobaltate (ZnHCCo), as the low-cost and high-performance cathode material has been demonstrated for LIBs. The open-framework crystal structure of ZnHCCo contributes toward reversible cation insertion and extraction along with the spontaneous valence change of hosts. Specifically, the as-prepared ZnHCCo exhibits a highly reversible capacity of  $121.5 \text{ mAh g}^{-1}$  at a current density of  $1.25 \text{ C}$ , a superior rate capability of  $60.5 \text{ mAh g}^{-1}$  at  $6.25 \text{ C}$ , and a stable cycling stability with a Coulombic efficiency of  $96.5\%$ . Therefore, the well-crystallized and low-cost ZnHCCo is expected to be a potential cathode material for LIBs used in grid-scale energy storage and conversion systems. In addition, the synthesis process of the electrode material can be readily up scaled using the earth abundant and environmentally benign precursors via a room-temperature wet-chemical method.

Aluminum-ion batteries (AIBs) are regarded as promising candidates for post-lithium-ion batteries due to their lack of flammability and electrochemical performance comparable to other metal-ion batteries. The lack of suitable cathode materials, however, has hindered the

development of high-performing AIBs.

We demonstrated the compatibility of elemental metal NPs as cathode materials for AIBs. Three types of metal NPs (Co@C, Fe@C, CoFe@C) were formed by in-situ growing PBAs (Co[Co(CN)<sub>6</sub>], Fe[Fe(CN)<sub>6</sub>], and Co[Fe(CN)<sub>6</sub>]) on a natural loofa (L) by a room-temperature wet chemical method in aqueous bath, followed by a carbonization process. The employed L effectively formed graphite C-encapsulated metal NPs after heat treatment. The discharge capacity of CoFe@C was superior (372 mAh g<sup>-1</sup>) than others (103 mAh g<sup>-1</sup> for Co@C and 75 mAh g<sup>-1</sup> for Fe@C). The novel design results in CoFe@C with an outstanding long-term charge/discharge cycling performance (over 1,000 cycles) with a Coulombic efficiency of 94.1%. Ex-situ X-ray diffraction study indicates these metal NP capacities are achieved through a solid-state diffusion-limited Al storage process. This novel design for cathode materials is highly significant for the further development of advanced AIBs in the future.

The use of metal oxides as electrode materials has seen great success in lithium-ion batteries. However, this type of electrode materials has been regarded as an improper option for rechargeable AIBs in comparison with sulfides and selenides, and has, thus, been nearly abandoned. Here, we demonstrate the suitability of metal oxides as cathode materials of AIBs, exhibiting high electrochemical activities toward Al-ion storage. We designed economical metal-oxide cathodes (Co<sub>3</sub>O<sub>4</sub>@rGO, Fe<sub>2</sub>O<sub>3</sub>@rGO, and CoFe<sub>2</sub>O<sub>4</sub>@rGO) for AIBs. The

$\text{Co}_3\text{O}_4@\text{rGO}$  displayed superior electrochemical properties, regarding both capacity and lifespan, to the current state-of-the-art cathode material reported by scientific literature. Furthermore, the  $\text{CoFe}_2\text{O}_4@\text{rGO}$  exhibits rational electrochemical capacities and an extremely stable charge/discharge process with an excellent Coulombic efficiency of 99.6%. The proposed study expects to stimulate researchers to focus on the overlooked metal oxides as competitive cathode materials for high performance AIBs.

Sulfur is a cost-efficient material, having distinguished electrochemical properties, and is considered an attractive cathode material for AIBs. Several pioneering reports have shown that aluminum-sulfur batteries (ASBs) exhibit superior electrochemical capacity over other cathode materials for AIBs. However, a rapid decay in the capacity is a huge barrier for their practical applications. Here, we have demonstrated systematically for the first time that the two-dimensional layered materials (e.g.,  $\text{MoS}_2$ ,  $\text{WS}_2$ , and BN) can serve as fixers of S and sulfide compounds during repeated charge/discharge processes; BN/S/C displays the highest capacity of  $532 \text{ mAh g}^{-1}$  (at a current density of  $100 \text{ mA g}^{-1}$ ) compared with the current state-of-the-art cathode material for AIBs. Further, we could improve the life-span of ASBs to an unprecedented 300 cycles with a high Coulombic efficiency of 94.3%; discharge plateaus at  $\sim 1.15 \text{ V}$  vs.  $\text{AlCl}_4^-/\text{Al}$  was clearly observed during repeated charge/discharge cycling. We believe that this work opens up a new method for achieving high-performing ASBs.

Besides metal-ion batteries, metal ion capacitors are another emerging issue. Li-ion storage capacitors having superior energy density are critical for one-time-charge long-term applications. Currently, much research endeavor is directed at enhancing the energy density of hybrid Li-ion capacitors, which incorporate the high energy of conventional Li-ion batteries with the elevated power density of Li-ion supercapacitors. Herein, we prepare orthorhombic  $\text{GdCo}(\text{CN})_6$  as a new PBA, showing that this compound offers excellent energy/power densities ( $605 \text{ Wh kg}^{-1}$  and  $174 \text{ W kg}^{-1}$ , respectively) and features Li-ion storage capacities ( $352$  and  $258 \text{ mAh g}_{\text{electrode}}^{-1}$  at  $100$  and  $1,000 \text{ mA g}^{-1}$ , respectively) that are almost twice higher than those of other cathode materials utilized in hybrid Li-ion capacitors. Thus, the study of  $\text{GdCo}(\text{CN})_6$  not only opens a new gate for the exploration of new-type PBAs, but also provides insights on the use of lanthanides in energy storage applications.

Catalysts are incessantly studied for efficient chemical conversions in industrial products and the development of highly active and selective heterogeneous nanocatalysts via a green and facile method with affordable cost-efficiency has been a challenging proposition. A low-cost nanocomposite catalyst containing copper oxide (CuO) nanoparticles (NPs) on graphene oxide (GO) was fabricated by a facile hydrothermal self-assembly process. The segregated CuO NPs and GO exhibited negligible catalytic activities for the reduction of nitroaromatics. However, their hybrid composite accomplished facile reduction with high conversions for several substituted nitroaromatics in aqueous  $\text{NaBH}_4$  solution; synergetic coupling effect of CuO NPs with GO in the

nanocomposite catalyst provided excellent catalytic activity. The nanocomposite catalyst could be separated from the reaction mixture and recycled consecutively.

Furthermore, we synthesized the reproducible heterogeneous catalyst of GO-supported palladium NPs via a simple and green process. The structure, morphology and physicochemical properties of the synthesized heterogeneous catalyst were characterized by the latest techniques such as high-resolution transmission electron microscopy (TEM), scanning TEM, energy-dispersive X-ray spectroscopy, X-ray diffraction analysis, and X-ray photoelectron spectroscopy. The GO-supported Pd NPs (Pd/GO nanocatalyst) exhibited excellent catalytic activity for the reduction of nitroaromatics to aminoaromatics in aqueous sodium borohydride. The nitroaromatics were converted to corresponding aminoaromatics with high yields (up to 99%) using Pd/GO nanocatalyst in aqueous solution. The hybrid heterogeneous catalyst showed 83% of conversion after six cycles in the reduction of nitrobenzene to aminobenzene. These features ensured the high catalytic activity of the introduced graphene oxide supported Pd nanocatalysts.

Keywords: Nanocatalyst, Reduction, Metal-ion battery, Metal-ion capacitor, Wet chemistry, Prussian blue analog, Metal oxide, Sulfure, Layered material, Lanthanide

**Student Number:** 2017-33502

Kaiqiang Zhang

# Table of Contents

---

<b>Abstract .....</b>	<b>1</b>
<b>Table of Contents .....</b>	<b>9</b>
<b>List of Tables .....</b>	<b>17</b>
<b>List of Figures .....</b>	<b>18</b>
<b>1. Chapter 1 .....</b>	<b>27</b>
<b>1.1. Introduction .....</b>	<b>27</b>
<b>1.1.1. Electrochemical energy storage.....</b>	<b>27</b>
<b>1.1.2. Al-ion battery .....</b>	<b>28</b>
<b>1.1.3. Electrode material characterizations.....</b>	<b>30</b>
<b>1.1.4. References.....</b>	<b>32</b>
<b>1.2. Layered metal-organic framework based on tetracyanonickelate as a cathode material for Li-ion storage</b>	<b>35</b>
<b>1.2.1. Introduction .....</b>	<b>35</b>
<b>1.2.2. Material preparation .....</b>	<b>36</b>
<b>1.2.3. Material characterization .....</b>	<b>37</b>

1.2.4. Results and discussion .....	39
1.2.5. Conclusions .....	49
1.2.6. References.....	50
<b>1.3. Iron hexacyanocobaltate metal-organic framework: highly reversible and stationary electrode material with rich borders for lithium-ion batteries.....</b>	<b>53</b>
1.3.1. Introduction .....	53
1.3.2. Material preparation.....	56
1.3.3. Material characterizations.....	57
1.3.4. Results and discussion .....	59
1.3.5. Conclusions .....	69
1.3.6. References.....	70
<b>1.4. A hybrid energy storage mechanism of zinc hexacyanocobaltate-based metal-organic framework endowing stationary and high-performance lithium-ion storage .....</b>	<b>73</b>
1.4.1. Introduction .....	73

<b>1.4.2. Material preparation</b> .....	75
<b>1.4.3. Material characterizations</b> .....	76
<b>1.4.4. Results and discussion</b> .....	78
<b>1.4.5. Conclusions</b> .....	89
<b>1.4.6. References</b> .....	89
<b>1.5. Coordinating gallium hexacyanocobaltate: Prussian blue-based nanomaterial for Li-ion storage</b> .....	92
<b>1.5.1. Introduction</b> .....	92
<b>1.5.2. Material preparation</b> .....	94
<b>1.5.3. Material characterizations</b> .....	94
<b>1.5.4. Results and discussion</b> .....	96
<b>1.5.5. Conclusions</b> .....	107
<b>1.5.6. References</b> .....	108
<b>1.6. Graphite carbon-encapsulated metal nanoparticles derived from Prussian blue analogs growing on natural loofa as</b>	

<b>cathode materials for rechargeable aluminum-ion batteries</b>	<b>110</b>
<b>1.6.1. Introduction</b> .....	<b>110</b>
<b>1.6.2. Material preparation</b> .....	<b>113</b>
<b>1.6.3. Material characterizations</b> .....	<b>114</b>
<b>1.6.4. Results and discussion</b> .....	<b>116</b>
<b>1.6.5. Conclusions</b> .....	<b>127</b>
<b>1.6.6. References</b> .....	<b>128</b>
<b>1.7. Metal-organic framework-derived metal oxide nanoparticles@reduced graphene oxide composites as cathode materials for rechargeable aluminum-ion batteries</b> .....	<b>131</b>
<b>1.7.1. Introduction</b> .....	<b>131</b>
<b>1.7.2. Materials preparation</b> .....	<b>134</b>
<b>1.7.3. Material characterizations</b> .....	<b>135</b>
<b>1.7.4. Results and discussion</b> .....	<b>136</b>
<b>1.7.5. Conclusions</b> .....	<b>145</b>

1.7.6. References.....	146
<b>1.8. Two-dimensional boron nitride as a sulfur fixer for high performance rechargeable aluminum-sulfur batteries .....</b>	<b>148</b>
1.8.1. Introduction .....	148
1.8.2. Material preparation .....	150
1.8.3. Material characterizations.....	151
1.8.4. Results and discussion .....	152
1.8.5. Conclusions .....	167
1.8.6. References.....	167
<b>1.9. Realization of lithium-ion capacitors with enhanced energy density via the use of gadolinium hexacyanocobaltate as a cathode material .....</b>	<b>170</b>
1.9.1. Introduction .....	170
1.9.2. Material preparation .....	172
1.9.3. Material characterizations.....	172

<b>1.9.4. Results and discussion</b> .....	174
<b>1.9.5. Conclusions</b> .....	187
<b>1.9.6. References</b> .....	188
<b>2. Chapter 2</b> .....	<b>192</b>
<b>2.1. Introduction</b> .....	192
<b>2.1.1. Reduciton of nitro-aromatics to amino-aromatics</b> 192	
<b>2.1.2. Characterizations</b> .....	194
<b>2.1.3. Classification of nanocatalysts</b> .....	195
<b>2.1.4. References</b> .....	196
<b>2.2. Facile synthesis of monodispersed Pd nanocatalysts decorated on graphene oxide for reduction of nitroaromatics in aqueous solution</b> .....	199
<b>2.2.1. Introduction</b> .....	199
<b>2.2.2. Nanocatalyst preparation</b> .....	201
<b>2.2.3. Catalytic characterization</b> .....	202

<b>2.2.4. Material characterization</b> .....	203
<b>2.2.5. Results and discussion</b> .....	204
<b>2.2.6. Conclusions</b> .....	213
<b>2.2.7. References</b> .....	214
<b>2.3. Copper oxide–graphene oxide nanocomposite: efficient catalyst for hydrogenation of nitroaromatics in water</b> .....	217
<b>2.3.1. Introduction</b> .....	217
<b>2.3.2. Nanocatalyst preparation</b> .....	219
<b>2.3.3. Materials characterization</b> .....	220
<b>2.3.4. Catalytic reduction of nitroaromatics</b> .....	221
<b>2.3.5. Results and discussion</b> .....	221
<b>2.3.6. Conclusions</b> .....	228
<b>2.3.7. References</b> .....	229
<b>Acknowledgments</b> .....	232
<b>List of Publications</b> .....	232
<b>Abstract (in Korean)</b> .....	235



## List of Tables

---

Table 1.1. Elemental mass percent in ZnHCCo measured by using XRF.

Table 1.2. A comparison in capacity of Prussian blue and Prussian blue analogous as cathode of lithium-ion batteries.

Table 1.3. Details of Rietveld Refinement parameters for the GaHCCo.

Table 1.4. EA(CHNS) for C, H, N elements and ICP for Co, Ga, and K elements measurements of the as-prepared GaHCCo.

Table 2.1. Heterogeneous reduction of nitroaromatics by Pd/GO nanocatalyst.

Table 2.2. Catalytic comparison studies of known heterogeneous catalysts in the reduction of nitrophenol using NaBH<sub>4</sub>.

Table 2.3. Heterogeneous reduction of substituted nitroaromatics catalyzed by CuO-GO nanocomposite catalyst in aqueous solution.

Table 2.4. Catalytic comparison study of known heterogeneous catalysts in the reduction of nitrophenol.

## List of Figures

---

Figure 1.1. Comparison of the standard potential, cost, and gravimetric capacity of various metal ion batteries.

Figure 1.2. Future insight into practical application of RABs.

Figure 1.3. Raman spectra of the few layered graphene cathode during the (a) charge and (b) discharge processes. (c) In-situ XRD data of the graphite electrode in an aluminum-graphite battery under charging to various voltages at  $-10\text{ }^{\circ}\text{C}$  under  $50\text{ mA g}^{-1}$ . The voltages were in the range of  $1.858\text{--}2.622\text{ V}$  vs.  $\text{AlCl}_4^-$  from the bottom to the top curves. The XRD curves were displaced vertically for clarity. Same color adjacent curves were recorded along a voltage plateau (indicated at the right with graphite staging number), adapted from Refs. [34,35].

Figure 1.4. (a) SEM image, (b) EDX mapping of  $\text{Ni/Fe}^{2+}$ , three dimensional representation of  $\text{Ni/M}$ (transition metal ions) (c) side view and (d) top view, (e) XRD, (f) FT-IR, (g) Raman, and (h) TGA spectra of  $\text{Ni/Fe}^{2+}$ .

Figure 1.5. (a) STEM, (b) EDX mapping, (e) TEM, and (f) HRTEM of  $\text{Ni/Fe}^{2+}$ . (c) STEM, (d) EDX mapping, (g) TEM, and (h) HRTEM of  $\text{Ni/Fe}^{3+}$ . Insets exhibit the diffraction patterns.

Figure 1.6. XPS spectra of (a) wide survey, (b) C 1s, (c) N 1s, (d) O 1s, (e) Ni 2p, and (f) Fe 2p of  $\text{Ni/Fe}^{2+}$ .

Figure 1.7. XANES spectra at Ni K-edge collected from Ni/Ni and  $\text{Ni/Fe}^{2+}$ .

Figure 1.8. (a) CV curve, (b) rate-performance, (c) repeated charge/discharge cycling measurement at  $100\text{ mA g}^{-1}$  of  $\text{Ni/Fe}^{2+}$ . Representative charge/discharge voltage profiles of (d) rate performance and (e) cycling measurements at a current density of  $100\text{ mA g}^{-1}$ . (f) long-term consecutive charge/discharge cycling test at  $1,000\text{ mA g}^{-1}$  of  $\text{Ni/Fe}^{2+}$ .

- Figure 1.9. Electrochemical characterization and analysis for Ni/Fe<sup>2+</sup>: (a) CV curves at different scan rates, (b) response current at different scan rates measured from (a) and the fitting dash line, (c) contribution ratios for capacity at various scan rates.
- Figure 1.10. Ex-situ XRD characterizations collected from Ni/Fe<sup>2+</sup> at charge stages of (a) 2.2, (b) 3.0, (c) 3.7, and (d) 4.5 V. (e) XRD spectra of original Ni/Fe<sup>2+</sup>.
- Figure 1.11. (a) Normal structure of Prussian blue analogous with the face-centered cubic phase. Eight subunits are contained in one unit. (b) Mechanism illustration of Li<sup>+</sup> charge/discharge in Prussian blue analogous.
- Figure 1.12. (a, b) SEM and EDS mapping images of the as-prepared FeHCCo. (c) Epitaxial growth illustration of FeHCCo. (d–g) TEM and HRTEM images, HRXRD pattern, and TGA curve of FeHCCo.
- Figure 1.13. (a) Wide survey, (b) N 1s, (c) C 1s, (d) O 1s, (e) Co 2p, and (f) Fe 2p XPS spectra of the as-prepared FeHCCo.
- Figure 1.14. Electrochemical performances of the assembled half-cells. (a) Cyclic voltammetry curves of FeHCCo with a scan rate of 0.2 mV s<sup>-1</sup>. (b) Rate performance of the as-prepared FeHCCo. (c) Representative charge/discharge voltage profiles of the cathode at C-rates ranging from 0.3 C to 6.25 C. (d and e) Cycling stability test at 0.63 and 1.25 C.
- Figure 1.15. (a) Schematic illustration of the SEI film and conductive agents on the surface of border-rich FeHCCo. (b) EIS spectra of the FeHCCo electrodes (fresh, after the first 1, 2, and 5 cycles), respectively.
- Figure 1.16. (a) Ex-situ HRXRD patterns of FeHCCo at various charge states, the (200) diffraction peak shifts to lower angles with decreases in the charge state. (b) The lattice parameter changes approximately linearly with respect to the discharge state.
- Figure 1.17. Theoretical crystal structure of ZnHCCo, where transition

metal Co and Zn are orderly and alternately arranged in the cubic framework. Co is six-fold carbon-coordinated, while Zn is four-fold nitrogen-coordinated resulting in two unpaired cyanide vacancies. Each unit cell consists of eight-subunit cells ( $\text{Li}^+$  site), which can be occupied by  $\text{Li}^+$  ions. Inset shows the visual image of as-prepared product in an aqueous solution.

Figure 1.18. A series of representative characterizations of as-prepared ZnHCCo: (a) X-ray diffraction pattern, (b) Raman spectrum, (c) FT-IR spectra, (d,e) SEM images (inset shows a visual image of easily up scaled ZnHCCo powder), (f) TEM image, and (g) EDX mapping.

Figure 1.19. (a) EDX mapping and (b) TGA curve of ZnHCCo. (c) Wide survey and (d) respective elemental peaks in XRF spectra of ZnHCCo.

Figure 1.20. (a) Wide-survey scan, (b) C 1s, (c) N 1s, (d) Co 2p, (e) Zn 2p, and (f) O 1s XPS spectra of the ZnHCCo product.

Figure 1.21. (a) Representative cyclic voltammetry curves of the ZnHCCo active material at a scan rate of  $0.2 \text{ mV s}^{-1}$  between 2.2–4.5 V vs  $\text{Li}^+/\text{Li}$ . (b) Rate performance of ZnHCCo at a wide variety of current densities of 1.25–6.25 C in the voltage range of 2.2–4.5 V vs.  $\text{Li}^+/\text{Li}$ . (c) Corresponding charge/discharge voltage profiles of the ZnHCCo. (d) Cycling measurement of as-prepared ZnHCCo at the current density of 1.25 C.

Figure 1.22. (a) Charge/discharge cycling measurement for the naked graphite paper current collector. (b) Corresponding voltage profiles display a negligible capacitive behavior. (c) EIS of fresh electrode and electrode after the first 5 charge/discharge cycles.

Figure 1.23. SEM images of (a) fresh electrode and (b) after the first 5 charge/discharge cycling measurement. It shows an improved porosity for the overall electrode, and well preserved active materials.

Figure 1.24. (a) CV curves of ZnHCCo at various scan rates. (b) Response currents measured in the CV curves at a fixed 3.5 V. (c) contribution distribution for Li<sup>+</sup> storage at different scan rates.

Figure 1.25. (a) Crystal structure (b) FE-SEM image, (c) EDX mapping, (d) TEM images, (e) TGA curve, (f) XRD and Rietveld refinement curves, (g) Raman spectrum, and (h) FT-IR spectrum of the GaHCCo.

Figure 1.26. (a) XRF spectra of the synthesized GaHCCo.

Figure 1.27. (a) Wide-survey and deconvoluted (b) C 1s, (c) N 1s, (d) Co 2p, and (e) Ga 2p XPS spectra of the GaHCCo.

Figure 1.28. (a) CV curves, (b) rate performance, (c) corresponding voltage profiles, (d) dQ/dV curves, (e) long-term repeated cycling test, and (f) representative voltage profiles of the GaHCCo.

Figure 1.29. (a) Ex-situ XRD patterns of GaHCCo at (a) 2.2 V, (b) 3.0 V, (c) 3.6 V, and (d) magnified XRD peaks.

Figure 1.30. XRD pattern of the GaHCCo (a) before and (b) after cycling test. (c) EIS spectrum of the GaHCCo. (d) The charge/discharge cycling measurement of the bare graphite paper current collector.

Figure 1.31. Ex-situ XPS characterizations for the electrode charged at 2.2, 3.0, and 3.6 V.

Figure 1.32. (a) CV curves obtained at various scan rates, (b) response currents at 3.1 V when scanned at different rates, and (c) contribution ratios of capacitive and diffusion-controlled Li-ion storage.

Figure 1.33. Synthesis procedure of the C encapsulated metal NPs.

Figure 1.34. (a) SEM image and (b) EDX mapping of CoHCFE. SEM images of (c) well-cleaned loofa surface; (d) in-situ grown CoHCFE on the loofa surface. (e-h) SEM, STEM, magnified STEM, and TEM images of CoFe@C. (i)

HRTEM of the crystallized CoFe alloy and C layer on the surface. (j,k) EDX mapping of CoFe@C. The CoFe@C was prepared through heating at 900 °C for 5 h.

Figure 1.35. XRD diffraction patterns of (a) L, CoHCCo, and CoHCCo/L, (b) L, FeHCFe, FeHCFe/L, (c) L, CoHCFe, and CoHCFe/L.

Figure 1.36. XRD spectra of carbonized L loaded with (a) CoHCCo, (b) FeHCFe, and (c) CoHCFe at various parameters. (d) Heat-treated naked L without any loading.

Figure 1.37. Raman spectra of (a) Co@C, (b) Fe@C, (c) CoFe@C, and (d) L prepared at diverse carbonization conditions.

Figure 1.38. Deconvoluted XPS spectra of (a) Co 2p for Co@C, (b) Fe 2p for Fe@C, (c) Fe 2p and (d) Co 2p for CoFe@C.

Figure 1.39. (a–c) CV curves and (d–f) corresponding charge/discharge voltage profiles of Co@C, Fe@C, and CoFe@C.

Figure 1.40. (a) Representative charge/discharge voltage profiles of CoFe@C at 1,000 mA g<sup>-1</sup>, (b) assembled pouch cells with CoFe@C as cathode material lighting a blue LED lamp, and (c) long-term repeated charge/discharge cycling measurement of CoFe@C at 1,000 mA g<sup>-1</sup>.

Figure 1.41. Schematic illustration of the synthesis process of metal-oxide NPs@rGO.

Figure 1.42. (a) STEM and EDX mapping, (b) TEM, and (c) HRTEM images of Co<sub>3</sub>O<sub>4</sub>@rGO. (d) STEM, (e) EDX mapping, (f) TEM, and (g) HRTEM images of CoFe<sub>2</sub>O<sub>4</sub>@rGO.

Figure 1.43. XRD peaks of (a) Co<sub>3</sub>O<sub>4</sub> and Co<sub>3</sub>O<sub>4</sub>@rGO, (b) Fe<sub>2</sub>O<sub>3</sub> and Fe<sub>2</sub>O<sub>3</sub>@rGO, and (c) CoFe<sub>2</sub>O<sub>4</sub> and CoFe<sub>2</sub>O<sub>4</sub>@rGO. Raman spectra of (d) Co<sub>3</sub>O<sub>4</sub>@rGO, (e) Fe<sub>2</sub>O<sub>3</sub>@rGO, and (f) CoFe<sub>2</sub>O<sub>4</sub>@rGO.

Figure 1.44. XPS spectra of (a) Co 2p of the Co<sub>3</sub>O<sub>4</sub>@rGO, (b) Fe 2p of the Fe<sub>2</sub>O<sub>3</sub>@rGO, and (c) Co 2p and (d) Fe 2p of the CoFe<sub>2</sub>O<sub>4</sub>@rGO.

Figure 1.45. CV curves of (a)  $\text{Co}_3\text{O}_4@\text{rGO}$ , (b)  $\text{Fe}_2\text{O}_3@\text{rGO}$ , and (c)  $\text{CoFe}_2\text{O}_4@\text{rGO}$  from 0.05–2.2 V vs.  $\text{AlCl}_4^-/\text{Al}$ .

Figure 1.46. Repeated charge/discharge cycling measurement for the  $\text{Co}_3\text{O}_4@\text{rGO}$  at 200  $\text{mA g}^{-1}$ .

Figure 1.47. (a) CV curve of the  $\text{CoFe}_2\text{O}_4@\text{rGO}$  measured within a narrowed potential window of 0.05–1.2 V vs.  $\text{AlCl}_4^-/\text{Al}$ . (b) Representative charge/discharge voltage profiles and (c) capacity values of the  $\text{CoFe}_2\text{O}_4@\text{rGO}$  for continuous charge/discharge at 1,000  $\text{mA g}^{-1}$ .

Figure 1.48. Schematic illustration of the assembled pouch cell-type ASB, with BN supported S cathode material as an example; one-layered BN here is a representative graphical illustration.

Figure 1.49. TEM images of bare (a,b) BN, (c,d) super P, and (e,f) S. Insets depict the electron diffraction patterns.

Figure 1.50. (a) SEM image, (b) EDX mapping, (c,d) EPMA spectra, (e) XRD spectra, and (f) TGA curve of the BN/S/C sample.

Figure 1.51. TGA of the  $\text{MoS}_2/\text{S}/\text{C}$ ,  $\text{MoS}_2/\text{C}$ ,  $\text{S}/\text{C}$ ,  $\text{BN}/\text{S}/\text{C}$ , and  $\text{BN}/\text{C}$  samples demonstrating adequate thermal stability when used as cathode materials for ASBs.

Figure 1.52. CV curves of (a)  $\text{S}/\text{C}$ , (b)  $\text{WS}_2/\text{S}/\text{C}$ , (c)  $\text{MoS}_2/\text{S}/\text{C}$ , and (d)  $\text{BN}/\text{S}/\text{C}$  with a scan rate of 0.5  $\text{mV s}^{-1}$  and potential window of 0.05–2.2 V vs.  $\text{AlCl}_4^-/\text{Al}$ .

Figure 1.53. Repeated galvanostatic charge/discharge cycling measurements for (a)  $\text{S}/\text{C}$ , (b)  $\text{WS}_2/\text{C}$ , (c)  $\text{MoS}_2/\text{C}$ , and (d)  $\text{BN}/\text{C}$  within a potential window of 0.05–2.2 V vs.  $\text{AlCl}_4^-/\text{Al}$ .

Figure 1.54. Long-term repeated charge/discharge cycling measurements for (a)  $\text{MoS}_2/\text{S}/\text{C}$ , (b)  $\text{WS}_2/\text{S}/\text{C}$ , and (c)  $\text{BN}/\text{S}/\text{C}$  at a current density of 100  $\text{mA g}^{-1}$  within a potential window of 0.05–2.2 V vs.  $\text{AlCl}_4^-/\text{Al}$ .

Figure 1.55. (a) Voltage profiles of  $\text{BN}/\text{S}/\text{C}$  at diverse charge/discharge

cycles corresponding Figure 5c. (b) An assembled Al/[EMIM]Cl/AlCl<sub>3</sub>/BN/S/C pouch cell with an open circuit voltage of 1.2 V vs. AlCl<sub>4</sub><sup>-</sup>/Al.

Figure 1.56. Deconvoluted XPS spectra (a) S 2p, (b) N 1s, (c) B 1s, and (d) C 1s of BN/S/C.

Figure 1.57. (a) TEM image, (b) EDX mapping, (c) HRTEM image of BN, and (d) HRTEM image of C in the BN/S/C sample.

Figure 1.58. XRD spectra of BN/S/C discharged to (a,b) 0.05 V vs. AlCl<sub>4</sub><sup>-</sup>/Al and (c,d) 0.7 V vs. AlCl<sub>4</sub><sup>-</sup>/Al. (e) XRD spectra of BN/S/C before and after the repeated charge/discharge cycling measurement. S peak in the fresh electrode disappears after charge/discharge cycling test, while layered BN is well preserved. (f) Magnified XRD spectra of BN/S/C where the formed Al<sub>2</sub>S<sub>3</sub> phase during discharge process is detected.

Figure 1.59. (a) Theoretical crystal structure of GdHCCo, with pink spheres representing cavities for Li-ion intercalation. (b) FE-SEM image of a GdHCCo particle revealing an orthorhombic crystal structure. (c) XRD pattern of GdHCCo, with standard peaks represented by red lines. (d) TEM image of GdHCCo. (e) FT-IR spectrum of GdHCCo, with the magnified C≡N stretching peak shown in the inset. The observed peak splitting demonstrates the co-existence of Co<sup>2+/3+</sup>. (f) Raman spectrum of GdHCCo showing Co<sup>3+</sup>-CN and Co<sup>2+</sup>-CN peaks. (g-i) STEM image and representative elemental mapping images of a GdHCCo crystal.

Figure 1.60. TGA curve of the as-prepared GdHCCo.

Figure 1.61. (a) C, (b) N, (c) Gd, and (d) Co XPS spectra of GdHCCo.

Figure 1.62. Electrochemical study of GdHCCo as a half-cell cathode. (a) CV curve, (b) rate performance, (c) charge/discharge curves at various current densities, (d) evolution of capacity upon repeated charge/discharge cycling at 100 mA g<sup>-1</sup> for 250 cycles, (e) evolution of capacity upon repeated

charge/discharge cycling at  $1,000 \text{ mA g}^{-1}$  for 1,000 cycles, inset shows the half-cell lighting a blue LED.

Figure 1.63. Representative charge/discharge voltage profiles of the GdHCCo cathode measured at  $1,000 \text{ mA g}^{-1}$  for 1,000 cycles.

Figure 1.64. XRD patterns of GdHCCo recorded before and after long-term charge/discharge cycling at  $1,000 \text{ mA g}^{-1}$  for 1000 cycles.

Figure 1.65. Dependence of (a) capacitance and (b) capacity on current density for GdHCCo and other cathode materials utilized in Li-ion capacitors. (c) Position of Li/GdHCCo and the estimated corresponding full cell on the energy density–power density map.

Figure 1.66. Electrochemical impedance spectrum of a fresh GdHCCo electrode in an assembled half-cell. Inset shows an expansion of the red-box-marked area.

Figure 1.67. (a) CV curves of GdHCCo recorded at various scan rates ( $0.5\text{--}2.5 \text{ mV s}^{-1}$ ). (b) Current response measured at  $3.5 \text{ V vs. Li}^+/\text{Li}$  at various scan rates. (c) Surface (blue region) and diffusion (red region) process co-controlled regions of Li-ion storage obtained for a scan rate of  $0.5 \text{ mV s}^{-1}$  scan rate. (d) Relative contributions of the above regions obtained at scan rates of 0.5, 1.0, 1.5, 2.0, and  $2.5 \text{ mV s}^{-1}$ .

Figure 1.68. (a) Charge (purple) and discharge (red) potential curves used to prepare samples charged/discharged at different cutoff voltages. (b) Ex-situ XRD patterns of the prepared samples showing characteristic (021) and (022) peaks.

Figure 2.1. (a) Schematic design for the reduction of nitrobenzene with aqueous  $\text{NaBH}_4$  using nanocatalysts. (b) The classification of various nanocatalysts applied for the reduction of NAs to AAs.

Figure 2.2. Procedure for the synthesis of Pd/GO nanocatalyst.

- Figure 2.3. TEM images of (a) GO, and (b) and (c) Pd/GO nanocatalyst. (d) HRTEM image of Pd/GO nanocatalyst.
- Figure 2.4. XRD patterns of GO and Pd/GO nanocatalyst.
- Figure 2.5. FT-IR spectra of GO and Pd/GO nanocatalyst.
- Figure 2.6. TGA results of GO and Pd/GO nanocatalyst.
- Figure 2.7. XPS analysis of (a) survey scan, and (b) Pd 3d, (c) C 1s, and (d) O 1s for the Pd/GO nanocatalyst.
- Figure 2.8. UV-visible spectra of the catalytic reduction using Pd/GO nanocatalysts. Nitrophenol (1 mmol) was reduced in the presence of NaBH<sub>4</sub> (1.2 mmol) by Pd/GO nanocatalyst (20 μL) in water.
- Figure 2.9. The conversion of nitrobenzene to aminobenzene. Nitrobenzene (1 mmol) was reduced in the presence of NaBH<sub>4</sub> (1.2 mmol) by Pd/GO nanocatalyst (20 μL) in 10 min.
- Figure 2.10. Schematic illustration for the synthesis of the CuO-GO nanocomposite catalyst.
- Figure 2.11. (a) XRD diffraction pattern, (b) Raman spectrum, (c) TGA analysis, and (d) FT-IR spectrum of the CuO-GO nanocomposite catalyst.
- Figure 2.12. (a and d) TEM and STEM images of GO. (b and e) TEM and STEM images of the CuO-GO nanocomposite catalyst. (c) HRTEM image of the CuO-GO nanocomposite catalyst. The inset shows the relevant FFT image. (f) EDX spectrum of the CuO-GO nanocomposite catalyst.
- Figure 2.13. XPS analysis (a) survey scan, (b) C 1s, (c) Cu 2p, and (d) O 1s for the CuO-GO nanocomposite catalyst.
- Figure 2.14. Reuse of the CuO-GO nanocomposite catalyst in the heterogeneous reduction of 4-nitrotoluene. Reaction conditions: 4-nitrotoluene (1 mmol), NaBH<sub>4</sub> (1.2 mmol), catalyst (50 mg), room temperature, aqueous solution, and 30 min. The yields were determined by GC-MS.

# 1. Chapter 1

## Electrochemical energy storage

### 1.1. Introduction

#### 1.1.1. Electrochemical energy storage

With ever-increasing environmental concerns and the depletion of fossil energy resources, the discovery of newer and renewable energy sources has become an urgent issue.<sup>[1]</sup> The use of clean energy sources, such as wind energy and solar power, to attain the required sustainability and environmental friendliness is one possible solution toward solving the current fossil fuel energy crisis.<sup>[2]</sup> However, the sporadic quality of renewable energy is a common obstacle in the use of current clean energy resources.<sup>[3]</sup> To address this issue, batteries have been considered as useful energy storage solutions for reliable power supply, playing an important role, which motivates the further improvement of their performance.<sup>[4-8]</sup> Li-ion batteries have seen tremendous development; however, the shortage of lithium metal resources and its high cost have restricted their large-scale application.<sup>[9,10]</sup> To address this problem, alternatives to lithium ion batteries, such as Zn-, Na-, Mg-, and Al-ion batteries have received significant attention.<sup>[11-22]</sup> Among these candidates, Na-ion batteries have an attractive low-cost advantage. However, the lack of reliable safety is one main obstacle. In addition, the shortage of promising electrode materials for aforementioned metal-ion batteries is another hindrance for massive application.

### 1.1.2. Al-ion battery

It is worth noting that Al, as one of the most abundant metallic element in the Earth's crust, enables three-electron charge density which exhibits promising theoretical capacities of  $2978 \text{ mAh g}^{-1}$  and  $8034 \text{ mAh cm}^{-3}$  (Figure 1.1).<sup>[23]</sup> Rechargeable Al batteries (RABs) are considered to be the next generation batteries for energy conversion and storage systems owing to the following advantages. The main benefit is the low cost of Al metal (Figure 1.1), not only because it is one of the most abundant metals but also in view of the maturity of smelting technology; lower cost is one of the critical factors that affects the practical application. Another plus point is the highly reliable safety feature. This does not mean that Al metal is inert; it has a standard electrode potential of  $-1.66 \text{ V}$  vs.  $\text{H}^+/\text{H}$  (Figure 1.1).

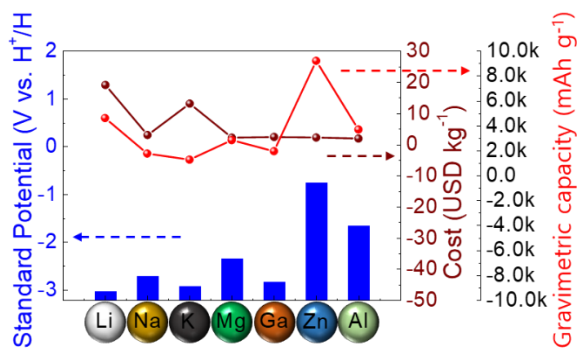


**Figure 1.1.** Comparison of the standard potential, cost, and gravimetric capacity of various metal ion batteries.

Al-ion batteries have been studied since 1800s, with little progress shown owing to the limitations of aqueous electrolytes on potential windows, as well as a lack of suitable cathode materials.<sup>[24–27]</sup> Dai et al.<sup>[28]</sup> applied the combination of a nonflammable ionic liquid ( $\text{AlCl}_3$ /1-ethyl-3-methylimidazolium chloride— $\text{AlCl}_3$ /[EMIm]Cl) electrolyte and a pyrolysis graphite cathode, which exhibited potential stability for over 7000 charge/discharge cycles and excellent rate performance. However, the low capacitance of graphite cathodes (generally below  $120 \text{ mAh g}^{-1}$ ) has made it difficult to achieve further improvement, owing to a limited space for the bulk storage of large-sized ions ( $\text{AlCl}_4^-$ ).<sup>[29]</sup> This drawback has severely hindered the increase in energy density, despite a discharge voltage plateau of approximately 2 V vs.  $\text{AlCl}_4^-/\text{Al}$ .<sup>[30]</sup> To further increase energy density and achieve the practical application of RABs (Figure 1.2), enormous efforts have been expanded in improving the electrochemical properties of cathode materials. Several reviews from diverse viewpoints have summarized the developed cathode materials for RABs that provide insights into the future exploration of high-performance electrode materials.<sup>[31–33]</sup> Zhang et al. synoptically summarized the development of RABs, covering the cell types, oxide layer on the Al anode surface, electrolytes (aqueous/ionic liquid), and cathode materials<sup>[32]</sup> including the charging/discharging principle (intercalation/conversion type) of RABs. Furthermore, Elia et al.<sup>[33]</sup> discussed two types of electrolyte (aqueous and ionic liquid) systems followed by a parallel summary of the reported cathode materials of Al-ion, Al-air, and Al-sulfur batteries. Although these reviews provide

certain guidelines for the development of cathode materials for RABs but any consideration for their extensive application is lacking.

An electrolyte as a medium of ion transfer between anode and cathode and plays a critical role in the overall electrochemical performance. Ionic liquid electrolyte in the RABs exhibits both advantages (e.g., wide potential window) and disadvantages (e.g., high viscosity limiting the rapid migration of ions in the electrolyte). In addition, the direct connection between electrolytes and electrodes (anodes and cathodes) requires a satisfied compatibility at the interfaces.

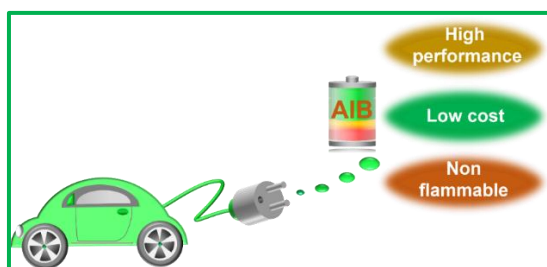


**Figure 1.2.** Future insight into practical application of RABs.

### **1.1.3. Electrode material characterizations**

Material characterization is an inevitable effort in the engineering of cathode materials to analyze synthesized products and assists in the structural modification of materials to improve their electrochemical performance. Herein, the common instruments for the material characterization are X-ray diffraction (XRD) for crystal phase detection, scanning electron microscopy (SEM) and transmission electron

microscopy (TEM) for morphology and micro-lattice observation, and thermogravimetric analysis for heat withstanding performance measurement. In addition, Raman spectrum, ultraviolet (UV) absorption, and Fourier transform infrared spectroscopy (FT-IR) are also employed for specific and special characterization, such as ex-situ or in-situ charge/discharge mechanism exploration. Typically, Raman spectra at different charge/discharge stages depict peak shifts corresponding to ion intercalation, as shown in Figure 1.3a,b.<sup>[34]</sup> During in-situ XRD, a long-range intercalation compound (layers of ions inserted into the graphite between each n-layer graphene) is derived by a staging reaction under the driving force of an electrochemical reaction (Figure 1.3c).<sup>[35]</sup> Thus, a good understanding of the appropriate characterization technology contributes to an in-depth description of the underlying electrochemical mechanisms.

Calculations from first principles are a powerful and useful tool to derive electrochemical properties and explain the electrochemical characteristics of both electrodes and electrolytes.<sup>[36]</sup> Typically, a low diffusion energy barrier for  $\text{AlCl}_4^-$  ion within the cathode material indicates high electrochemical dynamics, which allows improved rate performance. For instance, the calculations show that tetrahedral geometry is preferred over planar geometry in the  $\text{AlCl}_4^-$  ion intercalation into graphite, with a lower energy barrier of 0.77 eV.<sup>[37]</sup> Furthermore, the rate performance can be also enhanced by reducing the film thickness, e.g., to less than five graphene layers.<sup>[38]</sup> Therefore, this method can be useful in exploring new potential cathode materials for RABs.

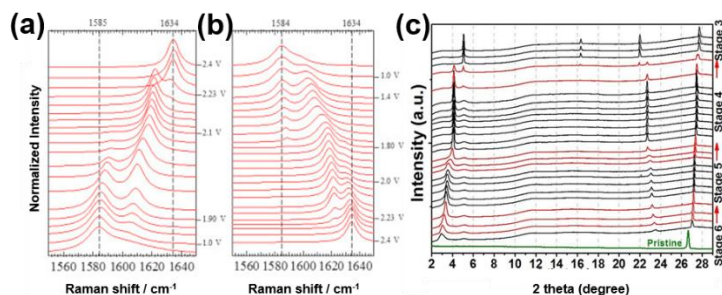


**Figure 1.3.** Raman spectra of the few layered graphene cathode during the (a) charge and (b) discharge processes. (c) In-situ XRD data of the graphite electrode in an aluminum-graphite battery under charging to various voltages at  $-10\text{ }^{\circ}\text{C}$  under  $50\text{ mA g}^{-1}$ . The voltages were in the range of 1.858–2.622 V vs.  $\text{AlCl}_4^-$  from the bottom to the top curves. The XRD curves were displaced vertically for clarity. Same color adjacent curves were recorded along a voltage plateau (indicated at the right with graphite staging number), adapted from Refs. 34,35.

#### 1.1.4. References

- [1] Mellino, S. et al. *Int. J. Hydrogen Energy* 2017, 42, 1830.
- [2] Thackeray, M. M. et al. *Energy Environ. Sci.* 2012, 5, 7854.
- [3] Pasta, M. et al. *Nat. Commun.* 2014, 5, 3007.
- [4] Yu, S. H. et al. *RSC Adv.* 2014, 4, 37365.
- [5] Armand, M. et al. *Nature* 2008, 451, 652.
- [6] Jiang, B. et al. *Angew. Chem. Int. Ed.* 2017, 56, 1869.
- [7] Hu, Y. et al. *Angew. Chem. Int. Ed.* 2015, 54, 4338.
- [8] Larcher, D. et al. *Nat. Chem.* 2015, 7, 19.

- [9] Wessells, C. D. et al. *Nano Lett.* 2011, 11, 5421.
- [10] Zhang, M. et al. *Adv. Mater.* 2018, 30, 1705431.
- [11] Yu, S. H. et al. *RSC Adv.* 2014, 4, 12087.
- [12] Shokouhimehr, M. et al. *Nanosci. Nanotechnol. Lett.* 2013, 5, 770.
- [13] Xia, C. et al. *Adv. Mater.* 2018, 30, 1705580.
- [14] Sun, J. et al. *Nat. Nanotechnol.* 2015, 10, 980.
- [15] Xu, J. et al. *Adv. Mater.* 2015, 27, 2042.
- [16] Wang, S. et al. *Adv. Energy Mater.* 2016, 6, 1502217.
- [17] Canepa, P. et al. *Energy Environ. Sci.* 2015, 8, 3718.
- [18] Pan, B. et al. *Adv. Energy Mater.* 2016, 6, 1600140.
- [19] Tepavcevic, S. et al. *ACS Nano* 2015, 9, 8194.
- [20] Tu, J. et al. *Chem. Commun.* 2018, 54, 1343.
- [21] Wei, J. et al. *J. Mater. Sci. Technol.* 2018, 34, 983.
- [22] Zhang, X. et al. *J. Mater. Chem. A* 2018, 6, 3084.
- [23] Sun, H. et al. *Chem. Commun.* 2015, 51, 11892.
- [24] Hudak, N. S. *J. Phys. Chem. C* 2014, 118, 5203.
- [25] Kaveevivitchai, W. et al. *Small* 2017, 13, 1701296.
- [26] Stadie, N. P. et al. *ACS Nano* 2017, 11, 1911.
- [27] Li, Q. et al. *J. Power Sources* 2002, 110, 1.
- [28] Lin, M.-C. et al. *Nature* 2015, 520, 324.
- [29] Jung, S. C. et al. *J. Phys. Chem. C* 2016, 120, 13384.
- [30] Greco, G. et al. *J. Mater. Chem. A* 2018, 6, 22673.
- [31] Zafar, Z. A. et al. *J. Mater. Chem. A* 2017, 5, 5646.
- [32] Zhang, Y. et al. *Adv. Mater.* 2018, 30, 1706310.

- [33] Elia, G. A. et al. *Adv. Mater.* 2016, 28, 7564.
- [34] Childress, A. S. et al. *Nano Energy* 2017, 39, 69.
- [35] Pan, C. J. et al. *Proc. Natl. Acad. Sci.* 2018, 115, 5670.
- [36] Bhauriyal, P. et al. *Chem-Asian J.* 2017, 12, 1944.
- [37] Gao, Y. et al. *J. Phys. Chem. C* 2017, 121, 7131.
- [38] Jung, S. C. et al. *J. Phys. Chem. C* 2016, 120, 13384.

## 1.2. Layered metal-organic framework based on tetracyanonickelate as a cathode material for Li-ion storage

### 1.2.1. Introduction

Prussian blue analogs (PBAs) are intriguing metal-organic framework (MOF) materials and expected to be utilized on a large-scale for various applications due to their reasonable cost, facile and environment-friendly synthesis, and possessing attractive properties such as electrochemical, gas absorption, and electrochromic, *etc.*<sup>[1-4]</sup> To date, dozens of PBAs and their applications have been reported. Face-centered cubic crystal structures of PBAs are formed by the cyanide linker alternatively and six-fold bridging with single or different transition metal ions. The frameworks formed in the PBAs impart attractive absorption properties, which enable applications requiring high specific area and encapsulation capability such gas absorption<sup>5</sup>, metal ion absorption in batteries, *etc.*<sup>[6-9]</sup> The present precursors for the formation of PBAs are mainly based on hexacyano salts.<sup>[10,11]</sup> The cyanide-based MOFs are more attractive than any other type of MOFs that require an increased cost and/or fussy synthesis (*e.g.*, hydrothermal), together with the inherent contaminated nature of the organic reactants employed during the synthetic processes.<sup>[12,13]</sup>

The PBAs demonstrate tunable electrochemical properties owing to the framework-shaped crystal structure.<sup>[14]</sup> The various reports on PBAs being used as electrode materials of electrochemical batteries reveal their stable electrochemical behaviors in diverse battery systems, including

metal-ion batteries (*e.g.*, Li-, Na-, K-, Al-ion batteries) and metal-air batteries.<sup>[15–19]</sup> For example, Lee *et al.* used vanadium hexacyanoferrate-based PBA as an electrode material for aqueous batteries and achieved a significantly improved capacity by unprecedented dual-ion redox reactions.<sup>[20]</sup> PBAs are also promising as electrode materials in non-aqueous electrolyte-based battery systems. Deng *et al.* employed PBA  $\text{Co}_3[\text{Co}(\text{CN})_6]_2$  as an anode material for K-ion batteries. It was found that this PBA displays a high capacity owing to the solid-state diffusion-limited potassiation/depotassiation processes.<sup>[21]</sup> Instead of directly using the PBAs as electrode materials, Lee *et al.* studied the porous spinel oxides derived from  $\text{Mn}_3[\text{Co}(\text{CN})_6]_2$  serving as electrode material for Zn-air batteries.<sup>[22]</sup> In addition, the cavities inside the PBAs were also shown to be capable of capacitive metal-ion storage.<sup>[23]</sup> These diverse and useful applicability of PBAs make them appropriate potential candidates for battery applications. One common feature for the reported PBAs is the three-dimensional framework determined by the six-fold coordinated precursor, which leads us to consider the possibility of tuning the inherent six-fold coordinated cyanide functional group to develop a different type of PBAs having four-fold tetracyano coordination.

### 1.2.2. Material preparation

The FF-PBAs were synthesized by a co-precipitation method at room temperature by the simultaneous dropwise addition of 100 mL of 0.1 M

FeSO<sub>4</sub>, MnSO<sub>4</sub>, NiSO<sub>4</sub>, ZnSO<sub>4</sub>, CuSO<sub>4</sub>, CoSO<sub>4</sub>, FeCl<sub>3</sub> (Sigma-Aldrich) and 100 mL of 0.01 M K<sub>2</sub>[Ni(CN)<sub>4</sub>] (Sigma-Aldrich) to 200 mL of H<sub>2</sub>O. Precipitates were formed immediately upon dropwise introduction of the solutions. The formed precipitates were separated and rinsed with deionized water several times to remove the impurity ions (such as K<sup>+</sup>). They were subsequently dried in a vacuum oven at 60 °C.

### **1.2.3. Material characterization**

X-ray diffraction (XRD, D8-Advance diffractometer with Cu K $\alpha$  radiation at a fixed incident angle of 2°) was used for structural studies. The surface chemical nature of the formed FF-PBAs was studied by X-ray photoelectron spectroscopy (XPS, PHI 5000 VersaProbe). Ni K-edge X-ray absorption near-edge spectra (XANES) were recorded on the CRG-FAME (BM30B) beamline. The energy of the incident radiation was selected using a pair of Si(220) crystals. Raman spectroscopy (inVia Raman microscope) and Fourier transform infrared (FT-IR, Nicolet iS50) spectroscopy were used for the detection of the cyano functional groups in the products. The morphologies and constitutions were investigated by field emission-scanning electron microscopy (FE-SEM, SUPRA 55VP), transmission electron microscopy (TEM, Tecnai F20), and energy-dispersive X-ray spectroscopy (EDX). Percentages of the constitution elements for each sample were determined from X-ray fluorescence (XRF, ZSX-PRIMUS) studies. Thermogravimetric analysis

(TGA, SDT) was performed under N<sub>2</sub> flow from room temperature to 600 °C with a temperature ramp of 10 °C min<sup>-1</sup>.

A slurry containing FF-PBAs, carbon black (Super P Li), and poly(vinylidene)difluoride (PVDF) in a mass ratio of 7:2:1 was prepared by manually grinding the mixed powders and subsequently dispersing them in *N*-methyl-2-pyrrolidinone (NMP) in a manner similar to previously reports. In addition, prior to the injection of NMP, the mixed powders were sufficiently dried overnight in a vacuum oven at 80 °C and were weighed before and after vacuum drying to ensure the water removal.

A working electrode with a mass loading of ~3 mg cm<sup>-2</sup> was prepared by spreading the slurry on an Al foil current collector, followed by drying it overnight in a vacuum oven at 60 °C.

In order to perform electrochemical measurements, half-cells were prepared using FF-PBA active materials (as the working electrode) and sufficient Li metal flooded with 1.0 M LiPF<sub>6</sub> in a 1:1 mixture (by volume) of ethylene carbonate and diethylene carbonate in an argon-filled glove box with water content less than 5 ppm.

Cyclic voltammetry (CV) measurements were performed with an electrochemical workstation (WBCS3000, Wonatech, Korea) in the potential range of 2.2–4.5 V vs. Li<sup>+</sup>/Li at a scan rate of 0.5 mV s<sup>-1</sup>. Galvanostatic charge/discharge cycling measurements were performed between 2.2–4.5 V vs. Li<sup>+</sup>/Li. Unless otherwise noted, all the current

densities and specific capacities in this report were calculated based on the weight of the FF-PBAs.

The ex-situ characterizations of the Ni/Fe<sup>2+</sup> system discharged to various potentials (2.2, 3.0, 3.7, and 4.5 V) were performed by XRD. The cathodes containing Ni/Fe<sup>2+</sup> were de-assembled from half-cells, followed by thorough rinsing with ethanol and drying in a vacuum oven at 60 °C.

#### **1.2.4. Results and discussion**

Morphologies of the formed FF-PBAs were observed by scanning electron microscopy (SEM) as shown in Figure 1.4a. Plate-like structures were clearly observed for these products, excluding Ni[Ni(CN)<sub>4</sub>] (Ni/Ni) and Ni/Zn. Consistent elements in each product were qualitatively demonstrated by the energy-dispersive X-ray EDX elemental mapping and spectra (Figure 1.4b), displaying uniformly distributed elements over-through each nanoparticle. The layered crystal structures of the FF-PBAs are shown in Figure 1.4c,d; it is evident that the cyanide linkers alternatively bonded with Ni and counter transition metal ions, expanding in two-dimensional space and forming a stacked layered crystal structure. However, Ni/Ni and Ni/Zn displayed particle-shaped products with sizes of ~20 nm and ~300 nm, respectively. Further studies on the crystallization processes of these two FF-PBAs are needed. The crystal structures of the as-prepared FF-PBAs exhibit characteristic diffraction peaks with high intensities in the XRD patterns (Figure 1.4e).

The cyanide functional groups in the FF-PBAs were further verified by Raman and FT-IR spectroscopies (Figure 1.4f,g). The cyanide bridges corresponding to the absorption peak at  $\sim 2120\text{ cm}^{-1}$  in the FT-IR spectra were similar to the cyanide linkers in six-fold coordinated PBAs, and were attributed to the in-plane vibrations of the metal-carbon-nitrogen bond.<sup>[17,24]</sup> The Raman diffraction peak of  $\text{C}\equiv\text{N}$  was also affected by the ambient coordinated transition metal ions. In addition, the presence of both weakly bonded and coordinated water molecules was detected by the appearance of O-H stretching band at approximately  $3500\text{ cm}^{-1}$  in the FT-IR spectrum.<sup>[25]</sup> Ni/Cu, Ni/Co, and Ni/Zn exhibited negligible O-H peaks, suggesting the presence of only a small amount of absorbed water molecules. This result was further verified by the thermal-stability measurements using thermogravimetric analysis TGA; the TGA curves of the three samples showed a slightly drop in the initial stages (low-temperature range). All FF-PBAs were found to be stable until  $400\text{ }^\circ\text{C}$ , although evaporation of different amounts of water molecules for certain samples was observed owing to the absorbed and coordinated water inside the products.

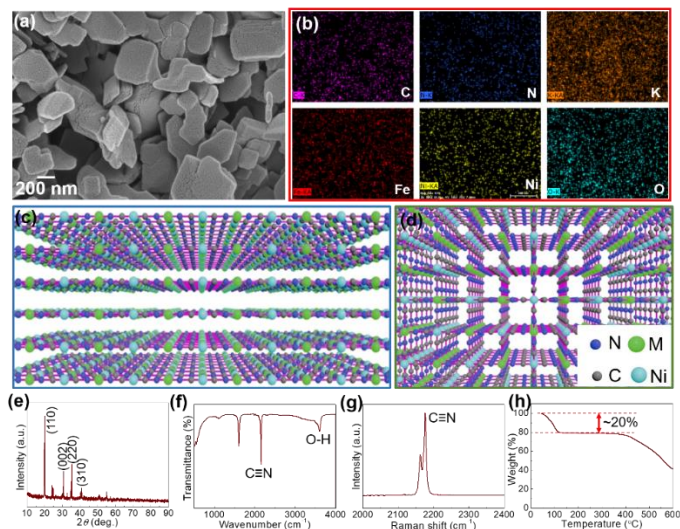


**Figure 1.4.** (a) SEM image, (b) EDX mapping of Ni/Fe<sup>2+</sup>, three dimensional representation of Ni/M(transition metal ions) (c) side view and (d) top view, (e) XRD, (f) FT-IR, (g) Raman, and (h) TGA spectra of Ni/Fe<sup>2+</sup>.

The layered crystal structures were further studied by transmission electron microscopy (TEM, Figure 1.5) for representative Ni/Fe<sup>2+</sup> and Ni/Fe<sup>3+</sup> having the counter transition metal ions with different valence states. The uniform distribution of consistent elements for both Ni/Fe<sup>2+</sup> and Ni/Fe<sup>3+</sup> was further confirmed by EDX mapping (Figure 1.5b,d). Furthermore, the expected two-dimensional crystal structures could be clearly observed in Figure 1.5e,g, where two-dimensional (2D) films with sizes over 200 nm and 500 nm are shown for Ni/Fe<sup>2+</sup> and Ni/Fe<sup>3+</sup>, respectively. It is worth noting that the present 2D materials constructed with transition metal ions are mainly metal sulfides that have

complicated and expensive synthetic processes. However, we used relatively low-cost raw materials for the wet chemical approach in aqueous solution at room temperature, and successfully synthesized large-scale 2D PBAs. This result is expected to inspire further studies on using FF-PBAs for diverse 2D material-based electronic devices. There is however one possible issue relating to the FF-PBAs, i.e., the lamination behavior caused during the separation of the synthesized products from the aqueous bath on drying, considering the different morphologies in the SEM and TEM images. Thus, Ni/Ni and Ni/Zn with sphere-like morphologies were expected because of aggregation during drying. The well-crystallized features for Ni/Fe<sup>2+</sup> and Ni/Fe<sup>3+</sup> were attributed to the oriented lattice with a spacing of 0.4 nm for Ni/Fe<sup>2+</sup> and 0.41 nm for Ni/Fe<sup>3+</sup> and Fast Fourier Transform (FFT) patterns corresponding to a polycrystalline nature. In summary, either trivalent Fe<sup>3+</sup> or bivalent Fe<sup>2+</sup> showed negligible effect on the final crystal structures in the tetracyanonickelate-based FF-PBAs. In other words, the final crystal structure of FF-PBAs was mainly determined by the in-plane four-fold coordinated precursor *e.g.*, Ni(CN)<sub>4</sub><sup>2-</sup>.

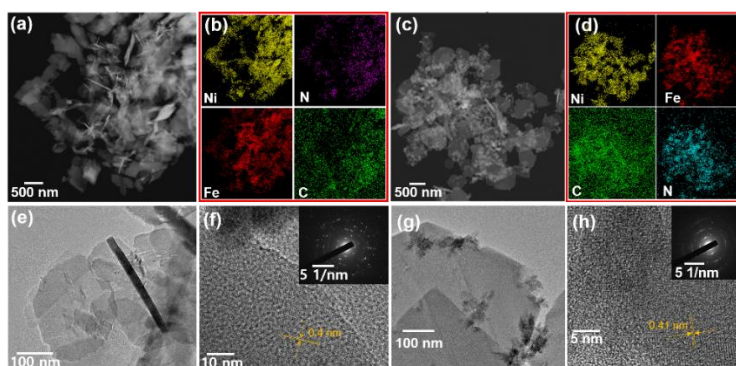


**Figure 1.5.** (a) STEM, (b) EDX mapping, (e) TEM, and (f) HRTEM of Ni/Fe<sup>2+</sup>. (c) STEM, (d) EDX mapping, (g) TEM, and (h) HRTEM of Ni/Fe<sup>3+</sup>. Insets exhibit the diffraction patterns.

The desired molecular formulae of the as-prepared products were K<sub>0.65</sub>Ni[Ni(CN)<sub>4</sub>]<sub>1.25</sub>, K<sub>0.09</sub>Fe<sup>2+</sup>[Ni(CN)<sub>4</sub>]<sub>0.78</sub>, K<sub>0.2</sub>Fe<sup>3+</sup>[Ni(CN)<sub>4</sub>]<sub>1.26</sub>, K<sub>0.2</sub>Co[Ni(CN)<sub>4</sub>]<sub>0.85</sub>, K<sub>0.05</sub>Mn[Ni(CN)<sub>4</sub>]<sub>0.81</sub>, K<sub>0.13</sub>Zn[Ni(CN)<sub>4</sub>]<sub>1.42</sub>, K<sub>0.23</sub>Cu[Ni(CN)<sub>4</sub>]<sub>0.92</sub>, respectively, based on the X-ray fluorescence (XRF) results. The specific calculation was performed by normalizing the stoichiometric number of coordinated transition metal ions (*i.e.*, Ni<sup>2+</sup>, Fe<sup>2+</sup>, Fe<sup>3+</sup>, Co<sup>2+</sup>, Mn<sup>2+</sup>, Zn<sup>2+</sup>, and Cu<sup>2+</sup>) in each deduced molecular formula. Absorbed water molecules were not shown, as they were sensitive to the humidity and temperature of the ambient environment.

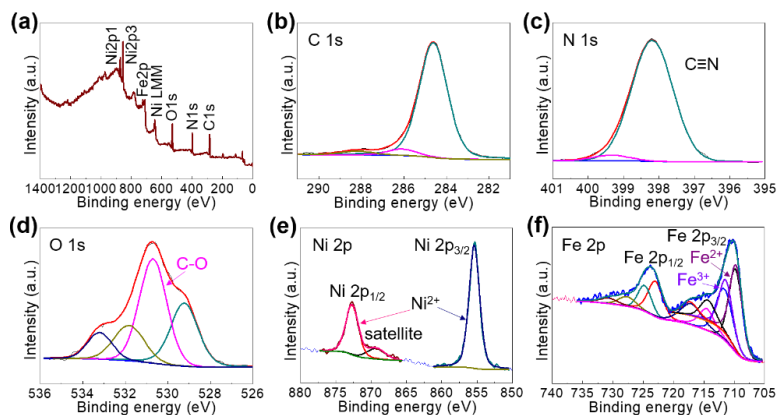


**Figure 1.6.** XPS spectra of (a) wide survey, (b) C 1s, (c) N 1s, (d) O 1s, (e) Ni 2p, and (f) Fe 2p of Ni/Fe<sup>2+</sup>.

The bonding nature of Ni/Fe<sup>2+</sup> was analyzed based on the XPS spectra, where the wide-survey image (Figure 1.6a) clearly showed the binding nature. The cyanide bond in Ni/Fe<sup>2+</sup> was further demonstrated in the XPS spectra (Figure 1.6b,c). The residual water molecules were evident in the deconvoluted O 1s spectra (Figure 1.6d). The deconvoluted Fe 2p XPS spectra of Ni/Fe<sup>2+</sup> (Figure 1.6f) suggested a coexistence of Fe<sup>2+</sup> and Fe<sup>3+</sup>, owing to the electron transfer through the cyanide bridge or coordination to the O or N from environment, which is in consistent with the transitional metal ions in conventional PBAs.<sup>[26]</sup>

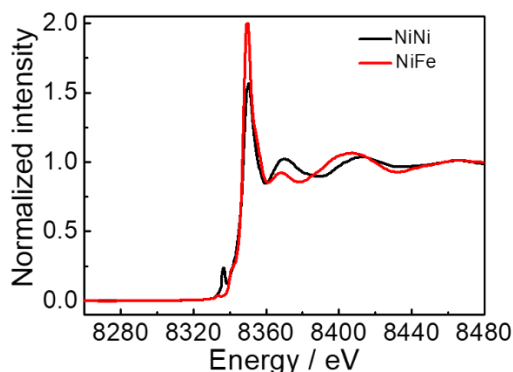


**Figure 1.7.** XANES spectra at Ni K-edge collected from Ni/Ni and Ni/Fe<sup>2+</sup>.

The Ni K-edge X-ray absorption near-edge structure (XANES) spectra for the representative Ni/Fe<sup>2+</sup> and Ni/Ni are depicted in Figure 1.7. It could be clearly observed that the line shapes of the Ni K-edge XANES spectra for Ni/Fe<sup>2+</sup> and Ni/Ni were analogous, typically showing that the electronic and local structures of Ni<sup>2+</sup> were not changed.

The position of the adsorption edge Reflects that the oxidation state of the Ni ions is II.<sup>[27,28]</sup>

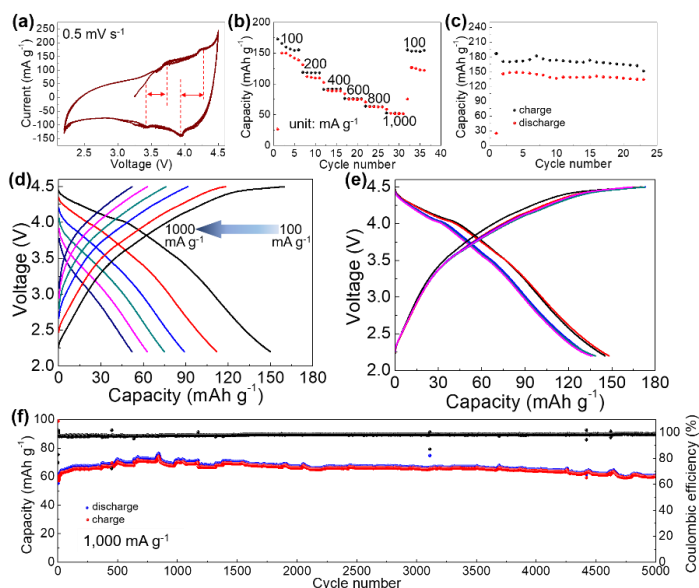


**Figure 1.8.** (a) CV curve, (b) rate-performance, (c) repeated charge/discharge cycling measurement at  $100 \text{ mA g}^{-1}$  of  $\text{Ni/Fe}^{2+}$ . Representative charge/discharge voltage profiles of (d) rate performance and (e) cycling measurements at a current density of  $100 \text{ mA g}^{-1}$ . (f) Long-term consecutive charge/discharge cycling test at  $1,000 \text{ mA g}^{-1}$  of  $\text{Ni/Fe}^{2+}$ .

The electrochemical properties of  $\text{Ni/Fe}^{2+}$  as a cathode material of LIBs were measured in half-cells. Cyclic voltammetry (CV) curves were measured in the potential window of 2.2-4.5 V vs.  $\text{Li}^+/\text{Li}$ , where distortions were absent and raised redox peaks were observed with

hysteresis phenomenon (Figure 1.8a). The subsequent repeated charge/discharge cycling tests were also performed in such a potential window. The rate performance of Ni/Fe<sup>2+</sup> was measured at various current densities of 100, 200, 400, 600, 800, and 1,000 mA g<sup>-1</sup>. The capacity retention at 1,000 mA g<sup>-1</sup> was 43% and a good capacity recovery was achieved (Figure 1.8b) with constant charge/discharge behaviors. The repeated charge/discharge cycling test was performed at 100 mA g<sup>-1</sup>, displaying a competitive discharge capacity of 137.9 mAh g<sup>-1</sup> for Ni/Fe<sup>2+</sup> at the first 20<sup>th</sup> cycle (Figure 1.8c) with constant charge/discharge behaviors, which was considerably superior to that of most other PBAs used as electrode materials.<sup>[9,29,30]</sup> In a controlled experiment, we also performed the repeated charge/discharge cycling tests for other FF-PBAs at the same conditions.

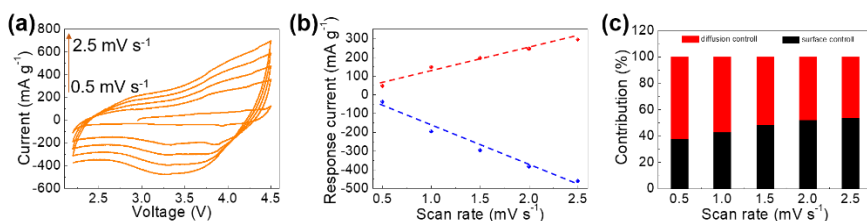


**Figure 1.9.** Electrochemical characterization and analysis for Ni/Fe<sup>2+</sup>: (a) CV curves at different scan rates, (b) response current at different scan rates measured from (a) and the fitting dash line, (c) contribution ratios for capacity at various scan rates.

Long-term charge/discharge stability of the electrode material is critical for practical applications. Therefore, we further subjected the

Ni/Fe<sup>2+</sup> electrode system to a long-term repeated charge/discharge measurement at 1,000 mA g<sup>-1</sup>. A prominent stable charge/discharge process was established with an initial lithiation capacity of 56.8 mAh g<sup>-1</sup> (Figure 1.8f). After the initial activation process, an improved capacity of 64.5 mAh g<sup>-1</sup> as compared with that in the initial range and an extremely high Coulombic efficiency of 98.8% were obtained. After the long-term cycling test, a capacity reserve of 86.1% (as compared with the highest capacity value of 71 mAh g<sup>-1</sup>) was achieved (60.3 mAh g<sup>-1</sup> at the 5,000<sup>th</sup> cycle). This long-term repeated charge/discharge cycling test sufficiently demonstrated the stability of the layered Ni/Fe<sup>2+</sup> PBA when used as a cathode material of LIBs. Further characterization of the high-performance Ni/Fe<sup>2+</sup> system was achieved by electrochemical impedance spectroscopy (EIS).

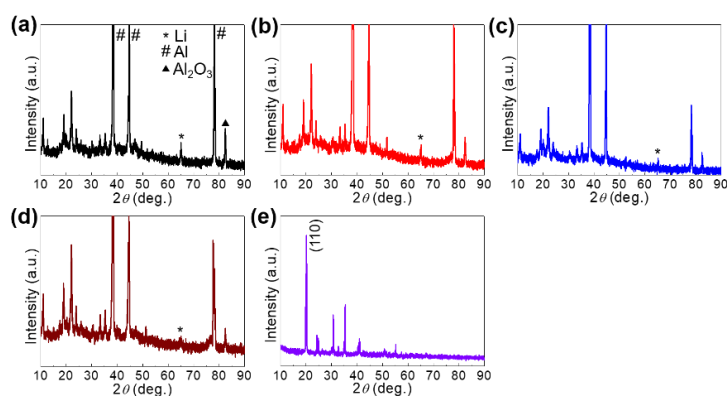


**Figure 1.10.** Ex-situ XRD characterizations collected from Ni/Fe<sup>2+</sup> at charge stages of (a) 2.2, (b) 3.0, (c) 3.7, and (d) 4.5 V. (e) XRD spectra of original Ni/Fe<sup>2+</sup>.

The mechanism for the storage of  $\text{Li}^+$  by  $\text{Ni}/\text{Fe}^{2+}$  was analyzed by CV scans at different scan rates ( $0.5\text{--}2.5\text{ mV s}^{-1}$ ) within the same potential window of  $2.2\text{--}4.5\text{ V}$  vs.  $\text{Li}^+/\text{Li}$  (Figure 1.9a). The curves obtained at all scan rates displayed a well-preserved shape and no obvious distortion. To further disclose this Li-ion storage feature, the dependence of the response current ( $i$ ) on the scan rate ( $v$ ) was modeled by the following power law:<sup>[31,37]</sup>

$$i = av^b \quad (1)$$

It is expected to afford a straight line with slope  $b$  by fitting  $\log(i)$  vs  $\log(v)$ ;  $b = 0.5$  corresponds to diffusion-controlled Li-ion storage, indicating a Faradic electrochemical reaction, while  $b = 1.0$  corresponds to the capacitive Li-ion storage process. Here,  $b$ -values between 0.5 and 1.0 obtained from the deviated fitting line (Figure 1.9b) indicating the co-existence of diffusion- and surface-controlled (capacitive) Li-ion storage processes. The contribution ratios of these storage mechanisms were calculated by deriving Eq. (1) as:

$$i = k_1v + k_2v^{1/2} \quad (2)$$

where  $k_1v$  represents the contribution of the  $b = 1$  case, and  $k_2v^{1/2}$  represents the contribution of the  $b = 0.5$  case. The obtained results are presented in Figure 1.9c, showing that at  $0.5\text{ mV s}^{-1}$ , 62% of the total capacity corresponds to the diffusion-controlled  $\text{Li}^+$  storage. This contribution decreased with the increasing scan rate (46% at  $2.5\text{ mV s}^{-1}$ ), indicating an increased polarization of the electrode at higher scan rates.

Further in-depth study on the charge/discharge mechanism was conducted by ex-situ XRD. During a charge/discharge process, the characteristic peaks of Ni/Fe<sup>2+</sup> at diverse discharge states were well preserved in the XRD spectra (Figure 1.10), demonstrating structural integrity. However, an obvious decrease in the intensity of the (110) peak accompanied by a slight shift toward lower diffraction angles indicated the expansion of layered Ni/Fe<sup>2+</sup> due to the insertion of Li<sup>+</sup>. Accordingly, the Li species in the Ni/Fe<sup>2+</sup> cathode materials at various cutoff potentials was recognized in the ex-situ XRD spectra. It is interesting that the detected Li species in these samples was elemental Li,<sup>[32–36]</sup> as it allowed us to peruse the electrochemical mechanism of the Ni/Fe<sup>2+</sup> PBA in the Li-ion storage process. When Li<sup>+</sup> ions from the electrolyte were inserted into the interlayers of Ni/Fe<sup>2+</sup>, they could be reduced in situ by the incoming electrons instead of forming compounds with the host material. Therefore, the electrochemical reaction of the discharge process can be written as  $\text{Li}^+ + \text{e}^- = \text{Li}$ . Hence, it can be concluded that the Ni/Fe<sup>2+</sup> PBA served as a Li host during the electrochemical process, which may also explain the quasi-rectangular shaped CV curves. This Li-ion storage mechanism is quite similar to that of the conventional PBAs in metal ion capacitors.<sup>[23]</sup>

### 1.2.5. Conclusions

In summary, several tetracyano-based FF-PBAs with layered crystal structures that were quite different from the conventional hexacyano-

based PBAs with framework crystal structures, were synthesized. TEM revealed the two-dimensional features of Ni/Fe<sup>2+</sup> and Ni/Fe<sup>3+</sup>. These innovative layered materials are expected to inspire further study of two-dimensional materials. Ni/Fe<sup>2+</sup> exhibited high stability during repeated charge/discharge cycling as a cathode in LIBs, with a capacity of 60.3 mAh g<sup>-1</sup> and Coulombic efficiency of 98.8% at the 5,000<sup>th</sup> cycle. A good rate capability was achieved; the capacity of 86.1% was preserved at 1,000 mA g<sup>-1</sup> as compared with that at 100 mA g<sup>-1</sup>. The design of FF-PBAs outlined in the present report is expected to pave the path toward the development of low-cost and environment-friendly LIBs in the future.

#### 1.2.6. References

- [1] Xuan, C. et al. ACS Appl. Mater. Inter. 2017, 9, 26134.
- [2] Shokouhimehr, M. et al. J. Mater. Chem. 2010, 20, 5251.
- [3] Shokouhimehr, M. et al. Inorg. Chem. Commun. 2010, 13, 58.
- [4] Han, L. et al. Adv. Mater. 2016, 28, 4601.
- [5] Jiang, Y. et al. Chem. Commun. 2018, 54, 11961.
- [6] Yu, S.-H. et al. RSC Adv. 2014, 4, 12087.
- [7] Yu, S.-H. et al. Rsc Adv. 2014, 4, 37365.
- [8] Shokouhimehr, M. et al. Nanosci. Nanotech. Lett. 2013, 5, 770.
- [9] Yu, S.-H. et al. ECS Electrochem. Lett. 2013, 2, A39.
- [10] Zou, H.-H. et al. Catal. Sci. Technol. 2017, 7, 1549.

- [11] Wang, J.-G. et al. *Nano Energy* 2017, 39, 647.
- [12] Rodenas, T. et al. *Nat. Mater.* 2015, 14, 48.
- [13] Zhao, S. et al. *Nat. Energy* 2016, 1, 16184.
- [14] Han, L. et al. *Adv. Mater.* 2016, 28, 4601.
- [15] Chen, R. et al. *ACS Appl. Mater. Inter.* 2016, 8, 31669.
- [16] Fan, L. et al. *ACS Energy Lett.* 2017, 2, 615.
- [17] Zhang, K. et al. *J. Alloy Compd.* 2019, 791, 911.
- [18] Nie, P. et al. *ACS Appl. Mater. Inter.* 2017, 9, 20306.
- [19] Ren, W. et al. *Nano Lett.* 2017, 17, 4713.
- [20] Lee, J.-H. et al. *Adv. Energy Mater.* 2017, 7, 1601491.
- [21] Deng, L. et al. *Adv. Mater.* 2018, 30, 1802510.
- [22] Lee, J.-S. et al. *Adv. Energy Mater.* 2016, 6, 1601052.
- [23] Li, Z. et al. *Adv. Energy Mater.* 2015, 5, 1401410.
- [24] Xie, M. et al. *J. Power Sources* 2016, 302, 7.
- [25] Xie, M. et al. *Electrochem. Commun.* 2015, 59, 91.
- [26] Xiong, P. et al. *Dalton T.* 2015, 44, 16746.
- [27] Wierzbicki, D. et al. *Int. J. Hydrogen Energ.* 2017, 42, 23548.
- [28] Beale, A. M. et al. *J. Mater. Chem.* 2009, 19, 4391.
- [29] Li, C. H. et al. *RSC Adv.* 2014, 4, 24955.
- [30] Shokouhimehr, M. et al. *Nanosci. Nanotech. Lett.* 2013, 5, 770.
- [31] Shen, L. et al. *Adv. Mater.* 2017, 29, 1700142.
- [32] Wu, M. et al. *J. Power Sources* 2011, 196, 8091.

- [33] Zhang, K. et al. *Electron. Mater. Lett.* 2019, 15, 444.
- [34] Jiang, B. et al. *Prog. Nat. Sci.* 2012, 22, 160.
- [35] Mazinani, B. et al. *JOM* 2019, 71, 1499.
- [36] Ma, G. et al. *Chem. Commun.* 2014, 50, 14209.
- [37] Ding, J. et al. *Energ. Environ. Sci.* 2015, 8, 941.

### **1.3. Iron hexacyanocobaltate metal-organic framework: highly reversible and stationary electrode material with rich borders for lithium-ion batteries**

#### **1.3.1. Introduction**

A significant amount of research is currently focused on the conversion and storage technologies for renewable energy resources (such as solar, wind, and tide) in view of the foreseeable exhaustion of the limited fossil energy resources and the ever-increasing environmental problems associated with fossil energy use.<sup>[1]</sup> However, the location and weather dependence of green and renewable energy makes it imperative to develop energy storage and conversion devices.<sup>[2,3]</sup> Among the diverse options available, rechargeable batteries are potential solutions for energy storage.<sup>[4,5]</sup> Rechargeable lithium-ion batteries (LIBs) have dominated the energy storage market for decades because of their theoretically irreplaceable merits, including high energy and power densities and excellent electrochemical kinetics.<sup>[6,7]</sup> Nevertheless, a low-cost battery electrode material that can be mass-produced and is well matched with the theoretical merits of LIBs is urgently required.

Metal-organic frameworks (MOFs) as multifunctional materials have been widely used in various applications because of their intriguing open-framework crystal structure and electrochemical behaviors.<sup>[8-12]</sup> Prussian blue analogs, in the form of MOFs, have the nominal formula corresponding to  $A_yP[R(CN)_6]_{1-x} \cdot nH_2O$  (A: mobile cations, P:

nitrogen-coordinated transition metal ion, R: carbon-coordinated transition metal ion,  $\square$ :  $[\text{R}(\text{CN})_6]$  vacancies,  $0 \leq y \leq 2$ ,  $0 \leq x \leq 1$ ). They have been described as potential electrode materials for LIBs because of their tunable electrochemical reaction potentials and pore sizes.<sup>[13-16]</sup> In addition, their long lifetime, low cost, and ease of fabrication make the Prussian blue analogs desirable electrode materials for LIBs.<sup>[17-19]</sup> The face-centered cubic crystal structure of the Prussian blue analogs is composed of transition metal ions that are alternately bridged with cyanide ligands (Figure 1.11a).<sup>[20-25]</sup> In the cubic structure, each unit consists of eight subunits (A site, Figure 1.11a) that are occupied by  $\text{Li}^+$  ions with a spontaneous change in the valence state of the hosts (P or R).<sup>[26-29]</sup> Each cyanide-bridged unit can theoretically encapsulate eight or more  $\text{Li}^+$  ions in the subunits (Figure 1.11b). Owing to the intercalation or de-intercalation of  $\text{Li}^+$  ions, lattice strain is generated because of the size and the electrostatic effect between  $\text{Li}^+$  ions and the hosts.<sup>[30]</sup> Consequently, it is essential to examine the structural sustainability of the Prussian blue analogs for the intercalation and de-intercalation processes of  $\text{Li}^+$  ions. Specifically, the channels in the Prussian blue analogs correspond to approximately 3.2 Å for the cyanide bonds and approximately 4.6 Å for the subunits (Figure 1.11a).<sup>[31]</sup> Wide channels are considered to be capable of facilitating easier transport of  $\text{Li}^+$  ions.

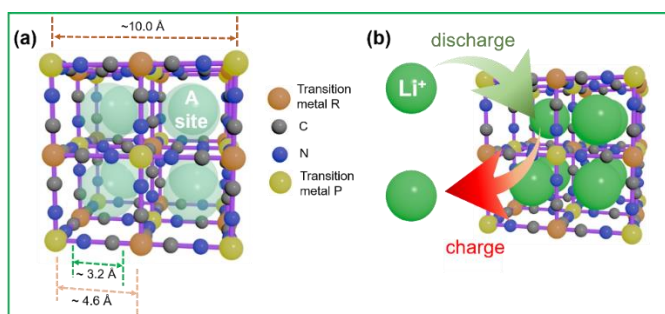


**Figure 1.11.** (a) Normal structure of Prussian blue analogous with the face-centered cubic phase. Eight subunits are contained in one unit. (b) Mechanism illustration of  $\text{Li}^+$  charge/discharge in Prussian blue analogous.

As reported in previous studies, manganese hexacyanomanganate and copper hexacyanoferrate have been established as relatively suitable electrode materials in aqueous electrodes.<sup>[9,30]</sup> Recently, the suitability of Prussian blue analogs as active materials for the next generation of battery electrodes is also proposed.<sup>[32]</sup> For example, the Prussian blue analog  $\text{Co}_3[\text{Co}(\text{CN})_6]_2$  was demonstrated to be an advanced anode material with a high capacity and long life-span for potassium-ion batteries.<sup>[33]</sup> The potential of multifunctional Prussian blue analog composites as promising electrode materials was also demonstrated by other scientific reports. Mao *et al.* demonstrated the high performance of carbon network-reinforced  $\text{Na}_x\text{K}_y\text{MnFe}(\text{CN})_6$  as a cathode for Na-ion batteries, displaying a life-time of over 100 cycles and a capacity of over  $100 \text{ mAh g}^{-1}$ .<sup>[34]</sup> Furthermore, Sun *et al.* demonstrated Mn-Prussian blue analog-reduced graphene oxide to be a superior anode for LIBs, showing

a high capacity of more than 1000 mAh g<sup>-1</sup> and an extremely long life time of over 1400 repeated charge discharge cycles at 10 A g<sup>-1</sup>.<sup>[35]</sup> Indeed, Prussian blue analogs have also been proved to be effective high-performance electrode materials. In a report by Zhang *et al.*, the introduction of polyaniline on the surface of Prussian blue is shown to be an efficient strategy to enhance the electrical conductivity and the kinetics of Na<sup>+</sup> transmission during the repeated charge/discharge process, leading to a higher specific capacity and improved rate performance.<sup>[36]</sup> However, there is inadequate evidence of the suitability of Prussian blue analogs assembled with wide-potential-window organic electrolytes as electrode materials for LIBs. The present study is motivated by the stimulating results obtained recently for the Prussian blue analogs and the existing research gaps. We geared up to demonstrate the suitability of the novel open-framework crystal structure iron (Fe<sup>3+</sup>) hexacyanocobaltate (FeHCCo) as a superior cathode material for LIBs, including the highly reversible feature in Li<sup>+</sup> ion intercalation and de-intercalation processes. The title material can be easily synthesized via a wet-chemical co-precipitation method at room temperature using low-cost precursors.

### **1.3.2. Material preparation**

FeHCCo nanoparticles (NPs) were synthesized by a co-precipitation method involving the simultaneous dropwise addition of 100 ml of FeCl<sub>3</sub> (0.03 M) and 100 ml of K<sub>3</sub>[Co(CN)<sub>6</sub>] (0.03 M) to 100 mL of H<sub>2</sub>O under constant stirring. The resulting yellow precipitation was sonicated for 30

min, and the suspension was allowed to sit for 1 h. The product was separated by centrifugation, rinsed with large amounts of deionized water and ethanol several times, and dried in an oven at 60 °C before use.

### **1.3.3. Material characterizations**

A structural study was performed via high resolution X-ray diffraction (HRXRD, D8-Advance equipped with Cu K $\alpha$  radiation at a fixed incident angle of 2°), X-ray photoelectron spectroscopy (XPS, PHI 5000 VersaProbe) using an Al K $\alpha$  source (Sigma probe, VG Scientifics), Raman spectroscopy (inVia Raman Microscope), and Fourier Transform-Infrared (FT-IR, Nicolet iS50). The morphology and structure were investigated via field emission-scanning electron microscopy (FE-SEM, SUPRA 55VP), transmission electron microscopy (TEM, Tecnai F20), energy-dispersive X-ray (EDX) spectroscopy, and energy disperse spectroscopy (EDS). The constitution of the as-prepared FeHCCo was analyzed via thermogravimetric analysis (TGA, SDT), which was performed under N<sub>2</sub> flow from room temperature to 1000 °C, with a temperature ramp of 10 °C min<sup>-1</sup>, and X-ray fluorescence (XRF, ZSX-PRIMUS).

A slurry containing FeHCCo, carbon black (Super P Li), and poly(vinylidene)difluoride (PVDF) in a mass ratio of 7:2:1 was prepared by manually grinding the materials and subsequently dispersing them in N-methyl-2-pyrrolidinone in a manner similar to the standard slurry preparation method that has been widely deployed in LIB studies by the

research community and manufacturers. Furthermore, prior to the injection of N-methyl-2-pyrrolidinone, the mixed powders were sufficiently dried overnight in a vacuum oven set at 80 °C. Their weight was measured before and after vacuum drying to ensure that water was thoroughly eliminated. A working electrode with a mass loading of approximately 3 mg cm<sup>-2</sup> was prepared by spreading the slurry on a graphite paper current collector, followed by overnight drying in vacuum at 60 °C.

In order to perform electrochemical measurements, a two-electrode half-cell (FeHCCo active material as the working electrode) and sufficient lithium metal (as the Reference electrode) were used to ensure that the capacity was limited solely by the mass of the active material). The system was flooded with 1.0 M LiPF<sub>6</sub> in a 1:1 mixture (by volume) of ethylene carbonate and diethylene carbonate prepared in an argon-filled glove box.

Electrochemical impedance spectroscopy (EIS) analysis of the electrode was performed with an Im6ex ZAHNER impedance measurement instrument in a half-cell. The frequency range used was from 10 mHz to 1 MHz, under a voltage amplitude of 10 mV.

Cyclic voltammetry (CV) measurements were performed on an electrochemical workstation (WBCS3000, Wonatech, Korea) in the potential range of 2.2–4.5 V vs. Li<sup>+</sup>/Li, at a scan rate of 0.2 mV s<sup>-1</sup>. Galvanostatic charge/discharge cycling measurements were performed between 2.2 and 4.5 V vs. Li<sup>+</sup>/Li at various current densities corresponding to 0.63, 1.25, 2.5, 3.75, 5, and 6.25 C. Unless otherwise

specified, all the current densities and specific capacities in the present study were calculated based on the weight of the active material, FeHCCo.

Ex-situ characterizations were performed to examine the interstitial strain and electrochemical reaction mechanism during charge/discharge for the as-prepared FeHCCo. The half-cells at discharged states of 4.5, 4.0, 3.5, 3.0, and 2.5 V were disassembled in an argon-filled glove box. In addition, ex-situ HRXRD characterizations of the electrode plates, coated with slurry, were performed.

#### **1.3.4. Results and discussion**

A morphological study was performed by FE-SEM (Figure 1.12a) and TEM (Figure 1.12d). Border-rich cubic NPs with a size of approximately 200 nm were formed. The constituent elements were verified via EDS (Figure 1.12b). Elements including C, N, Fe, Co, and K were observed throughout each NP in the EDS mapping results, and the wide-survey EDX and XRF results also clearly confirmed the presence of the aforementioned elements.

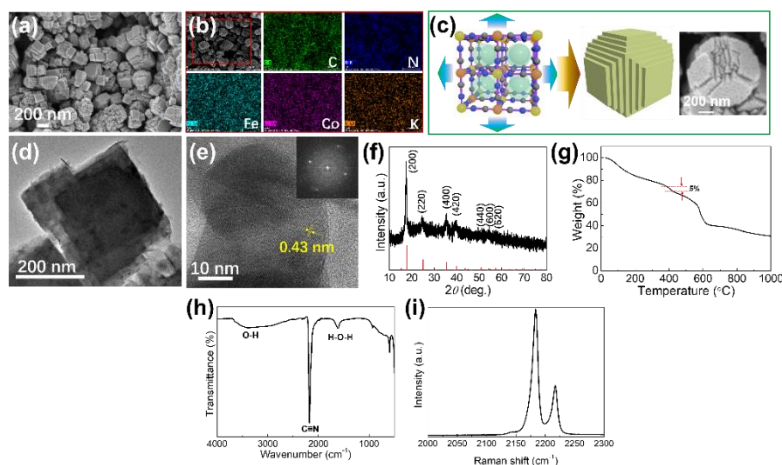


**Figure 1.12.** (a,b) SEM and EDS mapping images of the as-prepared FeHCCo. (c) Epitaxial growth illustration of FeHCCo. (d–g) TEM and HRTEM images, HRXRD pattern, and TGA curve of FeHCCo.

The generation of hierarchical cubic crystals with a rough surface was expected under epitaxial growth during the co-precipitation process, as shown in the mechanical illustration (Figure 1.12c). The small and uniform NPs with a broad surface area are expected to facilitate the trapping of  $\text{Li}^+$  during the rapid charge/discharge process. The TEM image (Figure 1.12d) showed the hierarchical structure in which the semitransparent outer layer was clearly observed. High-resolution TEM (HRTEM) verified that the particles exhibited lattice fringes with a single orientation, which is consistent with the diffraction pattern (Figure 1.12e inset), and thus the as-prepared FeHCCo is confirmed to be highly crystalline. The interplanar spacing measured in HRTEM was 0.45 nm, and this is consistent with the results discussed previously.

A structural study was performed by HRXRD (Figure 1.12f). The diffraction peaks were assigned as face-centered cubic ( $a=b=c=10.2 \text{ \AA}$ ) FeHCCo with the Fm-3m(225) phase group in good agreement with the standard peaks (red vertical lines), and indistinguishable impurity phases were absent. The difference in the lattice parameter was within the margin of error. The broad peaks indicate the nano-sized nature of the as-synthesized products in which the intensity of the (200) diffraction peak exceeds those of other characteristic peaks, thereby demonstrating the preferred growth direction of FeHCCo during the co-precipitation process.

TGA (Figure 1.12g) was conducted from room temperature to  $1000 \text{ }^\circ\text{C}$  with a temperature ramp of  $10 \text{ }^\circ\text{C min}^{-1}$  under a nitrogen flow to examine the thermal stability of the as-prepared FeHCCo. At the initial stage, less weakly bonded zeolitic water was gradually evaporated with an upsurge in the system temperature. The slight weight loss of 5 wt.% at approximately  $450 \text{ }^\circ\text{C}$  corresponds to the release of coordinated water molecules.<sup>[37]</sup> This weight loss in TGA indicated that the content of zeolitic water in FeHCCo was approximately 15 wt.% and enabled the subsequent derivation of the formula for the as-prepared FeHCCo. It should be noted that the zeolitic water in FeHCCo was related to the temperature and moisture of the environment, and thus it was difficult to confirm the accurate water content. The distinct weight loss at approximately  $550 \text{ }^\circ\text{C}$  was ascribed to the decomposition of FeHCCo<sup>[38–40]</sup> and, thereafter, the sample shows a quasi-stable thermal platform until  $1000 \text{ }^\circ\text{C}$ . It should be noted that the decomposition of the

products at approximately 500 °C guarantees stability when they are employed in practical energy storage and conversion systems. Thus, thermal stability analysis via TGA indicated that as-prepared electrode materials are adequate for use in practical batteries for portable and stationary applications.

In order to further verify the cyanide ligand-bridged open framework, FT-IR analysis was performed. The result is shown in Figure 2.12h. Sharp characteristic peaks at 2120  $\text{cm}^{-1}$  were attributed to the in-plane vibrations of the metal-carbon-nitrogen bond.<sup>[41,42]</sup> Additionally, the presence of the cyanide ligand was also verified from the Raman spectrum (Figure 1.12i) wherein evident peaks observed at 2180 and 2215  $\text{cm}^{-1}$  were ascribed to the stretching vibration of  $\text{C}\equiv\text{N}$  of  $\text{FeHCCo}$ .<sup>[43]</sup> In the FT-IR spectrum, the peaks at 1575 and 3400  $\text{cm}^{-1}$  correspond to the characteristic peaks of H-O-H bending and O-H stretching of interstitial water molecules, respectively,<sup>[44]</sup> as confirmed by the TGA result.

The precise composition of the as-prepared  $\text{FeHCCo}$  was deduced based on the TGA result as  $\text{K}_{0.07}\text{Fe}[\text{Co}(\text{CN})_6]_{0.89}\square_{0.11}\cdot 7.5\text{H}_2\text{O}$  based on Fe. When compared with other Prussian blue analogs,<sup>[45-47]</sup> the concentration of hexacyanocobaltate vacancies and potassium impurity in the product were extremely low, and this was expected to expose more interstitial sites for  $\text{Li}^+$  intercalation.

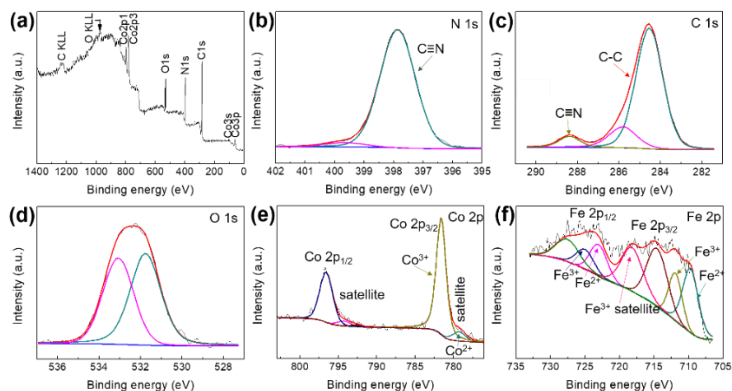


**Figure 1.13.** (a) Wide survey, (b) N 1s, (c) C 1s, (d) O 1s, (e) Co 2p, and (f) Fe 2p XPS spectra of the as-prepared FeHCCo.

The surface chemistry properties and bonding characteristics of the as-prepared FeHCCo were further investigated by X-ray photoelectron spectroscopy (XPS, Figure 1.13). Evident peaks of N 1s, C 1s, O 1s, Co 2p, and Fe 2p further revealed the bonding nature. Oxygen was detected in the products due to the residual water molecules within open-frameworks. The cyanide bond is confirmed in the deconvoluted N 1s spectrum, as shown in the above FT-IR and Raman spectra. Similarly, in the C 1s spectrum, the main peak at 284.6 eV corresponded to the  $sp^2$ -hybridized carbon. In addition, a small peak at 288.4 eV strongly verified the formation of  $C\equiv N$  bonds. The valence state of Co was shown in the high-resolution Co 2p XPS spectrum (Figure 1.13e): two distinct peaks located at binding energies of 781.5 and 796.7 eV were attributed to trivalent Co 2p<sub>3/2</sub> and 2p<sub>1/2</sub>, respectively, and this was accompanied by two evident satellite peaks at 777.2 and 793.8 eV corresponding to  $Co^{2+}$ .

Furthermore, triple-valent Fe 2p<sub>1/2</sub> and 2p<sub>3/2</sub> were assigned to the peaks at 712.1 and 723.2 eV,<sup>[48-50]</sup> and this importantly verified the valance state of Fe in the as-prepared FeHCCo. However, the newly presented Co<sup>2+</sup> and Fe<sup>2+</sup> can be ascribed to the charge transfer between Co<sup>3+</sup> and Fe<sup>3+</sup> sites through the C≡N bridge.<sup>[51]</sup> Nevertheless, it is difficult to fully comprehend the complex phenomenon solely via XPS. The electrochemical performance of the as-prepared FeHCCo as the cathode in LIBs was adequately investigated via cyclic voltammetry at a scan rate of 0.2 mV s<sup>-1</sup> in the voltage range of 2.2–4.5 V vs. Li<sup>+</sup>/Li. Redox peaks in the first five cycles revealed the typical Co redox behavior of the as-prepared FeHCCo with the intercalation of Li<sup>+</sup> cations within the subunits<sup>[52]</sup> and the formation of a solid electrolyte interface film. The charge/discharge process can be rationally analyzed as an electrochemical redox and charge diffusion double-fold controlled charge/discharge process. The redox reaction is thought to combine a Li-ion intercalation-type redox reaction and surficial redox reaction processes. For the purpose of convenience, we performed galvanostatic charge/discharge at a current density of 50 mA g<sup>-1</sup> for 5 cycles, and the obtained mean capacity value (approximately 160 mAh g<sup>-1</sup> as shown in Figure 1.14c, 0.3 C=50 mA g<sup>-1</sup>) corresponded to 1 C.

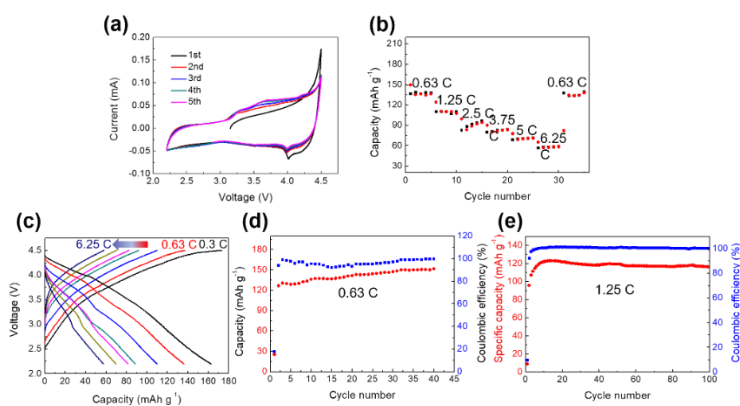


**Figure 1.14.** Electrochemical performances of the assembled half-cells. (a) Cyclic voltammograms of FeHCCo with a scan rate of  $0.2 \text{ mV s}^{-1}$ . (b) Rate performance of the as-prepared FeHCCo. (c) Representative charge/discharge voltage profiles of the cathode at C-rates ranging from 0.3 C to 6.25 C. (d,e) Cycling stability test at 0.63 and 1.25 C.

In order to demonstrate the rate performance, galvanostatic charge/discharge was performed at current densities of 0.63, 1.25, 2.5, 3.75, 5, and 6.25 C in the potential window corresponding to 2.2–4.5 V vs.  $\text{Li}^{+}/\text{Li}$  (Figure 1.14b). FeHCCo delivered reversible capacities of 136, 110, 91, 82, 70, and 57  $\text{mAh g}^{-1}$  at the aforementioned current densities. A capacity retention of 42% (when compared with that of at 0.63 C) was achieved at 6.25 C. The excellent rate capability significantly exceeded those previously reported for MOFs as electrode materials.<sup>[53–55]</sup> The corresponding potential profiles are shown in Figure 1.14c.

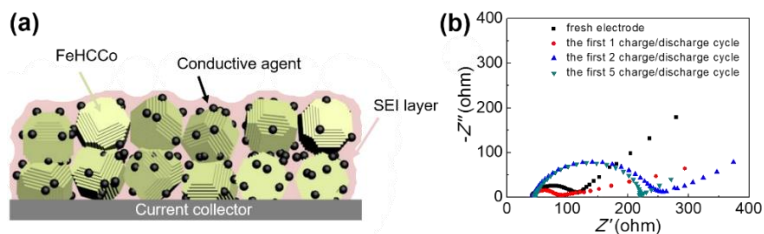


**Figure 1.15.** (a) Schematic illustration of the SEI film and conductive agents on the surface of border-rich FeHCCo. (b) EIS spectra of the FeHCCo electrodes (fresh, after the first 1, 2, and 5 cycles), respectively.

The cycling performances of these products were measured in another two cells assembled with FeHCCo as the working electrode at 0.63 and 1.25 C between 2.2–4.5 V vs.  $\text{Li}^+/\text{Li}$  for 40 and 100 cycles, respectively (Figure 1.14d,e). FeHCCo could deliver lithiation capacities of  $135 \text{ mAh g}^{-1}$  at 0.63 C, and  $121 \text{ mAh g}^{-1}$  at 1.25 C at the 10th cycle. Upon cycling, a lithiation capacity of  $150 \text{ mAh g}^{-1}$  at 0.63 C was maintained after 40 cycles, and that of  $116 \text{ mAh g}^{-1}$  at 1.25 C was maintained after 100 cycles. In the case of charge/discharge at 1.25 C, we excluded the 1st cycle, and the Coulombic efficiency increased from 92.4% at the 2nd cycle to 99.6% at the 6th cycle. It maintained the value in subsequent cycles, thereby indicating a stable SEI film and a highly reversible electrochemical reaction. The capacity value of the bare Prussian blue analogous is relatively less than those of other oxide compounds.<sup>[17–19]</sup> The aforementioned advantageous redox properties are ascribed to advantages including lower vacancy and  $\text{K}^+$  impurity values and a robust

crystal structure. Another possible reason is the unique interface reaction process shown in the schematic illustration (Figure 1.15). The contact surface area between active materials and the conductive agent increased due to the rich boundaries and provided better electron transfer ability for the electrode. Furthermore, active materials with a rough surface can firmly bind with the binder due to the strong interface reaction, and thus were well attached to the current collector. Specifically, the rough surface is expected to improve the wettability at electrode/electrolyte interface to develop a stable and dense ion-conductive and electron-insulative SEI layer, and this aids in preserving the crystal structure of the electrode.<sup>[56-58]</sup> To prove this deduction, the EIS spectra were measured for the fresh electrode, and after the first 1, 2, and 5 charge/discharge cycles, respectively. The recorded data comprised a depressed semi-circle and an oblique line. The depressed semi-circle in high frequency is related to the charge transfer process, where the intercept with the  $Z'$  axis at around 120 Ohm indicates the charge transfer impedance, which is around 80 (120-40) Ohm for the fresh electrode. In the EIS spectra after the first 1 charge/discharge cycle, a smaller charge transfer impedance was observed, which is more likely due to the further infiltration of electrolyte than that in the fresh electrode. With the progress of the charge/discharge process, the EIS spectrum after the first 2 charge/discharge cycles exhibits much larger charge transfer impedance, which can be explained by the formation of the incomplete and uneven ion conductive and electron insulate SEI layer with a rough surface and folds.<sup>[56]</sup> In the fourth EIS spectra, obtained after the first 5

charge/discharge cycles, a decreased charge transfer impedance is observed, which demonstrates the optimization of the SEI layer.

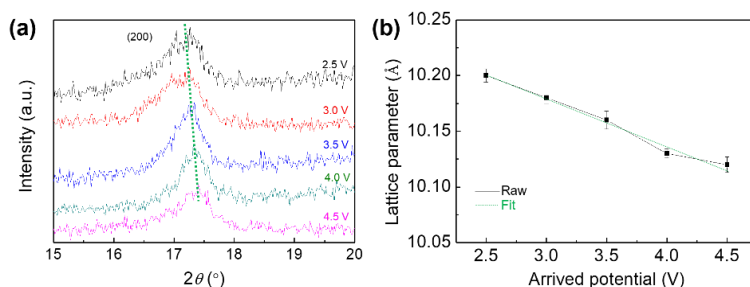


**Figure 1.16.** (a) Ex-situ HRXRD patterns of FeHCCo at various charge states, the (200) diffraction peak shifts to lower angles with decreases in the charge state. (b) The lattice parameter changes approximately linearly with respect to the discharge state.

Interstitial lattice strain generated during the  $\text{Li}^+$  ions insertion (discharge)/extraction (charge) within the as-prepared FeHCCo was adequately investigated by ex-situ XRD (Figure 1.16a). The electrode preparation was fully cycled ten times at 0.3 C and ended at a fully charged state. The electrodes were subsequently discharged to 4.5, 4.0, 3.5, 3.0, and 2.5 V at 0.3 C. Ex-situ XRD spectra (Figure 1.16a) of the electrodes at different charge states revealed that the lattice parameter increased during discharge ( $\text{Li}^+$  insertion), as illustrated by a shift in the position of the (200) diffraction peak to smaller angles. The lattice parameters (Figure 1.16b) as determined from XRD diffraction peaks for each sample (where the error bars denote the standard deviations from

the lattice parameter of each sample) increased as a function of  $x$  in  $\text{Li}_x\text{K}_{0.07}\text{Fe}[\text{Co}(\text{CN})_6]_{0.89}$ , thereby demonstrating isotropic lattice stress during the intercalation of  $\text{Li}^+$  ions. The crystal structure of FeHCCo is well preserved after the cycling measurement. The change in the lattice parameter was less than 1%, and this indicated that FeHCCo readily maintained its integrity after the cycling measurement. The variation in the lattice parameter of FeHCCo during the insertion (lattice expansion) and extraction (lattice shrink) of  $\text{Li}^+$  ions accommodated the volume change during cycling. Despite a tiny local-distortion, the overall unit-cells do not change significantly beyond a minor distortion in the frameworks. FeHCCo benefits from the highly reversible characteristics and exhibits excellent cycling stability and Coulombic efficiency.

### **1.3.5. Conclusions**

In summary, a highly reversible FeHCCo cathode material was fabricated via a facile, low-cost, and scalable co-precipitation chemical approach at room temperature. The results indicated that the border-rich FeHCCo exhibited an electrochemical performance of 136 and 57 mAh  $\text{g}^{-1}$  at 0.63 and 6.25 C, respectively. Upon cycling, lithiation capacities of 116 mAh  $\text{g}^{-1}$  at 1.25 C were maintained after 100 cycles, with a Coulombic efficiency of 99.6%. Isotropic and negligible lattice strains during  $\text{Li}^+$  ion intercalation/extraction compensate for the volume change in the unit-cells and also maintain the integrity of the overall open-framework structure, thereby enabling good cycling stability with

high Coulombic efficiency. The present method to prepare border-rich FeHCCo can be easily scaled-up. This is significant in terms of its use in large-scale energy storage, such as in electric grids. Thus, FeHCCo is presented as a novel and scientifically intriguing material and may be the key to promising developments in the LIB domain.

### 1.3.6. References

- [1] Wang, L. et al. *Angew. Chem. Int. Edit.* 2013, 125, 2018.
- [2] Yang, Z. et al. *Chem. Rev.* 2011, 111, 3577.
- [3] Soloveichik, G. L. et al. *Annu. Rev. Chem. Biomol.* 2011, 2 503.
- [4] Sun, Y. et al. *Nat. Energy* 2016, 1, 16071.
- [5] Pasta, M. et al. *Nat. Commun.* 2014, 5, 3007.
- [6] Yu, S. H. et al. *RSC Adv.* 2014, 4, 37365.
- [7] Mazinani, B. et al. *JOM* 2019, 71, 1499.
- [8] Yu, S. H. et al. *ECS Electrochem. Lett.* 2013, 2, A39.
- [9] Wessells, C. D. et al. *Nat. Commun.* 2011, 2, 550.
- [10] Shokouhimehr, M. et al. *J. Mater. Chem.* 2010, 20, 5251.
- [11] Shokouhimehr, M. et al. *Inorg. Chem. Commun.* 2010, 13, 58.
- [12] Shokouhimehr, M. Kent State University 2010.
- [13] Chen, L. et al. *Chem.-Eur. J.* 2018, 24, 13362.
- [14] Yang, J. et al. *Chem.-Eur. J.* 2017, 23, 631.
- [15] Yang, J. et al. *J. Mater. Chem. A* 2014, 2, 19005.

- [16] Yang, J. et al. *J. Mater. Chem. A* 2014, 2, 16640.
- [17] Shao, J. et al. *Appl. Surf. Sci.* 2019, 471, 745.
- [18] Shao, J. et al. *J. Mater. Sci.-Mater. El.* 2019, 30, 982.
- [19] Zhu, M. et al. *J. Alloys Compd.* 2018, 749, 811.
- [20] Wang, Y. et al. *J. Mater. Chem. A* 2017, 5, 25562.
- [21] Shao, J. et al. *J. Alloys Compd.* 2019, 784, 869.
- [22] Shao, J. et al. *J. Alloys Compd.* 2018, 768, 1049.
- [23] Feng, J. et al. *Int. J. Hydrogen Energ.* 2018, 43, 20538.
- [24] Han, X. et al. *Nanoscale* 2018, 10, 2735.
- [25] Li, Y. et al. *ChemistrySelect* 2018, 3, 13596.
- [26] Huang, S. D. et al. *U.S. Pat.* 2010, 20100254912.
- [27] Neff, V. D. *J. Electrochem. Soc.* 1978, 125, 886.
- [28] McCargar, J. W. et al. *J. Phys. Chem.* 1988, 92, 3598.
- [29] Bie, X. et al. *J. Power Sources* 2018, 378, 322.
- [30] Tealdi, C. et al. *J. Mater. Chem. A* 2016, 4, 6998.
- [31] Huang, S. D. et al. *U.S. Pat.* 2010, 12/710,633.
- [32] Hurlbutt, K. et al. *Joule* 2018, 2, 1950.
- [33] Deng, L. et al. *Adv. Mater.* 2018, 30, 1802510.
- [34] Mao, Y. et al. *Nano Energy* 2019, 58, 192.
- [35] Sun, D. et al. *Carbon* 2019, 143, 706.
- [36] Zhang, Q. et al. *J. Power Sources* 2018, 395, 305.
- [37] You, Y. et al. *J. Mater. Chem. A* 2013, 1, 14061.

- [38] Agnihotry, S. A. et al. *Electrochim. Acta* 2006, 51, 4291.
- [39] Avila, M. et al. *J. Solid State Chem.* 2008, 181, 2899.
- [40] Imanishi, N. et al. *J. Power Sources* 1999, 79, 215.
- [41] Xie, M. et al. *J. Power Sources* 2016, 302, 7.
- [42] Xie, M. et al. *Electrochem. Commun.* 2015, 59, 91.
- [43] Zhang, L. et al. *RSC Adv.* 2017, 7, 50812.
- [44] Zong, Y. et al. *J. Radioanal. Nucl. Ch.* 2017, 311, 1577.
- [45] Yu, S. et al. *J. Power Sources* 2015, 275, 45.
- [46] Trócoli, R. et al. *ChemSusChem* 2015, 8, 481.
- [47] You, Y. et al. *Energ. Environ. Sci.* 2014, 7, 1643.
- [48] Chen, Y. et al. *Phys. Chem. Chem. Phys.* 2015, 17, 14012.
- [49] Tang, R. et al. *Sci. Rep.-UK* 2015, 5, 13645.
- [50] Liu, C. et al. *Sci. Rep.-UK* 2015, 5, 9498.
- [51] Samain, L. et al. *J. Anal. Atom. Spectrom.* 2013, 28, 524.
- [52] Kuwata, N. et al. *Solid State Ionics* 2014, 262, 165.
- [53] Li, C. H. et al. *RSC Adv.* 2014, 4, 24955.
- [54] Nie, P. et al. *J. Mater. Chem. A* 2014, 2, 5852.
- [55] Sengodu, P. et al. *J. Alloys Compd.* 2017, 714, 603.
- [56] Huang, Y. et al. *Nano Energy* 2017, 39, 273.
- [57] Shokouhimehr, M. et al. *Nanosci. Nanotech. Let.* 2013, 5, 770.
- [58] Yu, S. H. et al. *RSC Adv.* 2014, 4, 12087.

## **1.4. A hybrid energy storage mechanism of zinc hexacyanocobaltate-based metal-organic framework endowing stationary and high-performance lithium-ion storage**

### **1.4.1. Introduction**

Electrical energy generated from renewable and low-cost resources has garnered growing attention due to the depletion verge of fossil fuels and the aggravation of environmental pollution.<sup>[1]</sup> Because of the intermittent nature of renewable resources, energy storage and conversion systems are required. The use of batteries for grid-scale energy storage and conversion devices potentially satisfies this requirement. Especially, rechargeable lithium-ion batteries (LIBs) as potential energy storage devices are expected to be able to offer efficient electrical energy storage, thus gaining significant attention.

However, the extensive utilization of LIBs is hindered because of lithium material cost and system fabrication complexities.<sup>[2-4]</sup> Therefore, a shift from LIBs to other metal-ion batteries, such as monovalent-ion batteries (*e.g.*, K<sup>+</sup>- and Na<sup>+</sup>-ion batteries) and multivalent-ion batteries (*e.g.*, Al<sup>3+</sup>-ion batteries) is observed.<sup>[5-8]</sup> Nevertheless, it is still a long way until the electric grid-scale applications of these emerging metal-ion batteries. Furthermore, to date, certain remarkable merits (*e.g.*, volume and weight efficiency, good transmission kinetics, and high energy and power densities) of LIBs still cannot be effectively replaced by other electrochemical battery systems.<sup>[9,10]</sup> However, certain existing problems

in the LIBs require to be resolved to achieve electric grid-scale energy storage. One of the solutions include the exploration of reasonable electrode materials for a new generation of advanced LIBs for the electric grid-scale application. Therefore, it is exceedingly necessary to pursue advanced materials with low-cost and facile fabrication for high-performance battery systems.

Low-cost and highly effective metal-organic frameworks (MOFs) are promising candidates as multifunctional electrode materials for grid-scale energy storage applications of LIBs.<sup>[11]</sup> The distinguished structural and electrochemical properties of MOFs have been documented in several literatures.<sup>[12-18]</sup> According to Ferey *et al.*,<sup>[19]</sup> the investigation of MOFs as electrode materials of rechargeable batteries has been increasingly gaining a broad interest.

Typically, MOF-structural Prussian blue analogs with cubic, face-centered open framework crystal structure have been studied as electrode materials for batteries assembled with aqueous or organic electrolytes.<sup>[20-26]</sup> These analogs were constructed using cyanide ligands and transition metal ions in a face-central framework structure similar to perovskites  $M_aM_bO_3$  constructed with ordered and alternative arrangement of  $M_a$  and  $M_b$  cations. Accordingly, the general formula of the Prussian blue analogs is  $A_xM_a[M_b(CN)_6]_{\square} \cdot nH_2O$  ( $A$ ,  $M_a$ ,  $M_b$ , and  $\square$  represent alkali metal ions, nitrogen coordinated transition metal ions, carbon coordinated transition metal ions, and vacancies of unpaired cyanide-ligand functional groups, respectively). The wide channels and

interstices (~1 nm) within the open framework allow the rapid Li<sup>+</sup> insertion into and extraction from with a spontaneous variation in the valence of the hosts.<sup>[27]</sup> Thus, the reversible electrochemical reactions of the Prussian blue analogs facilitate the prolonged lifetime of the electrode materials for LIBs.<sup>[28]</sup> Furthermore, robust crystal structure, high Coulombic efficiency, and low cost make Prussian blue analogs significant as an electrode material of LIBs for large-scale applications.

Based on the unique structural features and high electrochemical properties of the Prussian blue analogs, we synthesized and studied the Prussian blue analog, zinc hexacyanocobaltate (ZnHCCo, Figure 1a), as new cathode material for rechargeable LIBs used in grid-scale energy storage and conversion systems *via* the room temperature coprecipitation process using cost-efficient precursors, which are easily up scaled. Benefitting from the concomitant surface- and diffusion-controlled Li-ion storage, a highly reversible capacity of 121.5 mAh g<sup>-1</sup> at 1.25 C and a 96.5% Coulombic efficiency were obtained during charge/discharge cycling test.

#### **1.4.2. Material preparation**

ZnHCCo nanoparticles (NPs) were synthesized using a coprecipitation method, during which automatically dropwise addition of 100 ml of 0.03 M Zn(NO<sub>3</sub>)<sub>2</sub> and 100 ml of 0.03 M K<sub>3</sub>[Co(CN)<sub>6</sub>] to 100 ml of deionized H<sub>2</sub>O under vigorous magnetic stirring. Milk-white precipitation is formed immediately. After sonicating for 30 min, the

suspension was placed for one hour. The precipitate was separated, rinsed with a copious amount of deionized H<sub>2</sub>O and ethanol several times, and dried in an oven at 50 °C to be ready for further characterizations.

### **1.4.3. Material characterizations**

The structural study was conducted using X-ray diffraction (XRD, D8-Advance equipped with Cu K $\alpha$  radiation), X-ray photoelectron spectroscopy (XPS, PHI 5000 VersaProbe) using an Al K $\alpha$  source (Sigma probe, VG Scientifics), Raman technology (LabRAM HV Evolution), and Fourier Transform-Infrared (FT-IR, Nicolet iS50). The morphology and constitution were studied using field emission-scanning electron microscopy (FE-SEM, SUPRA 55VP), transmission electron microscopy (TEM, Tecnai F20), and energy-dispersive X-ray spectroscopy (EDX). The construction analysis of the as-prepared ZnHCCo product was performed using the thermogravimetric analysis (TGA, SDT) technique, which was conducted under N<sub>2</sub> flow from room temperature to 600 °C with a temperature ramp of 10 °C min<sup>-1</sup>, and X-ray fluorescence (XRF, ZSX-PRIMUS) technology.

A slurry was prepared *via* sufficiently grinding a mixture containing ZnHCCo NPs, carbon black (Super P Li), and poly(vinylidene)difluoride (PVDF) in a ratio of 7:2:1 followed by dispersing them in N-methyl-2-pyrrolidinone. This preparing process is similar to the standard slurry preparation method widely employed in the battery communities. Working electrode with mass loading of ~5 mg cm<sup>-2</sup> was prepared by

coating the slurry on a graphite paper current collector (Alfa Aesar) and subsequently drying in vacuum at 60 °C for 12 h.

A sufficiently large lithium metal foil was employed as the counter and Reference electrode to ensure the capacity limited only by the amount of ZnHCCo active materials. A two-electrode half-cell constructed with a graphite paper loaded with the as-prepared slurry and a lithium foil was employed as an electrochemical measurement system. Both electrodes were flooded in 1.0 M LiPF<sub>6</sub> in a 1:1 mixture by volume of ethylene carbonate and diethylene carbonate. The entire process was conducted in an Ar-filled glove box.

The electrochemical impedance spectroscopy (EIS) of the electrode was measured with an Im6ex ZAHNER impedance measurement instrument in a half cell. The frequency range is from 10 mHz to 1 MHz under a voltage amplitude of 10 mV.

Cyclic voltammetry measurements were conducted on an electrochemical workstation (WBCS3000, Wonatech, Korea) in the potential range of 2.2–4.5 V vs. Li<sup>+</sup>/Li at a scan rate of 0.2 mV s<sup>-1</sup>. Galvanostatic charge/discharge cycling measurement was conducted at various current densities set for 1.25 C, 2.5 C, 3.75 C, 5 C, and 6.25 C (160 mA g<sup>-1</sup> = 1 C) in the same voltage range. Cycling performance was conducted at 1.25 C for 100 cycles. All the specific capacities were calculated based on the mass of the active material.

#### 1.4.4. Results and discussion

The open framework microstructure of ZnHCCo composed of cyanide-bridged Co (on the C ends) and Zn (on the N ends) exposes wide open channels for Li-ion insertion (Figure 1.17). The corresponding structural study by powder X-ray diffraction (XRD, Figure 1.18a) demonstrated a uniform face-centered cubic crystal texture. The lattice parameter ( $10.2 \text{ \AA}$  from XRD result) of the as-prepared ZnHCCo is consistent with those previously reported for the Prussian blue analogs.<sup>[4]</sup>

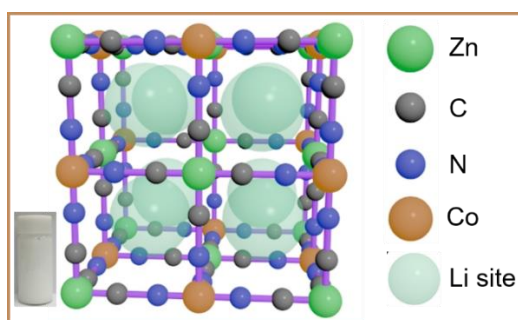


**Figure 1.17.** Theoretical crystal structure of ZnHCCo, where transition metal Co and Zn are orderly and alternately arranged in the cubic framework. Co is six-fold carbon-coordinated, while Zn is four-fold nitrogen-coordinated resulting in two unpaired cyanide vacancies. Each unit cell consists of eight-subunit cells ( $\text{Li}^+$  site), which can be occupied by  $\text{Li}^+$  ions. Inset shows the visual image of as-prepared product in an aqueous solution.

Distinguishable characteristic peaks are effectively matched with the

space group Fm-3m(225). The Raman spectra (Figure 1.18b) of the as-prepared ZnHCCo has demonstrated two significant vibrational bands at 2180 and 2203  $\text{cm}^{-1}$ , which are assigned to be the (-C $\equiv$ N-) stretching vibration of ZnHCCo. At wavenumber of 2178  $\text{cm}^{-1}$  in Fourier transform-infrared (FT-IR) spectroscopy (Figure 1.18c), the cyanide functional group was conclusively verified.<sup>[29]</sup> Residual water molecules were also detected *via* the FT-IR at the wavenumber of  $\sim$ 1610 and 3420  $\text{cm}^{-1}$ . The accurate amount of water within ZnHCCo NPs is difficult to determine, because of the variation in temperature and moisture of the environment. The morphology study using field-emission scanning electron microscopy (FE-SEM, Figure 1.18d,e) and transmission electron microscopy (TEM, Figure 1.18f) exhibit small and poly-disperse cubic-like NPs of the easily up-scaled ZnHCCo (Figure 1.18d, inset). Both the high crystallinity and small size of the open framework materials are expected to facilitate the rapid charge transport in each particle, enabling a complete charge/discharge of these materials in an exceedingly short time. In addition, the existing elements were qualitatively characterized using energy dispersive X-ray detector (EDX, Figure 1.18g and 1.19a). EDX mapping results of ZnHCCo conclusively verify the distribution of C, N, Co, and Zn elements throughout the as-prepared ZnHCCo. This result was also distinctly demonstrated in EDX spectra. In addition, EDX images exhibit a distinct existence of K impurity, which comes from the precursor  $\text{K}_3[\text{Co}(\text{CN})_6]$  that we used in the synthesis of ZnHCCo.

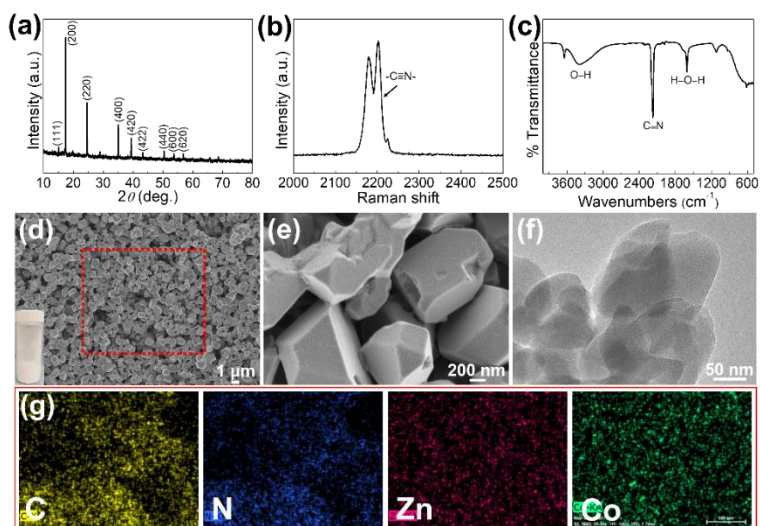


**Figure 1.18.** A series of representative characterizations of as-prepared ZnHCCo: (a) X-ray diffraction pattern, (b) Raman spectrum, (c) FT-IR spectra, (d,e) SEM images (inset shows a visual image of easily up scaled ZnHCCo powder), (f) TEM image, and (g) EDX mapping.

The relative accurate amount of water species was obtained *via* thermogravimetric analysis (TGA, Figure 1.19b) based on the weight loss prior to 200 °C, demonstrating water percentage of ~15 wt.% in the as-prepared ZnHCCo (~8 mole water molecules in one molecular formula), which are considerably reduced compared with previously reported transition metal-hexacyanoferrate products,<sup>[30]</sup> contributing to expose the active sites for electrochemical reactions. It is worth noting that a decomposition of our products at the temperature over ~450 °C guarantees the thermal stability when employed in practical energy

storage and conversion systems. Therefore, this satisfactory thermal stability demonstrates that the as-prepared cathode material is safe for use in practical batteries for numerous portable and stationary applications. A nominal formula of the as-prepared ZnHCCo was derived using X-ray fluorescence (XRF, Figure 1.19c,d, and Table 1.1). Following previous conventions of the crystal structure,<sup>[31,32]</sup> the molecular formula of the as-prepared ZnHCCo on the basis of Zn can be written as  $K_{0.48}Zn[Co(CN)_6]_{0.95}$ .

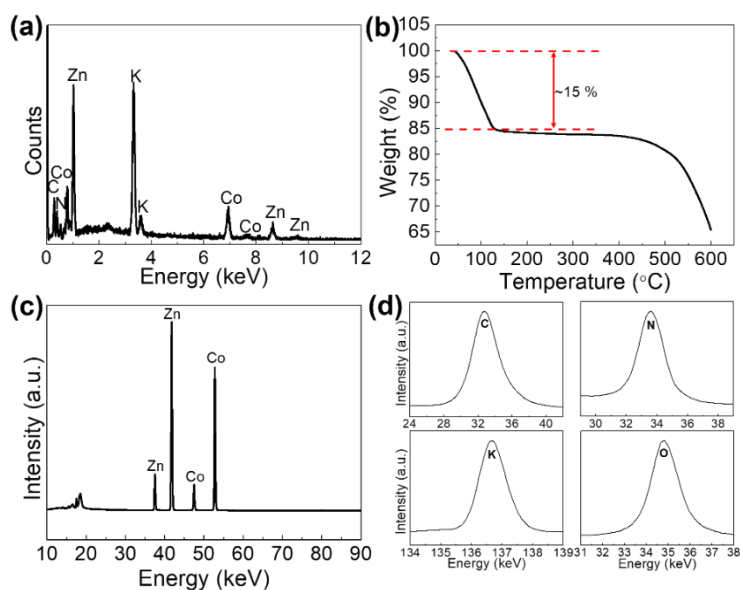


**Figure 1.19.** (a) EDX mapping and (b) TGA curve of ZnHCCo. (c) Wide survey and (d) respective elemental peaks in XRF spectra of ZnHCCo.

**Table 1.1.** Elemental mass percent in ZnHCCo measured by using XRF.

Element	Mass percent (%)
K	1.47
Zn	5.1
Co	4.41

Note: The measured elemental mass percent (%) is based on the weight of pretreated XRF sample. We deduced the molecular formula based on the normalized Zn.

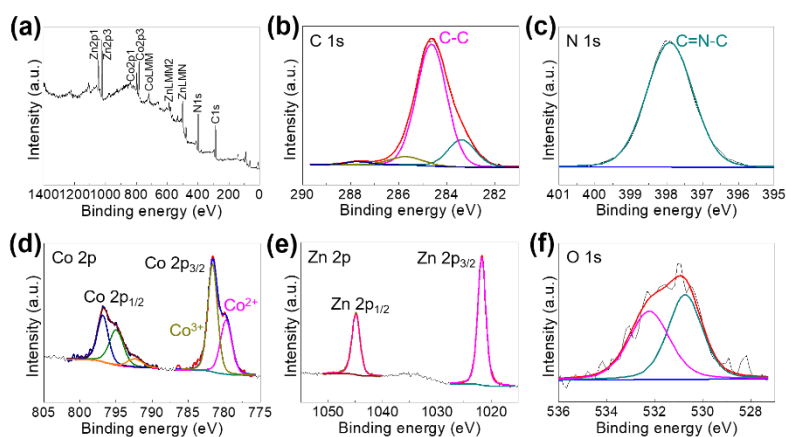


**Figure 1.20.** (a) Wide-survey scan, (b) C 1s, (c) N 1s, (d) Co 2p, (e) Zn 2p, and (f) O 1s XPS spectra of the ZnHCCo product.

The surface chemical states of ZnHCCo have been investigated using X-ray photoelectron spectroscopy (XPS, Figure 1.20), including wide survey, C 1s, N 1s, O 1s, Co 2p, and Zn 2p, which further confirmed the successful coordination of C, N, Co, and Zn elements within the product. The cyanide triple bond was conclusively demonstrated in Figure 1.20b

and c as with we expected. The valence state of Co was demonstrated in a high-resolution Co 2p XPS spectrum (Figure 1.20d), two distinct peaks located at binding energies of 781.5 and 796.7 eV could be indexed into trivalent Co 2p<sub>3/2</sub> and 2p<sub>1/2</sub>, respectively, accompanied by two evident satellite peaks at 777.2 and 793.8 eV. In addition, bivalent Zn 2p<sub>1/2</sub> and 2p<sub>3/2</sub> (Figure 1.20e) were indexed at 1044.8 and 1021.7 eV,<sup>[33,34]</sup> strongly verifying the valance state of Zn<sup>2+</sup> in the as-prepared ZnHCCo. The coordinated water molecules within ZnHCCo are further confirmed by the deconvoluted O 1s (Figure 1.20f).

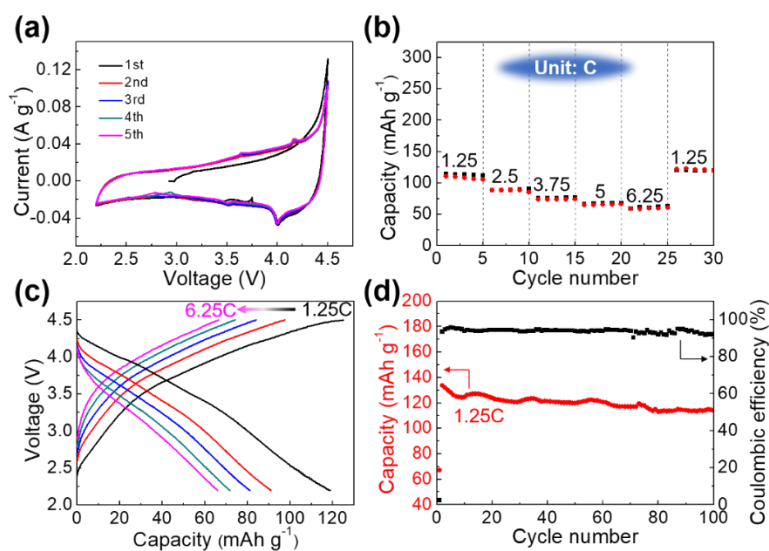


**Figure 1.21.** (a) Representative cyclic voltammetry curves of the ZnHCCo active material at a scan rate of 0.2 mV s<sup>-1</sup> between 2.2–4.5 V vs Li<sup>+</sup>/Li. (b) Rate performance of ZnHCCo at a wide variety of current densities of 1.25–6.25 C in the voltage range of 2.2–4.5 V vs. Li<sup>+</sup>/Li. (c) Corresponding charge/discharge voltage profiles of the ZnHCCo. (d)

Cycling measurement of as-prepared ZnHCCo at the current density of 1.25 C.

Cyclic voltammetry (CV) and galvanostatic charge/discharge measurements were conducted in 1 M LiPF<sub>6</sub> electrolyte based on a 1:1 vol.% mixture of ethylene carbonate and diethyl carbonate in the voltage range of 2.2–4.5 V vs. Li<sup>+</sup>/Li to evaluate their lithiation/delithiation performance as a cathode material. In the first sweep of CV curve (Figure 1.21a), there is one distinct peak around 4.0 V vs. Li<sup>+</sup>/Li, corresponding to the reduction of Co<sup>3+</sup> and the formation of solid electrolyte interface (SEI) film.<sup>[35]</sup> In the later cycles, this peak was replaced by two pairs of distinct peaks (at ~3.5 and ~4.0 V), indicating the redox reaction behavior during charge/discharge processes. We postulate the reaction mechanism observed for the ZnHCCo cathode that may exist owing to the electrochemical activity of the hexacyanocobaltate group instead of the nitrogen-coordinated zinc. However, to solve this problem, more research is required.

For the sake of convenience when describing current densities in the work presented here, we defined the C rate by galvanostatic charge/discharge (5 cycles) for the as-prepared electrode at 50 mA g<sup>-1</sup>. The calculated mean capacity value was 167 mAh g<sup>-1</sup>. Therefore, we defined 160 mA g<sup>-1</sup> as 1 C in this work. To highlight the rate performance, the as-prepared electrode was first activated for 5 cycles prior to the characterization of rate performance. The galvanostatic charge/discharge

at the current densities set for 1.25, 2.5, 3.75, 5, and 6.25 C in the potential window of 2.2–4.5 V vs. Li<sup>+</sup>/Li was conducted for the evaluation of rate performance (Figure 1.21b). It is worth mentioning that a reversible capacity of 50% (60.5 mAh g<sup>-1</sup>) at 6.25 C compared with 121.5 mAh g<sup>-1</sup> at 1.25 C was achieved. This satisfactory rate capability is considerably better than previously reported for MOFs as electrode materials.<sup>[36–38]</sup> The corresponding potential profiles are shown in Figure 2.21c. Compared with previously reported Prussian blue analogous, the ZnHCCo exhibits a superior Li-ion storage capability (Table 1.2).

**Table 1.2.** A comparison in capacity of Prussian blue and Prussian blue analogous as cathode of lithium-ion batteries.

<b>Ref. No.</b>	<b>Material</b>	<b>Capacity (mAh g<sup>-1</sup>)</b>	<b>Current density (mA g<sup>-1</sup>)</b>
23	Fe hexacyanoferrate	104	100
26	Cu <sub>(0.5)</sub> Mn <sub>(0.5)</sub> hexacyanoferrate	70	30
36	Ni hexacyanoferrate	60	30
39	Ni hexacyanoferrate	52	12
40	Fe hexacyanoferrate	138	25
41	Mn hexacyanoferrate	128	56
This work	Zn hexacyanocobaltate	121	200

Cycling stability was measured in another cell at 1.25 C between 2.2–4.5 V vs. Li<sup>+</sup>/Li for 100 cycles (Figure 1.21d). A highly reversible capacity of 121.5 mAh g<sup>-1</sup> at 1.25 C and a satisfactory cycling stability with a 96.5% Coulombic efficiency were demonstrated. The stability and satisfactory electrochemical properties of the as-prepared ZnHCCo is because of the robust crystal structure with wide open frameworks that may undergo only a finite lattice strain during the reversible charge/discharge cycling.

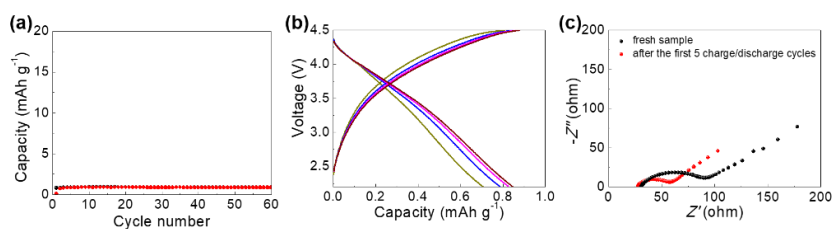


**Figure 1.22.** (a) Charge/discharge cycling measurement for the naked graphite paper current collector. (b) Corresponding voltage profiles display a negligible capacitive behavior. (c) EIS of fresh electrode and electrode after the first 5 charge/discharge cycles.

In a controlled experiment, a naked graphite paper current collector was measured in the same manner to ensure that the capacity was intensively coming from the active material ZnHCCo, although the electrochemical potential of graphite was suitable for anode. As a result, a negligible capacity was obtained (Figure 1.22a). The corresponding charge/discharge curves show a tedious capacitive behavior (Figure

1.22b). The superior rate performance and life-span of ZnHCCo are associative with the lower impedance (Figure 1.22c), where impedance of  $\sim 30$  Ohm is exhibited by the intercept of semicircle of after the first 5 charge/discharge cycles with  $Z'$  axis. The decreased impedance for the samples encountered charge/discharge cycles is most likely due to the activation of the active material and electrolyte infiltration as shown by the improved porosity of coated slurry (Figure 1.23).

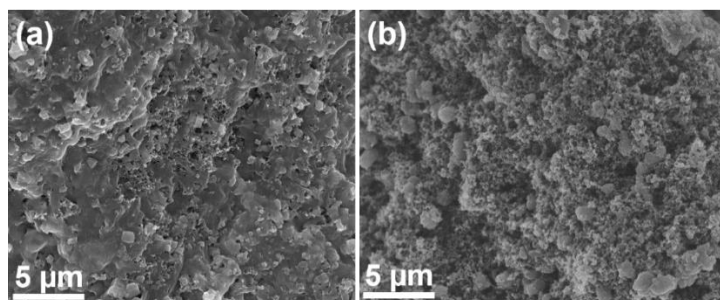


**Figure 1.23.** SEM images of (a) fresh electrode and (b) after the first 5 charge/discharge cycling measurement. It shows an improved porosity for the overall electrode, and well preserved active materials.

To further study the Li-ion storage mechanism behind the capacity of ZnHCCo, CV curves at diverse scan rates are performed (Figure 1.24a). The response currents of those well-preserved CV curves at different scan rates are typically studied by plotting the current values at a fixed voltage of 3.5 V (Figure 1.24b). Qualitative analysis on the Li-ion storage mechanism can be achieved by the following power law relationship:

$$i = av^b \quad (1)$$

Fitting of a  $\log(i)$  vs.  $\log(v)$  plot is expected to afford a straight line with slope  $b$ ;  $b = 0.5$  corresponds to diffusion-controlled Li-ion storage and thus indicates a Faradic electrochemical reaction, while  $b = 1.0$  corresponds to capacitive Li-ion storage. Furthermore, the relative contributions of these storage mechanisms were calculated by re-expressing Eq. (1) as:

$$i = k_1v + k_2v^{1/2} \quad (2)$$

where  $k_1v$  represents the contribution of the  $b = 1$  case, and  $k_2v^{1/2}$  represents the contribution of the  $b = 0.5$  case. In our case (Figure 1.24b),  $b$ -values between 0.5 and 1.0 were observed, which indicated the co-existence of diffusion- and surface-controlled Li-ion storage mechanisms. The obtained results are presented in Figure 1.24c, which shows that at  $0.5 \text{ mV s}^{-1}$ , 46.6% of the total capacity corresponded to capacitive  $\text{Li}^+$  storage. This contribution slightly increased with increasing scan rate (66.11% at  $2.5 \text{ mV s}^{-1}$ ), which indicated that capacitive Li-ion storage mechanism became even more dominant under higher scan rates.

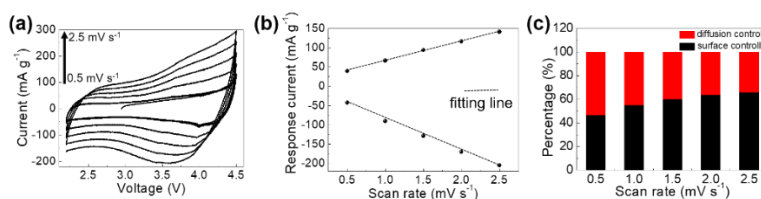


**Figure 1.24.** (a) CV curves of ZnHCCo at various scan rates. (b)

Response currents measured in the CV curves at a fixed 3.5 V. (c) contribution distribution for Li<sup>+</sup> storage at different scan rates.

#### **1.4.5. Conclusions**

In this work, we demonstrated the synthesis of the Prussian blue analog—ZnHCCo—and its electrochemical performance as a low-cost cathode material for rechargeable LIBs. A highly reversible capacity of 121.5 mAh g<sup>-1</sup> at 1.25 C and a satisfactory cycling stability with a 96.5% Coulombic efficiency were achieved benefitting from the concomitant surface- and diffusion-controlled Li-ion storage. In addition, the ZnHCCo demonstrates a superior rate capability of 60.5 mAh g<sup>-1</sup> at 6.25 C because of its wide channels for Li<sup>+</sup> transfer. It is worth highlighting that the present synthesis method of nano-sized ZnHCCo is facile and easily up scaled, which are significant in large-scale energy storage and conversion applications.

#### **1.4.6. References**

- [1] Dunn, B. et al. *Science* 2011, 334, 928.
- [2] Soloveichik, G. L. *Annu. Rev. Chem. Biomol. Eng.* 2011, 2, 503.
- [3] Yang, Z. et al. *Chem. Rev.* 2011, 111, 3577.
- [4] Lee, H. W. et al. *Nat. Commun.* 2014, 5, 5280.
- [5] Nie, P. et al. *J. Mater. Chem. A.* 2015, 3, 16590.
- [6] Xiong, P. et al. *ChemSusChem.* 2018, 11, 202.

- [7] Yan, C. et al. *J. Mater. Chem. A*. 2018, 6, 17371.
- [8] Pasta, M. et al. *Nat. Commun.* 2014, 5, 3007.
- [9] Chen, K. et al. *Adv. Funct. Mater.* 2018, 28, 1707592.
- [10] Lu, Y. et al. *Adv. Mater.* 2018, 30, 1702875.
- [11] Li, X. et al. *J. Power Sources* 2006, 160, 542.
- [12] Nie, P. et al. *ACS Appl. Mater. Inter.* 2017, 9, 20306.
- [13] Kim, D. S. et al. *Electrochim. Acta*. 2017, 240, 300.
- [14] Luo, J. et al. *ACS Appl. Mater. Inter.* 2017, 9, 25317.
- [15] Deng, L. et al. *Adv. Mater.* 2018, 30, 1802510.
- [16] Wu, X. et al. *Electrochem. Commun.* 2017, 77, 54.
- [17] He, G. et al. *ACS Energy Lett.* 2017, 2, 1122.
- [18] Zhang, C. et al. *Adv. Funct. Mater.* 2017, 27, 1604307.
- [19] Ferey, G. et al. *Angew. Chem. Int. Ed.* 2007, 46, 3259.
- [20] Jayalakshmi, M. et al. *J. Power Sources* 2000, 91, 217.
- [21] Eftekhari, A. *J. Power Sources* 2003, 117, 249.
- [22] Eftekhari, A. *J. Power Sources* 2004, 132, 291.
- [23] Yu, S. H. et al. *ECS Electrochem. Lett.* 2013, 2, A39.
- [24] Yu, S. H. et al. *RSC Adv.* 2014, 4, 37365.
- [25] Yu, S. H. et al. *RSC Adv.* 2014, 4, 12087.
- [26] Shokouhimehr, M. et al. *Nanosci. Nanotech. Lett.* 2013, 5, 770.
- [27] You, Y. et al. *J. Mater. Chem. A*. 2013, 1, 14061.
- [28] Wessells, C. D. et al. *ACS Nano* 2012, 6, 1688.

- [29] Xie, M. et al. *J. Power Sources* 2016, 302, 7.
- [30] Liu, S. et al. *J. Mater. Chem. A*. 2015, 3, 959.
- [31] Ludi, A. et al. *Inorg Chem* 1973, 14, 1.
- [32] Buser, H. J. et al. *Inorg. Chem.* 1977, 16, 2704.
- [33] Chen, Y. et al. *Phys. Chem. Chem. Phys.* 2015, 17, 14012.
- [34] Tang, R. et al. *Sci. Rep.* 2015, 5, 13645.
- [35] Xu, M. et al. *Nanoscale* 2013, 5, 8067.
- [36] Li, C. H. et al. *RSC Adv.* 2014, 4, 24955.
- [37] Nie, P. et al. *J. Mater. Chem. A* 2014, 2, 5852.
- [38] Sengodu, P. et al. *J. Alloys Compd.* 2017, 714, 603.
- [39] Omarova, M. et al. *Electrochim. Acta* 2015, 184, 58.
- [40] Shen, L. et al. *Chem.-Eur. J.* 2014, 20, 12559.
- [41] Okubo, M. et al. *Dalton T.* 2013, 42, 15881.

## **1.5. Coordinating gallium hexacyanocobaltate: Prussian blue-based nanomaterial for Li-ion storage**

### **1.5.1. Introduction**

Batteries are considered necessary devices for the integration of renewable and green natural energy resources into electric grid.<sup>[1-4]</sup> Lithium-ion batteries (LIBs) have seen great advances because of increases in the reliability and durability of the anodes and cathodes, and LIBs now have highly improved energy and power densities.<sup>[5-7]</sup> However, improvements in anodic safety and in cost efficiency of electrode materials are still required. Typically, the further modification of anode materials to prevent or minimize the formation of dendrites and to form a stable solid electrolyte interface<sup>[8,9]</sup> and the development of low-cost cathode materials synthesized by facile and environmentally friendly processes are required for sustainable developments. To date, several research groups have explored different types of high-performing cathode materials for LIBs,<sup>[10,11]</sup> but further work is required to reduce the complexity of cathode material synthesis while maintaining excellent electrochemical properties.

Metal-organic frameworks (MOFs) are multi-functional materials that have been studied in diverse fields including catalysts, gas sensors, and solid electrolytes and have shown great potential.<sup>[12-16]</sup> With regard to the use of MOFs as cathode materials for LIBs, two different methods (direct use or as sacrificial precursors) are typically employed.<sup>[17,18]</sup> In

particular, Prussian blue analogs (PBAs), which are typical MOFs, are considered one of the most attractive candidates because of their easy synthesis in aqueous solution at room temperature without the need of additives or post-processing.<sup>[19]</sup> Recently, the study of PBAs as cathode materials for LIBs has mainly focused on functionalized PBAs (for example, those treated by etching, oxidation, or combination with other materials such as carbon nanotubes),<sup>[20,21]</sup> which results in highly improved electrochemical properties. However, this extra processing increases the fabrication costs during a massive fabrication. Thus, the further study of naked PBAs is logical. With regard to the study of naked PBAs, research groups have mainly focused on  $A_3[M^{III}(CN)_6]_2$  and  $A_2M^{II}(CN)_6$  systems having  $A^{2+}$  ions and  $B_4[M^{II}(CN)_6]_3$  and  $BM^{III}(CN)_6$  systems having  $B^{3+}$  ions (M: transition metal ions coordinated to C; A and B: transition metal ions coordinated to N). However, the latter case (i.e., those constructed with  $B^{3+}$  ions) is limited to  $Fe^{3+}$  such as  $Fe^{3+}Fe(CN)_6$ ,  $Fe^{3+}Co(CN)_6$ , and  $Fe^{3+}Cr(CN)_6$ .<sup>[22,23]</sup> Therefore, studies of PBAs constructed with other types of N-coordinated trivalent metal ions are necessary to provide an in-depth understanding for this overlooked issue. To obtain a trivalent metal ion that is soluble and stable in an aqueous solution, we systematically studied the elements in the periodic table. The elements of the boron group in the periodic table have typical trivalent characteristics. We, thus, fabricated the six-fold coordinated PBAs using the lighter Ga species. In particular, we synthesized the Ga hexacyanocobaltate (GaHCCo) and further studied its electrochemical properties as a cathode material of LIBs, revealing a solid-state diffusion-

controlled Li-ion storage mechanism by utilizing the Co species.

### **1.5.2. Material preparation**

GaHCCo nanoparticles (NPs) were synthesized by a co-precipitation method involving the simultaneous dropwise addition of 100 mL  $\text{Ga}(\text{NO}_3)_3$  (0.01 M) (Sigma-Aldrich) and 100 mL  $\text{K}_3[\text{Co}(\text{CN})_6]$  (0.01 M) (Sigma-Aldrich) to 200 mL deionized  $\text{H}_2\text{O}$ . The entire synthesis process was carried out at 80 °C with vigorous stirring. The formation of a precipitate was observed after a period of heating. After a cooling of the mixture to room temperature, the precipitate was separated and rinsed with large amounts of deionized water several times to remove the impurity ions (such as  $\text{K}^+$ ) and subsequently dried in a vacuum oven at 60 °C; it was then ready for subsequent use.

### **1.5.3. Material characterizations**

X-ray diffraction (XRD, D8 Advance, Bruker, Cu  $K$  radiation at a fixed incident angle of  $2^\circ$ ), X-ray photoelectron spectroscopy (XPS, PHI 5000 VersaProbe with an Al  $K_\alpha$  source (Sigma Probe, VG Scientific)), Raman spectroscopy (inVia Raman Microscope), and Fourier transform infrared (FTIR, Nicolet iS50, Thermo Fisher) spectroscopy measurements were carried out. The morphology and composition of the samples were investigated using field emission-scanning electron microscopy (FE-SEM, SUPRA 55VP, Carl Zeiss AG), transmission

electron microscopy (TEM, JEOL JEM-2100F), energy-dispersive X-ray spectroscopy (EDX). The analysis for a composition of the as-prepared GaHCCo was also carried out using thermogravimetric analysis (TGA) which was performed under N<sub>2</sub> flow from room temperature to 700 °C with a temperature ramp of 10 °C min<sup>-1</sup>, as well as X-ray fluorescence measurements (XRF, ZSX-PRIMUS, Rigaku). Quantitative measurements were achieved by using inductively coupled plasma (ICP) for Ga, Co, and K elements and EA(CHNS) analysis for C, H, and N elements.

A slurry containing GaHCCo, carbon black (Super P Li), and poly(vinylidene)difluoride in a mass ratio of 7:2:1 was prepared by manually grinding the mixed powders and subsequently dispersing them in *N*-methyl-2-pyrrolidinone (NMP) in a manner similar to the standard slurry preparation method widely employed in the LIB research communities. In addition, before the injection of NMP, the mixed powders were dried overnight in a vacuum oven at 60 °C. The mixed powder weight was measured before and after vacuum drying to ensure that water was eliminated as much as possible. A working electrode with a mass loading of approximately 3 mg cm<sup>-2</sup> was prepared by spreading the slurry on a graphite paper current collector (Alfa Aesar), followed by drying overnight in a vacuum oven at 60 °C.

To perform electrochemical measurements, a two-electrode setup was used: the GaHCCo active material was used as the working electrode and

sufficient lithium metal to ensure that the capacity was limited solely by the mass of active materials was used as the anode. The electrodes were placed in 1.0 M LiPF<sub>6</sub> in a 1:1 mixture (by volume) of ethylene carbonate and diethylene carbonate in an argon-filled glove box.

The electrochemical impedance spectrum (EIS) of GaHCCo was measured using an Im6ex ZAHNER instrument in the assembled half-cell. The frequency range used was from 10 mHz to 1 MHz, at a voltage amplitude of 10 mV.

Cyclic voltammetry (CV) measurements were performed on an electrochemical workstation (WBCS3000, WonATech Co., Ltd., Korea) in the potential range of 2.2–4.5 V vs. Li<sup>+</sup>/Li at a scan rate of 0.5 mV s<sup>-1</sup>. Galvanostatic charge/discharge cycling measurements were performed between 2.2 and 4.5 V vs. Li<sup>+</sup>/Li at various current densities corresponding to 100, 200, 400, 600, 800, and 1,000 mA g<sup>-1</sup>. Unless otherwise specified, all the current densities and specific capacities in the present study were calculated based on the weight of the active material, GaHCCo.

#### **1.5.4. Results and discussion**

The proposed crystal structure is shown in Figure 2.25; the structure consists of a face-centered cubic crystal structure containing cyanide bridges alternately bonded with Co<sup>3+</sup> and Ga<sup>3+</sup> centers, having eight cavities (sub-units) within each unit with a size as small as ca. 1 nm.

Morphologies of the GaHCCo particles are observed using FE-SEM, and the NPs are found with a size of ca. 500 nm (Figure 1.25b). Furthermore, the comprising elements were uniformly distributed throughout the NPs (Figure 1.25c). The further magnification images of the particles are obtained using TEM (Figure 1.25d) displaying the particle with a diameter of ca. 500 nm and uniformly distributed elements as shown in the elemental mapping. To investigate this further, TGA experiments were conducted (Figure 1.25e), and it revealed a constant decrease in a weight of the product upon heating, confirming the structural weakness of GaHCCo, which is unlike that of other PBAs being able to withstand a temperature up to 400 °C.<sup>[24]</sup> The crystalized feature is depicted in the XRD result. Furthermore, the crystal structure is further confirmed by the Rietveld Refinement showing well matched XRD curves for experimentally obtained result and calculated one. The Refinement parameters are given in Table 1.3 demonstrating a space group 225 and lattice parameters of  $a=b=c=10.0971 \text{ \AA}$ . The characteristic lattice diffraction peaks in the XRD patterns (Figure 1.25f) indicate a typical face-centered cubic crystal structure for the GaHCCo. The characteristic Bragg diffraction peaks (PDF card no. 01-072-1431) are well indexed. Here, the standard diffraction peaks are Referred to the PBA  $\text{Co}_3[\text{Co}(\text{CN})_6]_2$  with a cubic crystal structure due to the absence of the corresponding standard card for GaHCCo. The presence of cyanide bridges was inferred from FTIR (Figure 1.25g), which showed characteristic bands at ca.  $2,200 \text{ cm}^{-1}$ . Furthermore, the cyanide bridges were further detected using Raman spectroscopy (Figure 1.25h),

revealing characteristic bands at ca. 2,210 and 2,240  $\text{cm}^{-1}$ , consistent with reports concerning other PBAs.<sup>[25]</sup>

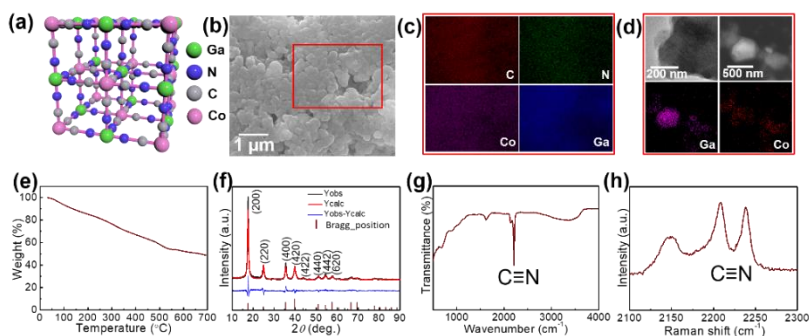


**Figure 1.25.** (a) Crystal structure (b) FE-SEM image, (c) EDX mapping, (d) TEM images, (e) TGA curve, (f) XRD and Rietveld Refinement curves, (g) Raman spectrum, and (h) FT-IR spectrum of the GaHCCo.

**Table 1.3.** Details of Rietveld Refinement parameters for the GaHCCo.

Parameters	Values
Space group	225
$a$ (Å)= $b$ = $c$	10.0971
$V$ (Å <sup>3</sup> )	1029.4
$C(x, y, z)$	(0.303, 0.000, 0.000)
$N(x, y, z)$	(0.1928, 0.000, 0.000)
$Ga(x, y, z)$	(0.500, 0.500, 0.500)
$Co(x, y, z)$	(0.000, 0.000, 0.000)
$R_{\text{Bragg}}$	3.607

$R_{wp}$	16.42
$R_{exp}$	10.41
$R_p$	13.17
GOF	1.58

The comprising elements are also clearly confirmed in XRF spectra (Figure 1.26). The composition elements are screened out at different energies as shown by peaks with high intensities for each element. A quantitative elemental analysis for the GaHCCo by ICP and EA(CHNS) (Table 1.4) demonstrates the molecular formula  $K_{0.017}Ga_{0.99}Co(CN)_6 \cdot 0.32H_2O$ . Furthermore, the surface chemical properties of the GaHCCo product are studied using XPS. The wide-survey spectrum (Figure 1.27a) indicates bonding nature in GaHCCo. The C 1s and N 1s peaks in the deconvoluted spectra are consistent with the presence of cyanide bridges, as indicated by the FTIR and Raman spectra (Figure 1.25g, h). Concomitant  $Co^{3+}$  and  $Co^{2+}$  ions in the deconvoluted Co 2p spectra with different energies are consistent with the split Raman peaks. Unlike the Co 2p peak, the deconvoluted Ga 2p peak indicates pure  $Ga^{3+}$  after the aqueous synthesis process. Thus, the XPS results demonstrate the bonding state of the formed GaHCCo.

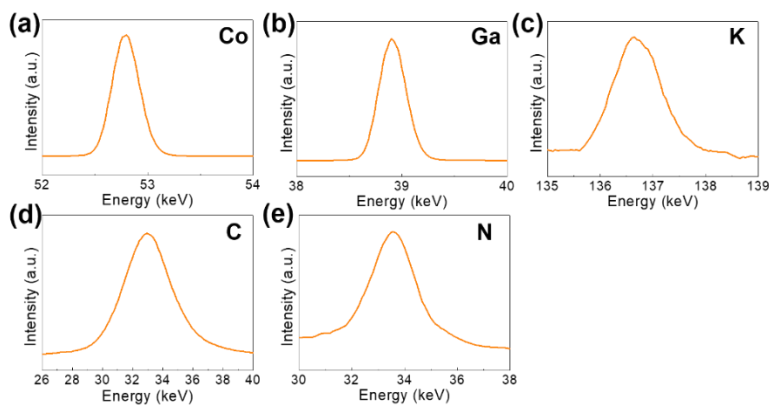


**Figure 1.26.** (a) XRF spectra of the synthesized GaHCCo.

**Table 1.4.** EA (CHNS) for C, H, N elements and ICP for Co, Ga, and K elements measurements of the as-prepared GaHCCo.

Element	C (wt.%)	H (wt.%)	N (wt.%)	Co (wt.%)	Ga (wt.%)	K (wt.%)
Amount	22.51	1.29	24.19	13.30	15.60	0.07

Electrochemical properties of GaHCCo as a cathode material are studied using CV measurements to determine the electrochemical activity toward Li-ion storage. A stable potential window of 2.2–4.5 V vs.  $\text{Li}^+/\text{Li}$  without obvious distortion was observed in the CV profile (Figure 1.28a). The quasi-rectangular CV curves indicate a predominant double-layer capacitive charge storage feature. The rate performance of GaHCCo is determined at current densities of 100, 200, 400, 600, 800,

and 1,000 mA g<sup>-1</sup>, with a capacity retention of 42.2% at 1,000 mA g<sup>-1</sup>. The corresponding charge/discharge potential profiles exhibit quasi-plateaus at ca. 4.0 V vs. Li<sup>+</sup>/Li (Figure 1.28c). A capacity differential (dQ/dV) (Figure 1.28d) exhibits a pair of depressed humps as marked in the differential curves suggesting the charge/discharge plateaus in the voltage profiles (Figure 1.28c). The long-term repeated charge/discharge process is shown in Figure 1.28e, where an initial capacity of ca. 80 mAh g<sup>-1</sup> after the activation phase is obtained. A high capacity retention of 75% is achieved after 3,000 cycles of successive charge/discharge testing, corresponding to an average loss in capacity of 0.008% for each cycle, although some fluctuation in the electrochemical capacities is observed. Notably, a high Coulombic efficiency of ca. 98% is achieved during the long-term cycling measurements (Figure 1.28e). The voltage profiles during the long-term capacity test are shown in Figure 1.28f, revealing the tedious charge/discharge process with quasi-plateaus at around 3.9 V vs. Li<sup>+</sup>/Li (charge) and 3.3 V vs. Li<sup>+</sup>/Li (discharge) for each cycle, which can be described as Li-ion redox reactions with local equilibrium.<sup>[26,27]</sup>

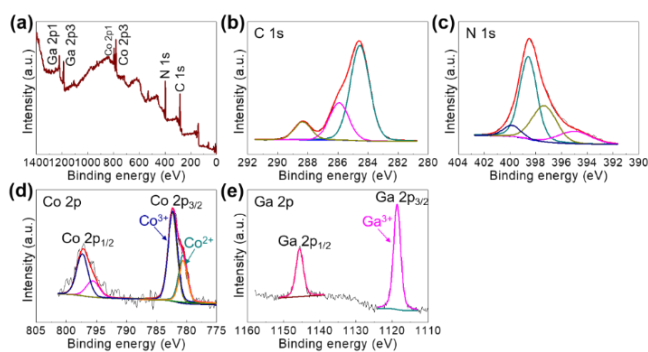


**Figure 1.27.** (a) Wide-survey and deconvoluted (b) C 1s, (c) N 1s, (d)

Co 2p, and (e) Ga 2p XPS spectra of the GaHCCo.

The Li-ion storage process of GaHCCo is further studied using the ex-situ XRD method (Figure 1.29). The XRD spectra of the samples charged to 2.2, 3.0, and 3.6 V vs. Li<sup>+</sup>/Li reveal the collapse of the GaHCCo structure, which is similar with the previously reported Co<sub>3</sub>[Co(CN)<sub>6</sub>]<sub>2</sub> as anode for potassium-ion batteries.<sup>[28]</sup> This can be further observed in the sample after a repeated charge/discharge cycling test (Figure 1.30b), where the characteristic peaks of GaHCCo are greatly eliminated. A newly formed peak (corresponding to Li<sub>0.73</sub>CoO<sub>2</sub>) at ca. 18° in the XRD pattern (Figure 1.29d) indicates that the corresponding charge/discharge process is mainly achieved by bonding with Co species instead of Ga. On increasing the cutoff voltage, the intensity of this phase was reduced, illustrating the underlying delithiation process. This can be further demonstrated in the ex-situ XPS results by the gradually increase of the deconvoluted Co<sup>2+</sup> peak intensity with discharge proceeding (Figure 1.31). Other deconvoluted XPS results (C 1s, N 1s, and Ga 2p) exhibit an absence of obvious changes (Figure 1.31). This is the first example of Li-ion storage in a collapsed PBAs via bonding with one of the host species.

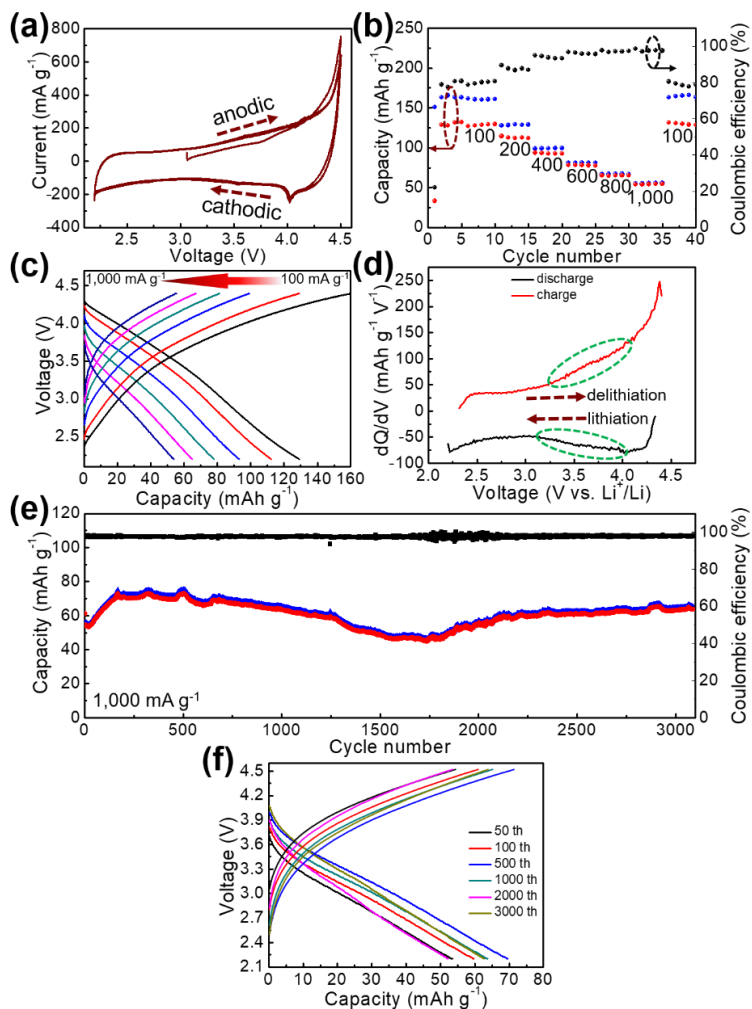


**Figure 1.28.** (a) CV curves, (b) rate performance, (c) corresponding voltage profiles, (d)  $dQ/dV$  curves, (e) long-term repeated cycling test, and (f) representative voltage profiles of the GaHCCo.

The electrochemical impedance spectra of GaHCCo is shown in

Figure 1.30c, with a depressed semicircle (charge transfer process) connected with an oblique line (mass transfer process). The material exhibits a charge transfer impedance of ca.  $200 \Omega$ . In a controlled experiment, we also measure the capacity of the bare graphite paper current collector, which shows a negligible capacity (Figure 1.30d).

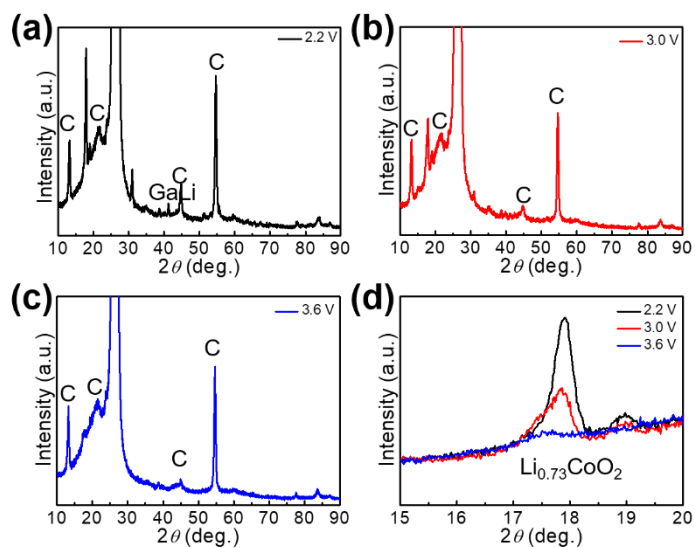


**Figure 1.29.** (a) Ex-situ XRD patterns of GaHCCo at (a) 2.2 V, (b) 3.0 V, (c) 3.6 V, and (d) magnified XRD peaks.

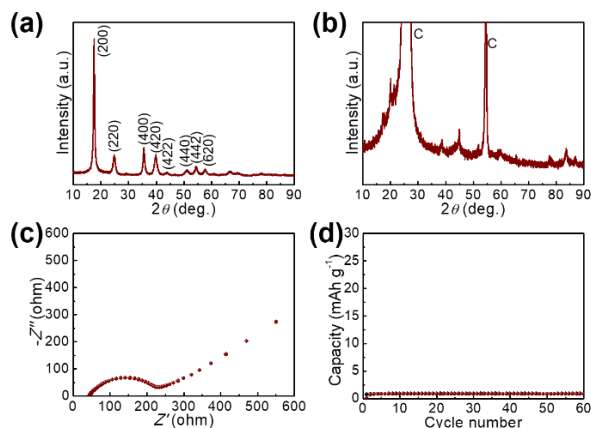


**Figure 1.30.** XRD pattern of the GaHCCo (a) before and (b) after cycling test. (c) EIS spectrum of the GaHCCo. (d) The charge/discharge cycling measurement of the bare graphite paper current collector.

To analyze the contributions of diffusion-controlled and capacitive Li-ion storage contributions to the total Li-ion storage capacity of GaHCCo qualitatively and quantitatively, we carried out CV measurements for the GaHCCo cathode at different scan rates ( $0.5\text{--}2.5\text{ mV s}^{-1}$ ) within the same potential window of  $2.2\text{--}4.5\text{ V vs. Li}^+/\text{Li}$  (Figure 1.32a). The curves obtained at all scan rates displayed a quasi-rectangular shape. To investigate this capacitive feature further, the dependence of response current ( $i$ ) on scan rate ( $\nu$ ) is modeled using the following power law:  $i = a\nu^b$ .

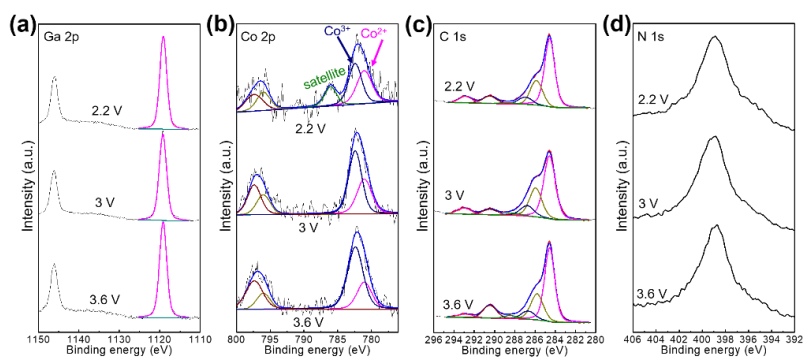


**Figure 1.31.** Ex-situ XPS characterizations for the electrode charged at 2.2, 3.0, and 3.6 V.

The fitting of a  $\log(i)$  vs.  $\log(v)$  plot is expected to afford a straight line with slope  $b$ ;  $b = 0.5$  corresponds to diffusion-controlled Li-ion storage, indicating a Faradic electrochemical reaction, whereas  $b = 1.0$  corresponds to capacitive Li-ion storage. Here,  $b$ -values between 0.5 and 1.0 are observed, which indicates the concomitant nature of diffusion-controlled and capacitive Li-ion storage (Figure 1.32b). The relative contributions of these storage mechanisms are further calculated by re-expressing Eq. (1) as:  $i = k_1v + k_2v^{1/2}$ , where  $k_1v$  represents the contribution of the  $b = 1$  case, and  $k_2v^{1/2}$  represents the contribution of the  $b = 0.5$  case. The obtained results are presented in Figure 1.32c, which shows that at  $0.5 \text{ mV s}^{-1}$ , 30% of the total capacity corresponded to capacitive  $\text{Li}^+$  storage. This contribution increases with increasing scan rates (49% at  $2.5 \text{ mV s}^{-1}$ ), which indicates that the Faradic redox reaction dominated the Li-ion storage process.

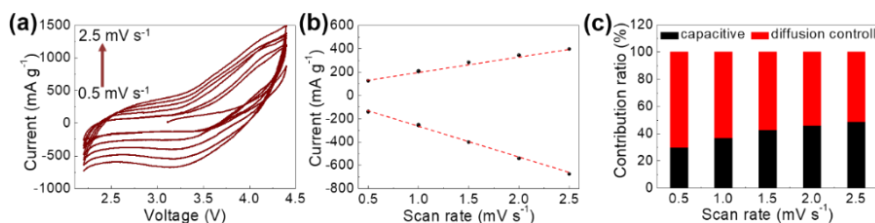


**Figure 1.32.** (a) CV curves obtained at various scan rates, (b) response currents at 3.1 V when scanned at different rates, and (c) contribution ratios of capacitive and diffusion-controlled Li-ion storage.

### 1.5.5. Conclusions

In this study, we conduct the formation of GaHCCo with an N-coordinated trivalent metal ion ( $\text{Ga}^{3+}$ ) as a cathode material for LIBs. The PBA depicts a face-centered cubic structure with a unique thermally sensitive property. In addition, the synthesized GaHCCo exhibits long-term charge/discharge stability, having a capacity retention of 75% after 3,000 cycles of repeated cycling test with an extremely high Coulombic efficiency of 98%, benefiting from a solid-state diffusion-controlled Li-ion storage process. In particular, the Li-ion storage in the GaHCCo is mainly attributed to the Co species by forming a Li/Co compound. This work will pave the way toward the study of PBAs constructed with other trivalent metal ions coordinated to N end of cyanides and provides more insights into the development of high-performing LIBs in the future.

### 1.5.6. References

- [1] Zhang, K. et al. *J. Alloy Compd.* 2019, 791, 911.
- [2] Li, W. et al. *Nano Lett.* 2015, 15, 1691.
- [3] Yu, S.-H. et al. *ECS Electrochem. Lett.* 2013, 2, A39.
- [4] Shokouhimehr, M. et al. *Nanosci. Nanotech. Lett.* 2013, 5, 770.
- [5] Xu, Q. et al. *Adv. Energy Mater.* 2017, 7, 1601481.
- [6] Zhou, J. et al. *ACS Nano* 2015, 9, 3837.
- [7] Yu, S.-H. et al. *RSC Adv.* 2014, 4, 37365.
- [8] Yu, S.-H. et al. *RSC Adv.* 2014, 4, 12087.
- [9] Sun, Y. et al. *Nat. Energy* 2016, 1, 16071.
- [10] Chen, K. et al. *Adv. Funct. Mater.* 2018, 28, 1707592.
- [11] Pang, Q. et al. *Nat. Energy* 2016, 1, 16132.
- [12] Huang, Y.-B. et al. *Chem. Soc. Rev.* 2017, 46, 126.
- [13] Koo, W.-T. et al. *J. Am. Chem. Soc.* 2016, 138, 13431.
- [14] Wang, Z. et al. *Adv. Mater.* 2018, 30, 1704436.
- [15] You, Y. et al. *Nano Res.* 2015, 8, 117.
- [16] You, Y. et al. *Energy Environ. Sci.* 2014, 7, 1643.
- [17] Wei, T. et al. *Nano Energy* 2017, 34, 205.
- [18] Guan, C. et al. *Adv. Energy Mater.* 2017, 7, 1602391.
- [19] Shokouhimehr, M. et al. *J. Mater. Chem.* 2010, 20, 5251.
- [20] Hou, X. et al. *J. Alloy Compd.* 2017, 729, 518.
- [21] Shao, J. et al. *Appl. Surf. Sci.* 2019, 471, 745.

- [22] Zhang, K. et al. *Electron. Mater. Lett.* 2019, 1.
- [23] Luque, F. J. et al. *J. Mater. Chem. C* 2018, 6, 8171.
- [24] Bhatt, P. et al. *New J. Chem.* 2018, 42, 4567.
- [25] Wang, Q. et al. *New J. Chem.* 2016, 40, 3244.
- [26] Mazinani, B. et al. *JOM* 2019, 71, 1499.
- [27] Huggins, R. A. *J. Power Sources* 1999, 81, 13.
- [28] Deng, L. et al. *Adv. Mater.* 2018, 30, 1802510.

## **1.6. Graphite carbon-encapsulated metal nanoparticles derived from Prussian blue analogs growing on natural loofa as cathode materials for rechargeable aluminum-ion batteries**

### **1.6.1. Introduction**

With the gradual reduction of fossil energy resources, increasing environmental problems, and increasing demand for energy, the search for an ideal energy has become highly challenging.<sup>[1]</sup> Currently, integrating clean, sustainable energy resources (solar, wind, geothermal, *etc.*) into the electric grid is considered as a potential solution.<sup>[2]</sup> However, their intermittencies are major obstacles that require energy storage devices. Hence, batteries have received significant attention and are considered as an ideal candidate owing to their unique energy storage mechanism (electrical energy to chemical energy). Meanwhile, the vigorous development of such devices can be applied to the electric energy storage in a power grid, as well as realize the transformation of the current traction of internal combustion engines to the fully electric traction vehicles, which will improve the urban environmental quality significantly.<sup>[3]</sup> Hitherto, lithium-ion batteries have demonstrated great success. However, cost is a primary obstacle hindering the mass application of lithium-ion batteries.<sup>[4]</sup> Hence, scientists are attempting to develop other low-cost metal ion batteries (*e.g.*, Na-, K-, and Al-ion batteries).<sup>[5-7]</sup>

Aluminum ranks first in metal content in the Earth's crust. Therefore,

aluminum ion batteries (AIBs) are ideal for solving cost problems. In addition, Al possesses competitive volumetric and gravimetric capacities (2978 mAh g<sup>-1</sup> and 8034 mAh cm<sup>-3</sup>, respectively) to Li anodes (3870 mAh g<sup>-1</sup> and 2080 mAh cm<sup>-3</sup>, respectively).<sup>[8]</sup> Research on aluminum-ion batteries has increased in the last five years, primarily focusing on the development of cathode materials to overcome the higher charge density of Al<sup>3+</sup> or large ionic radius of AlCl<sub>4</sub><sup>-</sup>.<sup>[9]</sup> Currently, the research on cathode materials of aluminum batteries focuses primarily on carbon- and sulfide-based cathode materials that demonstrate significant improvements in performance.<sup>[10-13]</sup> In brief, the present research on cathode materials has focused on developing new compounds or unique material structures. This has inspired us to investigate elemental metal nanoparticles (NPs) as cathode materials for AIBs. To obtain such NPs, a medium for dispersing metal NPs is necessary to inhibit infaust agglomerations. Meanwhile, an effective protective layer for isolating metal NPs and the ambient environment is essential, as metal NPs are generally active. A three-dimensional (3D) network material is an ideal structure option for dispersing metal NPs; however, the reported 3D foam is currently widely used as a current collector (e.g., nickel and copper foams, *etc.*),<sup>[14,15]</sup> and is not appropriate in this study requiring a nonmetallic 3D interconnected framework. In the search for such a 3D material, we found loofa (L) from nature. L is a natural nonmetallic 3D framework-like material with extremely low cost and no pollution.

Two primary approaches can be used for the metal NP loading process:  
i. direct chemical reduction of the metal ions to the surface of L (i.e. wet

chemical method); ii. heat treatment of the precursor in a reducing atmosphere. It is noteworthy that L exhibits a natural carbonaceous feature that requires heat treatment for carbonization in the subsequent preparation process of electrode materials. Hence, the second option is more appropriate and interesting. More importantly, a highly crystallized and defect-free carbon matrix requires a high temperature of up to 3000 °C for heat treatment.<sup>[16]</sup> However, in the presence of metal NPs, the crystallization temperature of carbon is reduced significantly (less than 1000 °C).<sup>[17,18]</sup> Therefore, carbon species are expected to crystallize spontaneously on the surface of metal NPs at a relatively low temperature to, in situ, form a graphite C layer for the protection of the metal NPs.

The remaining effort is to obtain a suitable process and material to grow the precursor of the metal NPs on the L surface. The presence of metallic elements in the precursor has inspired us to consider the currently popular metal-organic frameworks (MOFs). MOFs are promising candidates for linking nonmetallic L and metal ions owing to their special organic bridges. Among the MOFs, Prussian blue analogues (PBAs) exhibit the advantage of rich-C, simple synthesis, and easy mass production at room temperature by a facile wet chemistry method in aqueous base.<sup>[19,20]</sup>

In this study, Fe[Fe(CN)<sub>6</sub>] (FeHCFe), Co[Co(CN)<sub>6</sub>] (CoHCCo), and Co[Fe(CN)<sub>6</sub>] (CoHCFe) as precursors were loaded on the L surface, followed by heat treatment under reducing air (see experimental section for more detailed information). The formed elemental metal NPs

encapsulated by crystallized carbon (Co@C, Fe@C, and CoFe@C) served as cathode materials for the AIBs, indicating a solid-state diffusion-controlled activity toward Al storage.

### **1.6.2. Material preparation**

L was collected from a farm near our campus and washed several times using deionized (DI) water; 0.01 M of two CoCl<sub>2</sub> and one FeCl<sub>3</sub> solutions were prepared in three beakers. Subsequently, the well-cleaned L was soaked into these three solutions. Meanwhile, 0.01 M of one K<sub>3</sub>Co(CN)<sub>6</sub> and two K<sub>3</sub>Fe(CN)<sub>6</sub> solutions were prepared in another three beakers. The solutions mentioned herein were prepared using DI water without any organic additives. After overnight soaking the L in these three salt solutions, K<sub>3</sub>Co(CN)<sub>6</sub> was added to the CoCl<sub>3</sub> solution, and the two K<sub>3</sub>Fe(CN)<sub>6</sub> solutions were added into the FeCl<sub>3</sub> and CoCl<sub>3</sub> solutions, to in-situ grow CoHCCo, FeHCFe, and CoHCFe on the L surface. To avoid the aggregation of Prussian blue analog NPs, the adding procedure was performed dropwise. These mixed solutions were constantly stirred overnight, after which the soaked L was removed followed by rinsing with DI water to remove the loosely attached Prussian blue analog NPs.

The L loaded with CoHCCo, FeHCFe, and CoHCFe was dried in a vacuum oven followed by heat treatment in Ar/N<sub>2</sub> (96/4%) atmosphere at 700 and 900 °C for 1 and 5 h, respectively. The carbonized loofa loaded with metal NPs (Co@C, Fe@C, and CoFe@C) were collected for subsequent characterizations.

### 1.6.3. Material characterizations

The morphologies of the prepared CoHCCo, FeHCFe, CoHCFe, Co@C, Fe@C, and CoFe@C were investigated through field emission-scanning electron microscopy (FE-SEM, Inspect F50) and transmission electron microscopy (TEM, Tecnai F20). Consistent elements of the as-prepared products were qualitatively detected with energy-dispersive X-ray spectroscopy (EDX). A structural study and phase verification were performed through X-ray diffraction (XRD, D8-Advance, fixed incident angle of  $2^\circ$ , equipped with Cu K $\alpha$  radiation). The crystallinities of C derived from the L were measured through Raman spectroscopy (inVia Raman Microscope). The bonding features of C and metal NPs were detected through X-ray photoelectron spectroscopy (XPS, PHI 5000 VersaProbe) using an Al K $\alpha$  source (Sigma probe, VG Scientifics). The thermal stability of the as-prepared carbonized L was investigated through thermogravimetric analysis (TGA) that was performed under an air flow from room temperature to 700 °C with a temperature ramp of 10 °C min<sup>-1</sup>. Inductively coupled plasma (ICP) was used for the quantitative measurement of the amount of metallic element in each sample. The ICP samples were prepared by dissolving Co@C, Fe@C, and CoFe@C into *aqua regia* solutions, followed by ICP measurements. Mesoporous hollows were examined by N<sub>2</sub> gas Brunauer-Emmett-Teller (BET) adsorption-desorption isotherms.

The as-prepared Co@C, Fe@C, and CoFe@C were ground with super P and poly(vinylidene) fluoride in a mass ratio of 7:2:1, after which the

mixed powders were dispersed into a constantly stirred N-methyl-2-pyrrolidinone solution to prepare a uniform slurry for subsequent electrochemical characterizations. The well-prepared slurry was cast on an Pt deposited organic polymer ( $\sim 3 \text{ mg cm}^{-2}$ ) by Referring other literature<sup>[21]</sup> and dried in a vacuum oven at  $80 \text{ }^\circ\text{C}$  overnight to form the final cathode of the AIBs.

The electrochemical properties of Co@C, Fe@C, and CoFe@C were characterized in the pouch cells where the well-dried electrodes were inserted as the cathodes, and Al metal foil (0.5 mm in thickness) was used as the anode. Between the two electrodes, two pieces of glass-fiber papers (Whatman) soaked with 1-Ethyl-3-methylimidazolium chloride ([EMIM]Cl)/AlCl<sub>3</sub> (1/1.3 mole/mole) was inserted to isolate the anode from the cathode.

The electrochemical dynamic performance was characterized with electrochemical impedance spectroscopy (EIS, Im6ex ZAHNER) in the assembled pouch cell with a frequency range of 10 mHz to 1 MHz and a voltage amplitude of 10 mV.

Cyclic voltammetry (CV) measurements were performed in the potential range of 0.05–1.2 V vs. AlCl<sub>4</sub><sup>-</sup>/Al with a scan rate of  $0.5 \text{ mV s}^{-1}$  (WBCS3000, Wonatech, Korea). Galvanostatic charge/discharge cycling measurement was performed between 0.05–1.2 V vs. AlCl<sub>4</sub><sup>-</sup>/Al at various current densities corresponding to 100 and 1,000 mA g<sup>-1</sup>. A long-term lifetime measurement was conducted at the current density of 1,000 mA g<sup>-1</sup>. The current densities and specific capacities herein were

calculated based on the weight of the metallic active materials.

The samples for ex-situ XRD characterizations were prepared by disassembling the pouch cells charged/discharged to 1.2/0.05 V vs.  $\text{AlCl}_4^-/\text{Al}$ , followed by rinsing with sufficient ethanol and drying in a vacuum oven.

#### 1.6.4. Results and discussion

The synthesis procedure of the innovative products was illustrated in Figure 1.33. Sphere-shaped FeHCCo NPs of less than 100 nm were exhibited in the SEM images (Figure 1.34a). Furthermore, the uniform distribution of the consistent elements for each of the NPs were further confirmed by EDX mapping (Figure 1.34b).

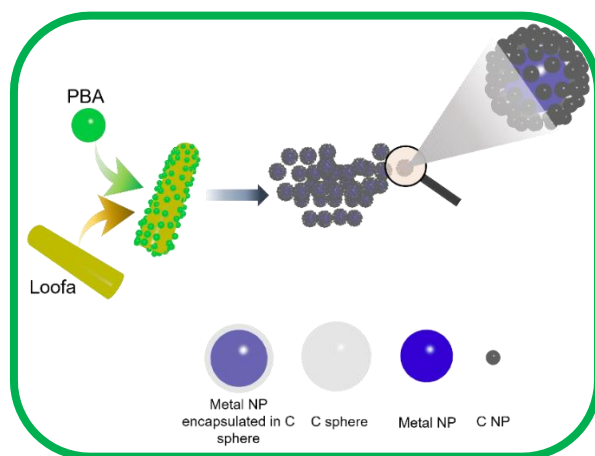


**Figure 1.33.** Synthesis procedure of the C encapsulated metal NPs.

A high specific area is important for the mass loading of CoHCCo, FeHCFe, and CoHCFe. After the in-situ growth of CoHCCo, FeHCFe, and CoHCFe, a significant difference in the L surface is observed (Figure 1.34c,d). The surface of the L was fully covered with the in-situ grown NPs. In addition, the interior of the channels in each L ribbon was well loaded, although a slight reduction in the loading amount was shown. Carbonization is considered as a key procedure to obtain final electrode materials with a well-constructed porous physical structure. In this study, we performed four types of heat-treatment conditions (700 and 900 °C for 1 and 5 h, respectively). Samples annealed at 700 °C for 1 and 5 h exhibit a clogged sponge-like structure. However, some residual species were observed for the CoHCCo-loaded L when treated at 900 °C for 1 h. After the final optimization for the heat-treatment condition (at 900 °C for 5 h), a sponge-like porous C matrix decorated with metal NPs was observed. The same heat-treatment conditions can be obtained for another Fe@C and CoFe@C. The uniformly distributed metal NPs are also demonstrated by the SEM image of a representative CoFe@C (Figure 1.34e) and scanning transmission electron microscopy (STEM, Figure 1.34f), where small metal NPs mired in the C matrix are apparent. The porous C matrix disperses the metal NPs effectively, thus limiting the particle size to ~70 nm (Figure 1.34g,h).

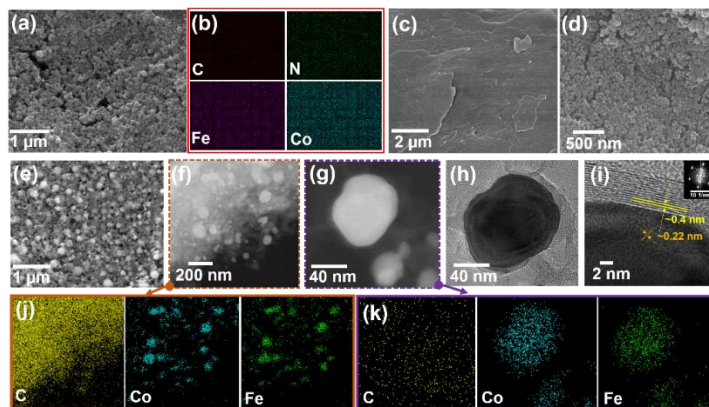


**Figure 1.34.** (a) SEM image and (b) EDX mapping of CoHCFe. SEM images of (c) well-cleaned loofa surface; (d) in-situ grown CoHCFe on the loofa surface. (e–h) SEM, STEM, magnified STEM, and TEM images of CoFe@C. (i) HRTEM of the crystallized CoFe alloy and C layer on the surface. (j,k) EDX mapping of CoFe@C. The CoFe@C was prepared through heating at 900 °C for 5 h.

Such small NPs were expected to enhance the contact surface area with infiltrated electrolytes, facilitating the improvement in use efficiency of the active materials. Magnified STEM and TEM images (Figure 1.34g,h) clearly exhibit that the carbon layers cover the surface of the metal NPs to form a CoFe@C structure. To verify the crystallized condition of C as described in the introduction section, high-resolution TEM (Figure 1.34i) displays the C lattice planes (~15 layers) with an interplanar spacing of ~0.4 nm; this is different from the inside metal NPs with a much smaller interplanar spacing of ~0.22 nm. This highly

crystallized feature was also verified by the fast Fourier transform pattern, in which a single crystal diffraction pattern was clearly observed. The consistent elements for the specially designed materials were detected with EDX mapping (Figure 1.34j,k). The Co, Fe, and C elements were clearly detected in both high and low magnifications, revealing the alloy matrix of the NPs. This in-situ grown carbon layer was expected to protect the integrity of the metal NPs to exhibit an outstanding lifespan.<sup>[22]</sup>

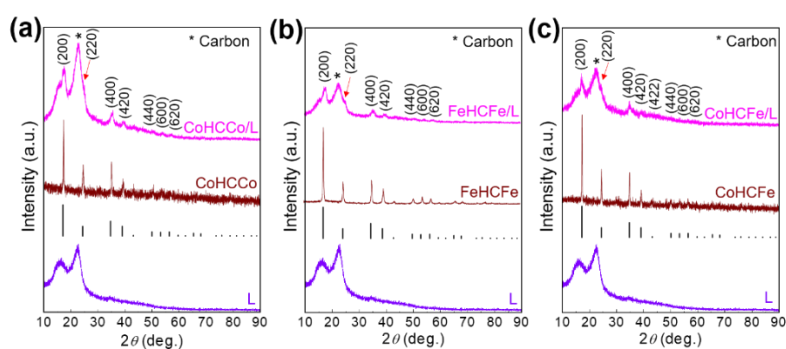


**Figure 1.35.** XRD diffraction patterns of (a) L, CoHCCo, and CoHCCo/L, (b) L, FeHCFE, FeHCFE/L, (c) L, CoHCFE, and CoHCFE/L.

The phase variation during the synthesis process was examined with X-ray diffraction (XRD, Figure 1.35). The characteristic peaks of the CoHCCo, FeHCFE, and CoHCFE were well indexed after in-situ growing on the L surface, demonstrating that the cyanide organic linkers can easily coordinate with L at room temperature in aqueous bath. The generated phase for each sample by heat treatment are shown in Figure

1.36, where C/metal compounds (e.g.,  $\text{Fe}_3\text{C}$ ) were observed when the annealing temperature was set at 700 °C. However, CoHCCo/L and CoHCFe/L exhibit a separated phase, i.e. C and elemental metal, although a  $\text{Fe}_3\text{C}$  phase was shown for FeHCFe/L, when heated at 900 °C for 1 h. In addition, the crystallization of C was slightly improved after carbonization at 900 °C compared to that at 700 °C. We thus employed the parameters (900 °C, 5 h) for subsequent heat treatments. It is not necessary to further enhance the temperature and prolong the processing time as the elemental metals have been obtained. The crystallized C as shown in the TEM image (Figure 1.34i) was further demonstrated by XRD (Figure 1.36a–c), where a sharp (002) peak of C was indexed in the samples with metal NPs encapsulated inside; nevertheless, the naked L after heating displays only an amorphous C hump (Figure 1.36d).

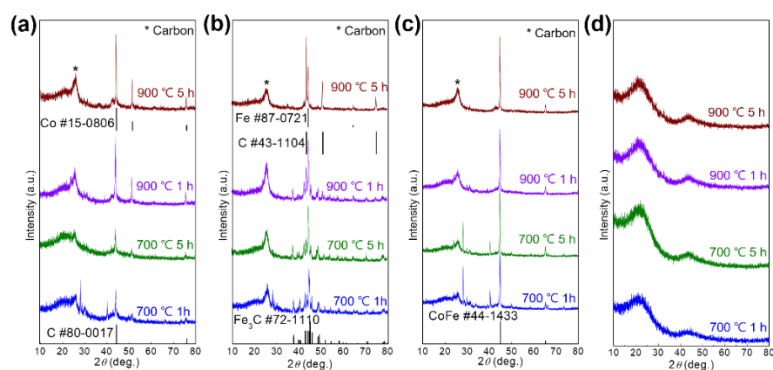


**Figure 1.36.** XRD spectra of carbonized L loaded with (a) CoHCCo, (b) FeHCFe, and (c) CoHCFe at various parameters. (d) Heat-treated naked L without any loading.

The characteristics of C were further studied with Raman spectra (Figure 1.37), where the D-band ( $A_{1g}$  symmetry) caused by the presence of the disordered structure was exhibited at  $\sim 1350\text{ cm}^{-1}$ .<sup>[23]</sup> The typical G-band at  $\sim 1600\text{ cm}^{-1}$  corresponds to the stretching of the C–C bond ( $E_{2g}$  symmetry), and it is typical to all  $sp^2$  carbon systems.<sup>[24]</sup> However, a significant difference in the Raman spectra of L with and without metal NPs is the 2D band corresponding to a graphitic  $sp^2$  mode, which further supported the crystallized C as discussed in the XRD and TEM results (Figure 1.34 and Figure 1.36).<sup>[25-27]</sup> This behavior is absent in the naked L after heat treatment (Figure 1.37d), revealing the disordered C matrix. Several uncertain peaks were observed at wavenumbers less than  $800\text{ cm}^{-1}$  in the Raman spectra (Figure 1.37a–c), and were more likely to be the Reflections of oxidized metal NPs at the metal NPs/C interfaces owing to the electron transfer from metal NPs to C.<sup>[28,29]</sup>

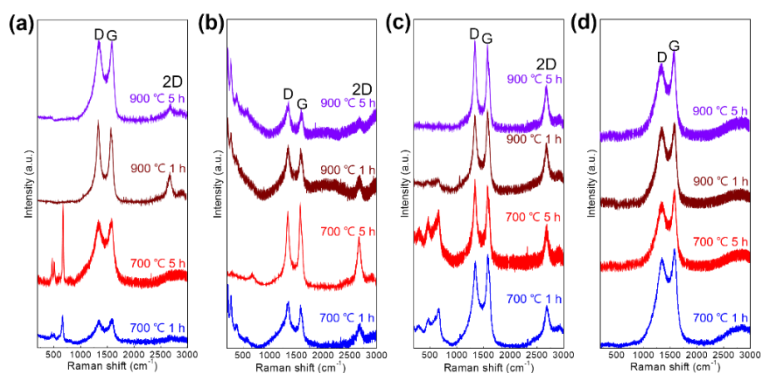


**Figure 1.37.** Raman spectra of (a) Co@C, (b) Fe@C, (c) CoFe@C, and (d) L prepared at diverse carbonization conditions.

The thermal stabilities of the as-prepared Fe@C, Co@C, and CoFe@C were measured using TGA. A slight weight decrease in the initial range owing to the evaporation of water molecules was indicated until  $\sim 400$  °C, where a rapid decrease is resulted from the C burning, emphasizing the adequate reliability of the products when served at room temperature. Consequently, residues of  $\sim 40\%$  for Co@C and CoFe@C, and of  $\sim 30\%$  for Fe@C had remained.

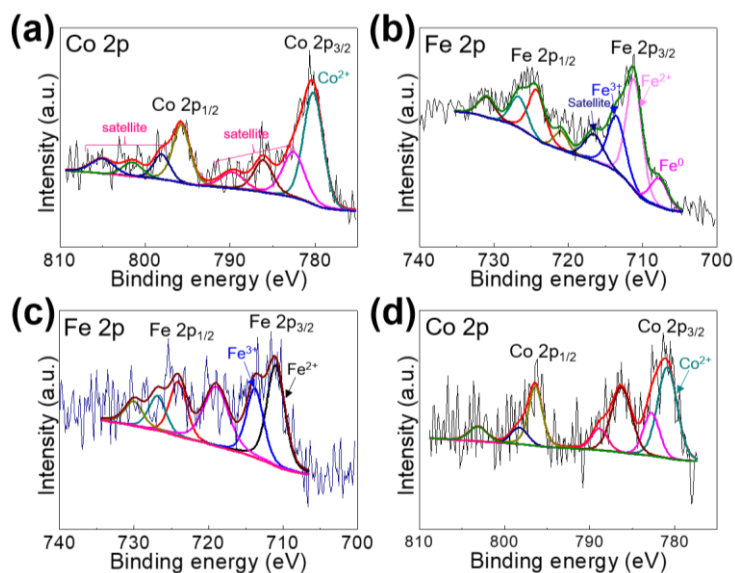


**Figure 1.38.** Deconvoluted XPS spectra of (a) Co 2p for Co@C, (b) Fe 2p for Fe@C, (c) Fe 2p and (d) Co 2p for CoFe@C.

The surface chemical properties of Co@C, Fe@C, and CoFe@C were studied using XPS. The deconvoluted Co 2p and Fe 2p XPS spectra (Figure 1.38) with relatively lower intensities compared with C 1s

confirm the wrapping layer on the surface of the metal NPs, based on the surface chemical characterization feature of XPS, as observed in the SEM and TEM images (Figure 1.34g–i). A further analysis of the deconvoluted Fe 2p and Co 2p exhibits oxidized Co and Fe (Figure 1.38) caused by the electron transfer from the metal element to the surrounding crystallized C wrapping layer, although elemental iron was detected in Fe@C (Figure 1.38b). However, metal elementals (Co, Fe, and CoFe alloy) being dominated phases are confirmed according to the XRD diffraction results (Figure 1.36), indicating that only a small amount of surficial metal atoms bonded with C to promote C crystallization. Thus, it is rational to conclude that the active materials in these composite materials are elemental metal NPs.

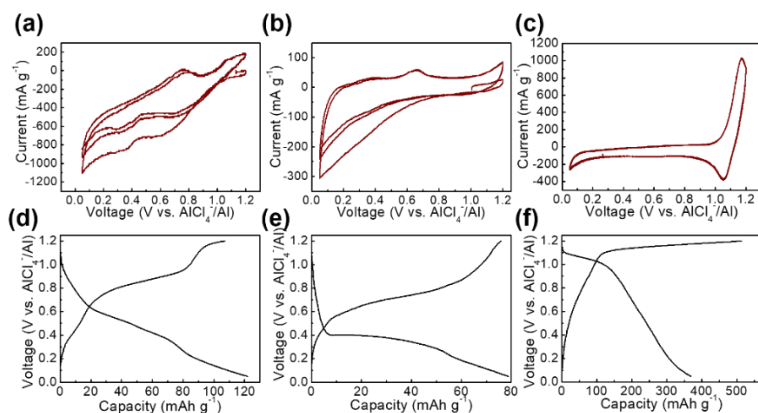


**Figure 1.39.** (a–c) CV curves and (d–f) corresponding charge/discharge voltage profiles of Co@C, Fe@C, and CoFe@C.

A quantitative analysis of the metal elements in Co@C, Fe@C, and

CoFe@C were performed with ICP. Co@C consists of 13 wt.% Co; Fe@C consists of 22 wt.% Fe; CoFe@C consists of 12 wt.% CoFe in the basis of exposed samples.

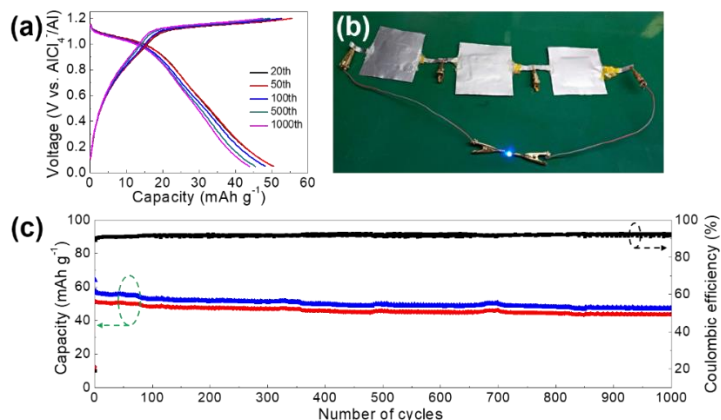


**Figure 1.40.** (a) Representative charge/discharge voltage profiles of CoFe@C at  $1,000 \text{ mA g}^{-1}$ , (b) assembled pouch cells with CoFe@C as cathode material lighting a blue LED lamp, and (c) long-term repeated charge/discharge cycling measurement of CoFe@C at  $1,000 \text{ mA g}^{-1}$ .

The electrochemical properties of Co@C, Fe@C, and CoFe@C were measured in pouch cells, and exhibited an open circuit voltage (OCV) of  $\sim 1 \text{ V vs. AlCl}_4^-/\text{Al}$ . The electrochemical activities of Co@C, Fe@C, and CoFe@C were investigated using CV curves at a scan rate of  $0.5 \text{ mV s}^{-1}$ . The CV curve of Co@C (Figure 1.39a) shows evident discharge peaks at  $\sim 0.6$  and  $0.3 \text{ V vs. AlCl}_4^-/\text{Al}$ , and accordingly, a charge peak at  $\sim 0.8 \text{ V vs. AlCl}_4^-/\text{Al}$ . In addition, the CV curve of Fe@C (Figure 1.39b) exhibits a discharge and charge hump at  $0.39$  and  $0.66 \text{ V vs. AlCl}_4^-/\text{Al}$ ,

respectively. However, the CoFe@C displays a pair of redox peaks at 1.17 V vs.  $\text{AlCl}_4^-/\text{Al}$  (charge process) and 1.04 V vs.  $\text{AlCl}_4^-/\text{Al}$  (discharge process) (Figure 1.39c). A further discussion on the relevant effective electrochemical reactions are provided in the following context. To the best of our knowledge, this is the first example where metal NPs as cathode materials in AIBs exhibit distinct redox peaks, suggesting the electrochemical activity toward Al storage. Furthermore, the potential window of 0.05–1.2 V vs.  $\text{AlCl}_4^-/\text{Al}$  is suitable for subsequent characterizations without obvious decomposition behaviors. In a controlled experiment, we evaluated the error that may be introduced by C, although the electrochemical active potential of C was reported to be  $\sim 2$  V vs.  $\text{AlCl}_4^-/\text{Al}$ .<sup>[30]</sup> No redox peaks were observed in the CV curve of naked C derived from the L, indicating its negligible electrochemical activity.

Galvanostatic charge/discharge was performed at a current density of 100 mA  $\text{g}^{-1}$  for the three samples. The representative voltage profiles of Co@C and Fe@C (Figure 1.39d,e) exhibit discharge plateaus at  $\sim 0.5$  V vs.  $\text{AlCl}_4^-/\text{Al}$  for Co@C and  $\sim 0.4$  V vs.  $\text{AlCl}_4^-/\text{Al}$  for Fe@C, indicating typical electrochemical reaction processes. However, we found that the discharge plateau ( $\sim 1.1$  V vs.  $\text{AlCl}_4^-/\text{Al}$ ) of CoFe@C was much higher than those of Co@C and Fe@C, which facilitates the enhancement in energy density. The cycling measurements for Co@C and Fe@C as the cathode materials of AIBs were performed at a current density of 100 mA  $\text{g}^{-1}$  and exhibited stable charge/discharge cycling. Competitive capacities of 103 mAh  $\text{g}^{-1}$  for Co@C and 75 mAh  $\text{g}^{-1}$  for Fe@C at the

100<sup>th</sup> cycle were obtained with Coulombic efficiencies of 95.5% and 99.7%, respectively. However, compare with other, a 3X higher discharge capacity (372 mAh g<sup>-1</sup>) for CoFe@C was obtained with an undesirable Coulombic efficiency (72%). We thus conducted repeated charge/discharge cycling tests at an enhanced current density (1,000 mA g<sup>-1</sup>) for Co@C, Fe@C and CoFe@C. As depicted in Figure 1.40a, stable discharge plateaus during the long-term cycling test were observed for CoFe@C. Practical pouch-type AIBs assembled with CoFe@C-based cathode materials can lighten a 3-V blue LED (Figure 1.40b). As the test progressed, a capacity of 44 mAh g<sup>-1</sup> was maintained with a Coulombic efficiency of 94.1% achieved at the 1000<sup>th</sup> cycle at a capacity loss of 0.7% in each cycle based on the initial charge capacity of 51 mAh g<sup>-1</sup>, demonstrating the outstanding long life-span performance of CoFe@C as a cathode material for AIBs. However, decreased capacities of 34 mAh g<sup>-1</sup> for Co@C and 27 mA g<sup>-1</sup> for Fe@C are obtained at the 1000<sup>th</sup> cycle. The capacity values are lower than the estimated theoretical one (559 mAh g<sup>-1</sup> for Co@C, 373 mAh g<sup>-1</sup> for Fe@C and 273 mAh g<sup>-1</sup> for CoFe@C implying the high potential for further improvement. The higher capacity of CoFe@C at 100 mAh g<sup>-1</sup> than the estimated one remains unclear. The calculations were performed based on the general alloy phase of Co and/or Fe with Al<sup>[31-33]</sup> and composition content (41% for Co@C, 26% for Fe@C and 39% for CoFe@C) calculated by Referring previously reported methods.<sup>[9,21]</sup>

We may be able to preliminarily pursue the possible electrochemical reactions to be  $xAl^{3+} + 3xe^{-} + Co \leftrightarrow Al_xCo$  for Co@C and  $yAl^{3+} + 3ye^{-}$

+ Fe  $\leftrightarrow$  Al<sub>y</sub>Fe for Fe@C similar to other reports.<sup>[12,22,34]</sup> The dual peaks (cathodic) for Co@C may imply a sequential reactions.<sup>[35]</sup> Accordingly, the possible electrochemical reaction for CoFe@C might be  $\text{CoFe} + z\text{Al}^{3+} + 3z\text{e}^{-} \leftrightarrow \text{Al}_z\text{CoFe}$ . The difference in the electrochemical reaction potentials between the Co@C or Fe@C and CoFe@C might be explained by the species variation.<sup>[36–38]</sup> Therefore, we speculated that the underlying mechanism may be a solid-state diffusion-limited ion insertion/extraction process. However, a further in-depth study is required to provide sufficient evidence.

### 1.6.5. Conclusions

We herein verified the electrochemical activity of elemental metal NPs as cathode materials for AIBs. The metal NPs were formed by in-situ grown PBAs (CoHCCo, FeHCFE, and CoHCFE) on natural and low-cost L surface, followed by carbonization. After heating, a crystallized C wrapping layer formed spontaneously on the surface of the metal NPs. When the formed Co@C, Fe@C, and CoFe@C were used as the cathode materials in AIBs, respectively, the CoFe@C exhibited a superior charge/discharge capacity (372 mAh g<sup>-1</sup>) to others (103 mAh g<sup>-1</sup> for Co@C and 75 mAh g<sup>-1</sup> for Fe@C). The metal NPs demonstrated a stable electrochemical process with apparent discharge plateaus. Typically, CoFe@C would demonstrate an extremely long-term charge/discharge cycling with a capacity decay of 0.7% for each cycle and a Coulombic efficiency of 94.1%. The ex-situ characterization had allowed us to

conclude that the electrochemical activity of the metal NPs toward charge storage was primarily benefitting from a solid-state diffusion-controlled process. This study is expected to contribute toward the realization of low-cost, innovative, and high-performance cathode materials for AIBs.

#### **1.6.6. References**

- [1] Zhang, L. et al. *Adv. Energy Mater.* 2017, 7, 1700034.
- [2] Tan, K. M. et al. *Renew. Sust. Energ. Rev.* 2016, 53, 720.
- [3] Andwari, A. M. et al. *Renew. Sust. Energ. Rev.* 2017, 78, 414.
- [4] Zhang, Y. et al. *Adv. Mater.* 2018, 30, 1706310.
- [5] Hwang, J. Y. et al. *Chem. Soc. Rev.* 2017, 46, 3529.
- [6] Lin, M. C. et al. *Nature* 2015, 520, 324.
- [7] Shokouhimehr, M. et al. *Nanosci. Nanotechnol. Lett.* 2013, 5, 770.
- [8] Sun, H. et al. *Chem. Commun.* 2015, 51, 11892.
- [9] Hu, Y. et al. *Adv. Mater.* 2018, 30, 1703824.
- [10] Wang, S. et al. *Adv. Energy Mater.* 2016, 6, 1600137.
- [11] Chen, H. et al. *Adv. Mater.* 2017, 29, 1605958.
- [12] Wang, S. et al. *ACS Nano* 2016, 11, 469.
- [13] Jung, S. C. et al. *J Phys. Chem. C* 2016, 120, 13384.
- [14] Gu, S. et al. *Energy Storage Mater.* 2017, 6, 9.

- [15] Wang, H. et al. *ACS Appl. Mater. Inter.* 2014, 7, 80.
- [16] Tsubouchi, N. et al. *Energ. Fuel* 2003, 17, 1119.
- [17] Serrano-Esparza, I. et al. *J. Phys. D: Appl. Phys.* 2016, 49, 105301.
- [18] Rodriguez, R. D. et al. *Nanoscale* 2015, 7, 9545.
- [19] Zhang, K. et al. *J. Alloy Compd.* 2019, 791, 911.
- [20] Zhang, K. et al. *Electron Mater. Lett.* 2019, 15, 444.
- [21] Hu, Y. et al. *Adv. Mater.* 2017, 29, 1606132.
- [22] Cai, T. et al. *Energ. Environ. Sci.* 2018, 11, 2341.
- [23] Castiglioni, C. et al. *J. Chem. Phys.* 2001, 115, 3769.
- [24] Saito, R. et al. *Phys. Rev. B* 2001, 64, 085312.
- [25] Gupta, A. et al. *Nano Lett.* 2006, 6, 2667.
- [26] Ferrari, A. C. et al. *Phys. Rev. Lett.* 2006, 97, 187401.
- [27] Pimenta, M. A. et al. *Phys. Chem. Chem. Phys.* 2007, 9, 1276.
- [28] Cabo-Fernandez, L. et al. *Chem. Commun.* 2016, 52, 3970.
- [29] Poudyal, N. et al. *Nanotechnology* 2013, 24, 345605.
- [30] Wu, Y. et al. *Adv. Mater.* 2016, 28, 9218.
- [31] Mondal, D. et al. *J. Alloy Compd.* 2016, 688, 187.
- [32] Konno, T. J., et al. *J. Appl. Phys.* 2001, 90, 3079.
- [33] Zhao, Y. et al. *J. Solid State Chem.* 2019, 276, 232.
- [34] Rehnlund, D. et al. *Energ. Environ. Sci.* 2017, 10, 1350.
- [35] Xiao, L. et al. *Chem. Commun.* 2012, 48, 3321.

- [36] Zhang, W. et al. *J. Am. Chem. Soc.* 2017, 139, 3316.
- [37] Zhao, Y. et al. *Chem. Mater.* 2015, 27, 3096.
- [38] Yu, L. et al. *ACS Appl. Mater. Inter.* 2017, 9, 2516.

## **1.7. Metal-organic framework-derived metal oxide nanoparticles@reduced graphene oxide composites as cathode materials for rechargeable aluminum-ion batteries**

### **1.7.1. Introduction**

With the ever-growing environmental problems and ever-declining storage amounts of fossil energy resources, methods of integrating green and sustainable energy resources (such as solar, tidal, and wind energies) into an electric grid have been intensively researched.<sup>[1-6]</sup> However, a common issue for natural energy resources is the intermittency, which requires the employment of intermediate high-performing and cost-efficient energy storage devices.<sup>[7]</sup> Aluminium-ion batteries (AIBs), as post-lithium-ion batteries, are regarded as potential candidates for the next generation of electric energy storage, owing to the uniquely high charge density ( $\text{Al}^{3+}$ ) and rich substantial reserves in the earth ( $\sim 8000$  ppm,  $< 2.5$  \$  $\text{kg}^{-1}$ ).<sup>[8]</sup> After the significant advance on AIBs made by Dai's group,<sup>[9]</sup> an intensive study on AIBs has been performed, focusing on the development of the cathode materials as an Al metal can be used directly as an anode and the employment of ionic-liquid electrolyte ([EMIM]Cl/ $\text{AlCl}_3$ ) enables stable Al stripping and plating in AIBs. Reliable cathode materials for AIBs which can tolerate the high charge density ( $\text{Al}^{3+}$ ) and large ionic radius of the inserted ion ( $\text{AlCl}_4^-$ ) are important for high-performing AIBs.<sup>[10]</sup> To meet this requirement, research groups have intensively explored C-based materials (e.g.,

defect-free graphene, three-dimensional graphene foam, and natural graphite) among other compounds (e.g., sulfides and selenides).<sup>[11-14]</sup> Studies on the metal-oxide compounds as cathode materials of AIBs assembled with an ionic-liquid electrolyte are rare due to the high electronegativity of O ions. Metal oxides, such as TiO<sub>2</sub> and MoO<sub>3</sub>, are initially demonstrated to be decent cathode materials in aqueous AIBs.<sup>[15,16]</sup> However, further investigation on metal oxides as the cathode materials of non-aqueous AIBs has been overlooked, except a few relevant reports<sup>[17,18]</sup> with inferior electrochemical capacities and limited lifespan. Zhang's group designed CuO microsphere architectures for use as a cathode material of AIBs, demonstrating a rational initial capacity (~250 mAh g<sup>-1</sup>) but a rapid decay (~100 mAh g<sup>-1</sup> at the 100<sup>th</sup> cycle) at a charge/discharge current density of 200 mA g<sup>-1</sup>.<sup>[19]</sup> Their findings, thus, inspire us to conduct an in-depth study on this issue.

Metal-organic frameworks (MOFs) have been demonstrated to be a novel class of original or sacrificial materials for multiple applications, including gas absorption, supercapacitors, and batteries, owing to their porous structures and high surface areas.<sup>[20-22]</sup> The MOFs derived porous and organized electrode materials provide more exposed active sites, short diffusion length, and integrity of the electrode materials during electrochemical reactions. Zhang *et al.* demonstrated porous CuO/Cu<sub>2</sub>O as a high-performance anode material for sodium-ion batteries, exhibiting a

reversible capacity of  $415 \text{ mAh g}^{-1}$  at  $50 \text{ mA g}^{-1}$ .<sup>[23]</sup> Furthermore, Zou *et al.* reported Ni-based MOF-derived NiO/Ni nanocrystals as an advanced anode material of lithium-ion batteries, showing an excellent reversible capacity ( $1144 \text{ mAh g}^{-1}$ ), cyclability, and rate performance.<sup>[24]</sup> Recently, Xu *et al.* used an MOF as a precursor to form carbon-encapsulated selenides as superior anode materials for sodium-ion batteries, with a potential electrochemical property of  $218 \text{ mAh g}^{-1}$  after 500 cycles at a current density of  $3,000 \text{ mA g}^{-1}$ .<sup>[25]</sup> However, reports on MOF-derived metal oxides as cathode materials for AIBs are absent. It is, thus, highly interesting to further study the electrochemical properties of MOF-derived metal oxides as cathode materials for AIBs.

Herein, we demonstrate the advanced electrochemical properties of unit and multiple metal oxides ( $\text{Co}_3\text{O}_4$ @reduced graphene oxide (rGO),  $\text{Fe}_2\text{O}_3$ @rGO, and  $\text{CoFe}_2\text{O}_3$ @rGO) as cathode materials of AIBs, in which the rGO is employed as a wrapping layer to reinforce the material structures. Prussian blue analog (PBA)-type MOF ( $\text{CoCo}(\text{CN})_6$ ,  $\text{FeFe}(\text{CN})_6$ , and  $\text{FeCo}(\text{CN})_6$ ) are employed as the precursors, which can be constructed by a facile co-precipitation process in an aqueous bath without further hydrothermal treatment. It is found that the synthesized metal-oxide samples exhibit superior electrochemical properties as cathode materials for AIBs.

### 1.7.2. Materials preparation

In this report, we synthesized rGO-encapsulated metal-oxide NPs ( $\text{Co}_3\text{O}_4@\text{rGO}$ ,  $\text{Fe}_2\text{O}_3@\text{rGO}$ , and  $\text{CoFe}_2\text{O}_4@\text{rGO}$ ) by a facile spontaneous self-assembly process. The MOF precursors ( $\text{Co}^{2+}$ -hexacyanocobaltate (II),  $\text{Fe}^{2+}$ -hexacyanoferrate (III), and  $\text{Fe}^{2+}$ -hexacyanocobaltate (III)) were prepared by a co-precipitation method in aqueous solutions. After a sufficient precipitation reaction, the collected products were rinsed with deionized water several times to remove impure ions from the reactants. The well-cleaned powders were dried in a vacuum oven overnight, ready for the next usage. The metal-oxide NPs were obtained by heating the as-prepared MOF precursors at  $700\text{ }^\circ\text{C}$  for 5 h in air. An aqueous solution comprising of the oxidized metal NPs and polydiallyl dimethyl ammonium chloride (PDDA, 5% by volume) was prepared. The solution was constantly stirred to uniformly disperse the NPs by surficial electrostatic repulsion. After stirring overnight, the excess PDDA was removed by centrifugation, washing, and re-dispersion in another aqueous solution. Afterwards, a diluted graphene suspension ( $10\text{ g L}^{-1}$ ) was dropwise added to the metal-oxide NPs suspension under constant stirring. This solution was then constantly stirred for further 24 h. During this period, the metal-oxide NPs would spontaneously attach to and be encapsulated by graphene sheets via electrostatic attraction between the positively charged metal-oxide NPs and the negatively charged graphene sheets. The well-assembled products were filtrated and further annealed at  $500\text{ }^\circ\text{C}$  in an argon atmosphere for 2 h.

### 1.7.3. Material characterizations

A structural study was performed via Cu-K $\alpha$  radiation equipped XRD (D8-Advance) at a fixed incident angle of 2°, XPS (PHI 5000 VersaProbe) with an Al-K $\alpha$  source (Sigma probe, VG Scientifics), and Raman spectroscopy (inVia Raman Microscope). Morphologies and constitution elements were demonstrated via SEM (SUPRA 55VP), TEM (JEOL JEM-2100F), EDX mapping, and EPMA. Thermal stability of the as-prepared composites was demonstrated via TGA, which was performed under air flow with temperature ranging from room temperature to 700 °C (10 °C min<sup>-1</sup>). The ratios of rGO and metal oxides were determined with XRF (ZSX-PRIMUS) technique.

The as-prepared samples were manually grinded together with super P and poly(vinylidene) fluoride with a weight ratio of 7:2:1; the mixed powders were then dispersed into a constantly stirred *n*-methyl-2-pyrrolidinon solution to prepare a uniform slurry for the subsequent electrochemical characterizations. The well-prepared slurry was casted on an organic polymer current collector coated with Pt for conductivity, followed by drying in a vacuum oven overnight to be ready for the subsequent electrochemical measurements.

Electrochemical properties were characterized in pouch cells where the well-dried electrodes were inserted as the cathodes and Al metal foils (0.5 mm) were used as anodes. Two pieces of glass-fiber (Whatman) papers soaked with 1-ethyl-3-methylimidazolium chloride

([EMIM]Cl)/AlCl<sub>3</sub> (1/1.3 molar ratio) were inserted between anodes and cathodes for insulation.

An EIS analysis of the CoFe<sub>2</sub>O<sub>4</sub>@rGO cathode material, after a repeated galvanostatic charge/discharge process for 10 cycles at 100 mA g<sup>-1</sup>, was performed by using the Im6ex ZAHNER. A frequency range used was from 10 mHz to 1 MHz, under a constant voltage amplitude of 10 mV.

CV measurements were performed on an electrochemical workstation (WBCS3000, Wonatech, Korea) in potential ranges of 0.05–2.2 and 0.05–1.2 V vs. AlCl<sub>4</sub><sup>-</sup>/Al at a scan rate of 0.5 mV s<sup>-1</sup>. Galvanostatic charge/discharge cycling measurements were performed within potential windows of 0.05–2.2 and 0.05–1.2 V vs. AlCl<sub>4</sub><sup>-</sup>/Al at various current densities of 100, 200 and 1,000 mA g<sup>-1</sup>. Unless otherwise noted, all the current densities and specific capacities in this study were calculated based on the weight of the metal-oxide NP active materials.

Pouch cells with electrodes discharged to desired voltages were disassembled, followed by rinsing the cathodes with ethanol and drying in an oven for ex-situ XRD and EDX characterizations.

#### **1.7.4. Results and discussion**

The synthesis process is illustrated in Figure 1.41. The entire process is performed in an aqueous bath and could be easily mass produced. The morphologies of the prepared Co<sub>3</sub>O<sub>4</sub>@rGO, Fe<sub>2</sub>O<sub>3</sub>@rGO, and

CoFe<sub>2</sub>O<sub>4</sub>@rGO depicted in Figure 1.42 are observed using scanning electron microscopy (SEM) and transmission electron microscopy (TEM). The rGO wrapping layer is clearly observed in the scanning TEM (STEM, Figure 1.42a,d), where almost-transparent graphene sheets are exhibited. Such a phenomenon can be reconfirmed by the TEM morphologies (Figure 1.42b,f). The consistent elements of the final Co<sub>3</sub>O<sub>4</sub>@rGO, Fe<sub>2</sub>O<sub>3</sub>@rGO and CoFe<sub>2</sub>O@rGO are further qualitatively measured by energy-dispersive X-ray spectroscopy (EDX) (Figure 1.42a,e), where the component elements are uniformly distributed over-through each particle.

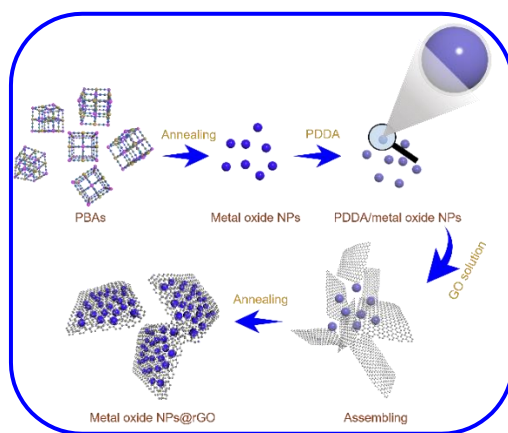


**Figure 1.41.** Schematic illustration of the synthesis process of metal-oxide NPs@rGO.

The same structural and elemental information can also be obtained for Fe<sub>2</sub>O<sub>3</sub>@rGO, which is similar to that of Co<sub>3</sub>O<sub>4</sub>@rGO and

CoFe<sub>2</sub>O<sub>4</sub>@rGO, displaying clear pocket-like rGO-wrapped metal-oxide nanoparticles (NPs). The aligned atoms in the high-resolution TEM (HRTEM) and the corresponding fast Fourier transform diffraction patterns depict well-crystallized natures for Co<sub>3</sub>O<sub>4</sub>@rGO, Fe<sub>2</sub>O<sub>3</sub>@rGO, and CoFe<sub>2</sub>O<sub>4</sub>@rGO (Figure 1.42c,g). The interplanar spacing of Co<sub>3</sub>O<sub>4</sub>@rGO, Fe<sub>2</sub>O<sub>3</sub>@rGO, and CoFe<sub>2</sub>O<sub>4</sub>@rGO measured using HRTEM are 0.58, 0.37, and 0.45 nm, respectively.

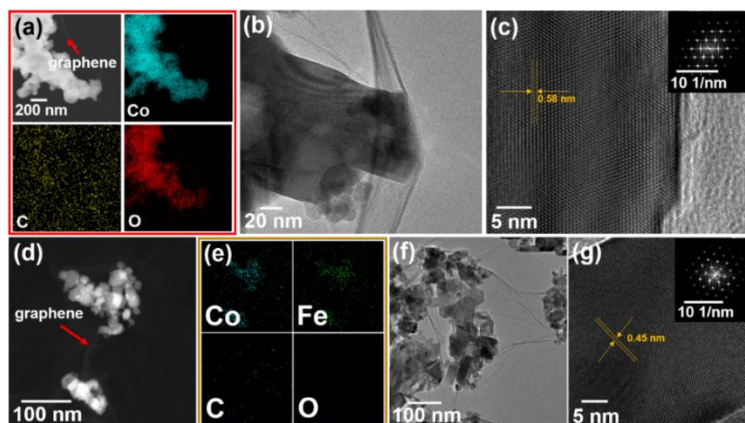


**Figure 1.42.** (a) STEM and EDX mapping, (b) TEM, and (c) HRTEM images of Co<sub>3</sub>O<sub>4</sub>@rGO. (d) STEM, (e) EDX mapping, (f) TEM, and (g) HRTEM images of CoFe<sub>2</sub>O<sub>4</sub>@rGO.

The structures of Co<sub>3</sub>O<sub>4</sub>@rGO, Fe<sub>2</sub>O<sub>3</sub>@rGO, and CoFe<sub>2</sub>O<sub>4</sub>@rGO are observed via X-ray diffraction (XRD) following a contrastive analysis. After facile heat treatments for the pre-prepared PBAs, Co<sub>3</sub>O<sub>4</sub>, Fe<sub>2</sub>O<sub>3</sub>, and CoFe<sub>2</sub>O<sub>4</sub> are formed based on the well-indexed diffraction peaks,

which can be preserved after the introduction of rGO (Figure 1.43). The XRD results of  $\text{Co}_3\text{O}_4@\text{rGO}$ ,  $\text{Fe}_2\text{O}_3@\text{rGO}$ , and  $\text{CoFe}_2\text{O}_4@\text{rGO}$  exhibit combined phases of metal-oxide and rGO (humps at  $\sim 20^\circ$ ). The introduced protective layer (rGO) is further detected with Raman spectroscopy, as shown in Figure 1.43d–f, and the characteristic D and G bands are observed. This indicates well-preserved graphene layers after the self-assembly process in aqueous solutions and annealing processes. The metal-oxide phases in the as-prepared  $\text{Co}_3\text{O}_4@\text{rGO}$ ,  $\text{Fe}_2\text{O}_3@\text{rGO}$ , and  $\text{CoFe}_2\text{O}_4@\text{rGO}$  are further detected with X-ray photoelectron spectroscopy (XPS, Figure 1.44). Co-existing  $\text{Co}^{2+}$  and  $\text{Co}^{3+}$  for  $\text{Co}_3\text{O}_4@\text{rGO}$ ;  $\text{Fe}^{3+}$  for  $\text{Fe}_2\text{O}_3@\text{rGO}$ ;  $\text{Co}^{2+}$  and  $\text{Fe}^{3+}$  for  $\text{CoFe}_2\text{O}_4@\text{rGO}$  are analysed, which indirectly demonstrate the phase results obtained from the XRD spectra.

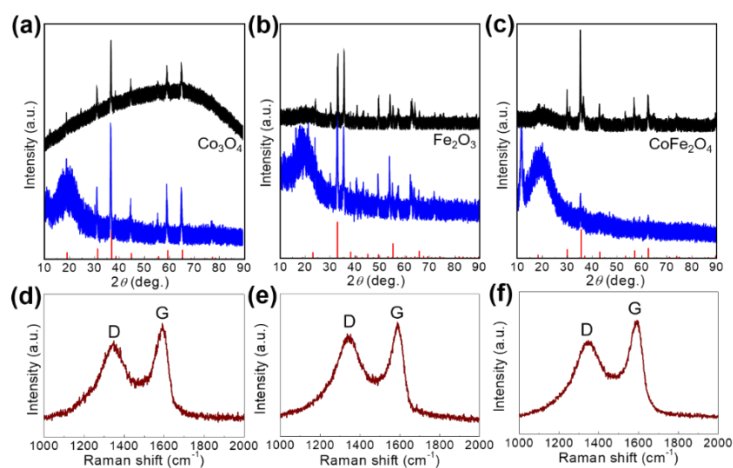


**Figure 1.43.** XRD peaks of (a)  $\text{Co}_3\text{O}_4$  and  $\text{Co}_3\text{O}_4@\text{rGO}$ , (b)  $\text{Fe}_2\text{O}_3$  and  $\text{Fe}_2\text{O}_3@\text{rGO}$ , and (c)  $\text{CoFe}_2\text{O}_4$  and  $\text{CoFe}_2\text{O}_4@\text{rGO}$ . Raman spectra of (d)  $\text{Co}_3\text{O}_4@\text{rGO}$ , (e)  $\text{Fe}_2\text{O}_3@\text{rGO}$ , and (f)  $\text{CoFe}_2\text{O}_4@\text{rGO}$ .

The thermal stabilities of the as-prepared samples were measured via thermogravimetric analysis prior to the electrochemical measurements. Sufficient thermal stabilities until 400 °C for the samples are verified, with less absorbed water species. For the sake of the subsequent electrochemical measurements, the mixture ratios of the three types of materials are measured using X-ray fluorescence (XRF). Besides the qualitative characteristic elements, the metal-oxide NPs/rGO ratios are shown to be 49:51 for  $\text{Co}_3\text{O}_4$ @rGO, 62:38 for  $\text{Fe}_2\text{O}_3$ @rGO, and 40:60 for  $\text{CoFe}_2\text{O}_4$ @rGO. The obtained results are used as Reference values for calculations of the subsequent current densities and specific capacities.

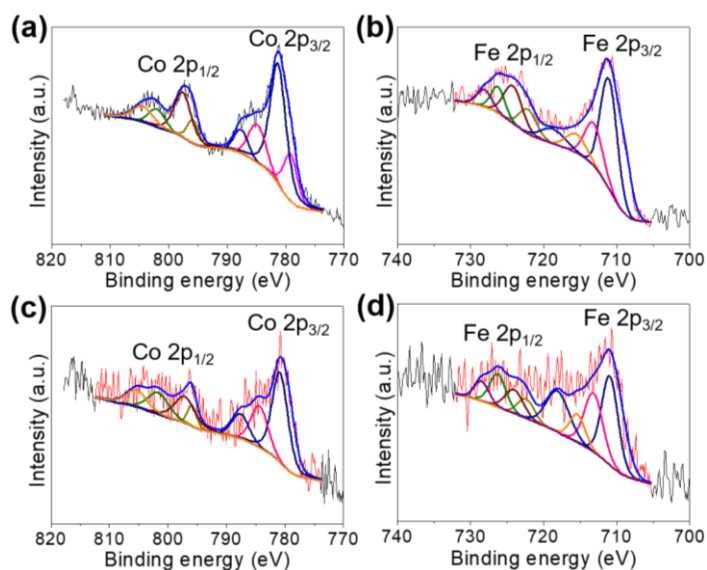


**Figure 1.44.** XPS spectra of (a) Co 2p of the  $\text{Co}_3\text{O}_4$ @rGO, (b) Fe 2p of

the  $\text{Fe}_2\text{O}_3@\text{rGO}$ , and (c) Co 2p and (d) Fe 2p of the  $\text{CoFe}_2\text{O}_4@\text{rGO}$ .

Electrochemically active voltage ranges of the three cathode materials are diagnosed using cyclic voltammetry (CV) curves from 0.05–2.2 V vs.  $\text{AlCl}_4^-/\text{Al}$ , as shown in Figure 1.45, where the redox peaks can be clearly observed for each sample. In particular, two pairs of reduction/oxidation peaks at  $\sim 0.5/0.8$  and  $0.9/1.3$  V vs.  $\text{AlCl}_4^-/\text{Al}$  for  $\text{Co}_3\text{O}_4@\text{rGO}$ ,  $\sim 0.25/0.70$  and  $1.8/2.0$  V vs.  $\text{AlCl}_4^-/\text{Al}$  for  $\text{Fe}_2\text{O}_3@\text{rGO}$ , and  $\sim 0.3/0.8$  and  $1.8/2.0$  V vs.  $\text{AlCl}_4^-/\text{Al}$  for  $\text{CoFe}_2\text{O}_4@\text{rGO}$  are displayed, demonstrating the typical electrochemical-based charge/discharge processes. Furthermore, stage by stage charge/discharge processes are demonstrated by these multiple peaks. We, thus, discharge the electrodes comprising of the as-prepared products to 0.2 and 0.7 V vs.  $\text{AlCl}_4^-/\text{Al}$  for  $\text{Co}_3\text{O}_4@\text{rGO}$ ; 0.1, 0.5, and 1.5 V vs.  $\text{AlCl}_4^-/\text{Al}$  for  $\text{Fe}_2\text{O}_3@\text{rGO}$ ; 0.1, 0.5, and 1.5 V vs.  $\text{AlCl}_4^-/\text{Al}$  for  $\text{CoFe}_2\text{O}_4@\text{rGO}$  to reveal the underlying electrochemical reactions. For which, it is necessary to know how much Al species is inserted in the products in each stage. The effective electrochemical reaction for each stage can be roughly concluded as follows. The same electrochemical reaction in the anode side can be obtained in different electrochemical stages.<sup>[17,18]</sup> In the cathode side, discharge proceeds stage by stage by following the corresponding electrochemical reactions. Al species is inserted into the discharge product formed in the last discharge stage.

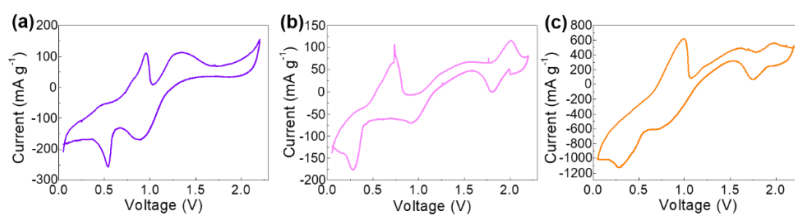


**Figure 1.45.** CV curves of (a)  $\text{Co}_3\text{O}_4@\text{rGO}$ , (b)  $\text{Fe}_2\text{O}_3@\text{rGO}$ , and (c)  $\text{CoFe}_2\text{O}_4@\text{rGO}$  from 0.05–2.2 V vs.  $\text{AlCl}_4^-/\text{Al}$ .

Theoretical capacities of the products are calculated based on the above discussion. As a result, theoretical capacities of  $234 \text{ mAh g}^{-1}$  (based on the weight of  $\text{Co}_3\text{O}_4$  and 0.7 mole of Al insertion),  $1508 \text{ mAh g}^{-1}$  (based on the weight of  $\text{Fe}_2\text{O}_3$  and 1.5 mole of Al insertion), and  $444 \text{ mAh g}^{-1}$  (based on the weight of  $\text{CoFe}_2\text{O}_4$  and 1.3 mole of Al insertion) are obtained.

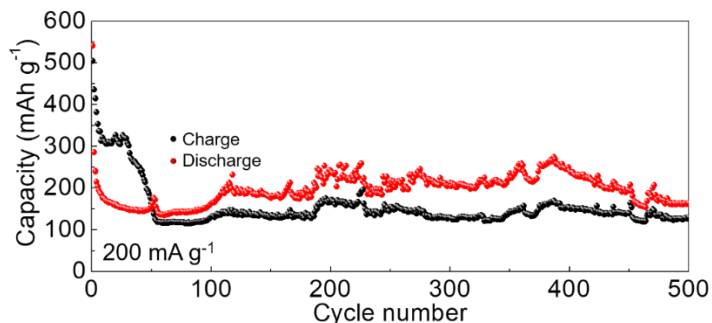


**Figure 1.46.** Repeated charge/discharge cycling measurement for the  $\text{Co}_3\text{O}_4@\text{rGO}$  at  $200 \text{ mA g}^{-1}$ .

Prior to measuring the capacities of the innovative cathode materials, we test the capacity of naked rGO separately. Negligibly small capacity values for naked rGO are obtained, ensuring the capacities of the metal-oxide NPs@rGO samples in the subsequent measurements originate from the metal-oxide active materials. Surprisingly, unprecedented high capacity values for  $\text{Co}_3\text{O}_4$ @rGO are achieved at a current density of  $200 \text{ mA g}^{-1}$  (Figure 1.46), which should be a favourable breakthrough in the attempt of using metal oxides with heavy electronegative O ions as cathode materials for AIBs. After the initial activation phase, an AIB with the  $\text{Co}_3\text{O}_4$ @rGO cathode material proceeds for 500 cycles with a retained discharge capacity of  $168 \text{ mAh g}^{-1}$  and Coulombic efficiency of 76% (Figure 1.46). Notably, this result is quite superior to that of the previously reported CuO microspheres and  $\text{V}_2\text{O}_5$  cathode materials in terms of both capacities and lifespan.<sup>[17,19]</sup> It should be considered that the Al foil can be directly inserted in an anode side without safety concerns, which is quite different from the conventional Li-ion batteries with a requirement of additional consideration for alternatives to Li in an anode side. However, The Coulombic efficiencies increase from 60% to 80% gradually. This relatively low values suggest remain efforts after the primary demonstration for high potentials of metal oxides as cathode materials for rechargeable aluminum-ion batteries in this report.

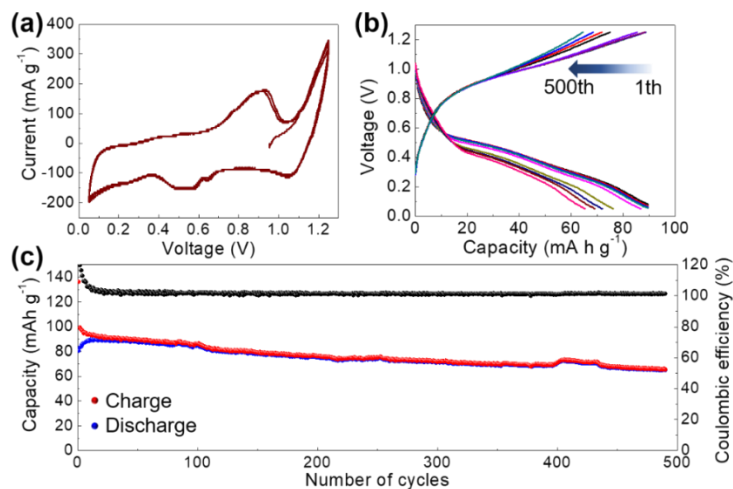


**Figure 1.47.** (a) CV curve of the  $\text{CoFe}_2\text{O}_4@\text{rGO}$  measured within a narrowed potential window of 0.05–1.2 V vs.  $\text{AlCl}_4^-/\text{Al}$ . (b) Representative charge/discharge voltage profiles and (c) capacity values of the  $\text{CoFe}_2\text{O}_4@\text{rGO}$  for continuous charge/discharge at 1,000 mA g<sup>-1</sup>.

$\text{CoFe}_2\text{O}_4@\text{rGO}$  shows a high initial discharge capacity of 407 mA h g<sup>-1</sup> maximum, similar to the  $\text{Co}_3\text{O}_4@\text{rGO}$ . However, a rapid decay of capacities for the  $\text{CoFe}_2\text{O}_4@\text{rGO}$  demonstrates the undesirable electrochemical property. A rational assumption can be due to the deep charge/discharge corresponding to the wide potential range of 0.05–2.2 V vs.  $\text{AlCl}_4^-/\text{Al}$ , which may result in a degradation of polymetallic oxide in  $\text{CoFe}_2\text{O}_4@\text{rGO}$ . We, thus, narrow the potential window from the original range of 0.05–2.2 to 0.05–1.2 V vs.  $\text{AlCl}_4^-/\text{Al}$  for further performance analysis. A pair of obvious redox peaks at ~0.5 (reduction) and 0.9 V vs.  $\text{AlCl}_4^-/\text{Al}$  (oxidation) are clearly detected in the overlapped

(the 1<sup>st</sup> and 2<sup>nd</sup>) CV curves for CoFe<sub>2</sub>O<sub>4</sub>@rGO after an activation operation (Figure 1.47a). Corresponding redox reactions of the redox peaks are pursued following the same method except that the potential window ranges from 0.05 to 1.2 V vs. AlCl<sub>4</sub><sup>-</sup>/Al without covering the electrochemical reactions at 1.8/2.0 V vs. AlCl<sub>4</sub><sup>-</sup>/Al for CoFe<sub>2</sub>O<sub>4</sub>@rGO.

A further long-term charge/discharge demonstration is performed for CoFe<sub>2</sub>O<sub>4</sub>@rGO within the optimized potential window (0.05–1.2 V vs. AlCl<sub>4</sub><sup>-</sup>/Al) at a high current density of 1,000 mA g<sup>-1</sup>. A capacity value of 67 mAh g<sup>-1</sup> at the 500<sup>th</sup> charge/discharge cycle is preserved, corresponding to a retention rate of 74% in comparison with the initial 91 mAh g<sup>-1</sup>, with a high Coulombic efficiency of 99.6% (Figure 1.47c). Notably, voltage profiles during the charge/discharge proceeding are captured and representatively provided in Figure 1.47b, where the undisputed charge/discharge plateaus are observed at ~0.8 and 0.4 V vs. AlCl<sub>4</sub><sup>-</sup>/Al, suggesting that the CoFe<sub>2</sub>O<sub>4</sub>@rGO is more appropriately used within a shallow charge/discharge range and is a potential cathode material for AIBs.

### 1.7.5. Conclusions

In this report, we demonstrate high electrochemical activity of economical metal oxides encapsulated in rGO (Co<sub>3</sub>O<sub>4</sub>@rGO, Fe<sub>2</sub>O<sub>3</sub>@rGO, and CoFe<sub>2</sub>O<sub>4</sub>@rGO) towards Al-ion storage as cathode materials for AIBs. The Co<sub>3</sub>O<sub>4</sub>@rGO displays highly improved electrochemical properties regarding both capacity and lifespan which

are superior to the state-of-the-art metal oxide cathode material currently reported by scientific literature. Besides, the  $\text{CoFe}_2\text{O}_4@\text{rGO}$  exhibits an extremely stable charge/discharge process with a promising Coulombic efficiency of 99.6% after an optimization for the operating voltage range. This report is expected to stimulate further investigation on metal oxides as economical cathode materials for high performance AIBs.

### 1.7.6. References

- [1] Zhang, K. et al. *J. Alloy Compd.* 2019, 791, 911.
- [2] Zhang, K. et al. *Electron. Mater. Lett.* 2019, 15, 444.
- [3] Shokouhimehr, M. et al. *Nanosci. Nanotech. Lett.* 2013, 5, 770.
- [4] Yu, S.-H. et al. *ECS Electrochem. Lett.* 2013, 2, A39.
- [5] Yu, S.-H. et al. *RSC Adv.* 2014, 4, 12087.
- [6] Zhang, K. et al. *ACS Appl. Mater. Inter.* 2019, 11, 31799.
- [7] Wang, S. et al. *Adv. Energy Mater.* 2016, 6, 1600137.
- [8] Zhang, Y. et al. *Adv. Mater.* 2018, 30, 1706310.
- [9] Lin, M.-C. et al. *Nature* 2015, 520, 324.
- [10] Wang, H. et al. *ACS Appl. Mater. Inter.* 2016, 8, 27444.
- [11] Liang, K. et al. *Adv. Energy Mater.* 2019, 9, 1802543.
- [12] Chen, H. et al. *Adv. Mater.* 2017, 29, 1605958.
- [13] Wu, Y. et al. *Adv. Mater.* 2016, 28, 9218.
- [14] Wang, D. Y. et al. *Nat. Commun.* 2017, 8, 14283.

- [15] Liu, Y. et al. *Electrochim. Acta* 2014, 143, 340.
- [16] Lahan, H. et al. *J. Power Sources* 2019, 413, 134.
- [17] Wang, H. et al. *ACS Appl. Mater. Inter.* 2014, 7, 80.
- [18] Chiku, M. et al. *ACS Appl. Mater. Inter.* 2015, 7, 24385.
- [19] Zhang, X. et al. *J. Mater. Chem. A* 2018, 6, 3084.
- [20] Zhang, K. et al. *RSC Adv.* 2019, 9, 21363.
- [21] Li, Z. et al. *Adv. Energy Mater.* 2015, 5, 1401410.
- [22] Zhang, K. et al. *Electron. Mater. Lett.* 2019, 15, 444.
- [23] Zhang, X. et al. *Chem. Commun.* 2015, 51, 16413.
- [24] Zou, F. et al. *ACS Nano* 2015, 10, 377.
- [25] Xu, X. et al. *Adv. Funct. Mater.* 2018, 28, 1707573.

## 1.8. Two-dimensional boron nitride as a sulfur fixer for high performance rechargeable aluminum-sulfur batteries

### 1.8.1. Introduction

Aluminum-ion batteries (AIBs) are considered one of the best potential alternatives to lithium-ion batteries, due in part to Al being one of the most common elements in the Earth's crust, together with its high safety (can be directly inserted as an anode) and a higher reduction potential (-1.76 V versus a standard hydrogen electrode).<sup>[1]</sup> In addition, AIBs have comparable theoretical gravimetric and volumetric capacities (2978 mAh g<sup>-1</sup> and 8034 mAh cm<sup>-3</sup>, respectively)<sup>[2]</sup> to other metal ion batteries.<sup>[3-5]</sup> A successful use of pyrolytic graphite as a cathode of AIBs shows amazing charge and discharge stability (~7000 repeated charge/discharge cycles) and higher discharge voltage (~2 V vs. AlCl<sub>4</sub><sup>-</sup>/Al), although the electrochemical capacity is lower (~60 mAh g<sup>-1</sup>).<sup>[6]</sup> Not surprisingly, research on AIBs is proliferating as many modified and improved cathode materials for AIBs have been reported in the scientific literature<sup>[7-10]</sup> although a lack of suitable cathode materials for AIBs is a significant obstacle for high-energy-density AIBs. Cutting edge research shows a discharge capacity of ~300 mAh g<sup>-1</sup> at a current density of 100 mA g<sup>-1</sup> suggesting new insights and efforts are required for achieving high-performing AIBs.

Inexpensive and extremely high-capacity lithium-sulfur batteries have been intensively studied in the battery research communities with a focus on solving the problem of polysulfide shuttling.<sup>[11-15]</sup> Inspired by the high

electrochemical capacities of lithium-sulfur batteries, a prospect of elemental sulfur as a cathode for AIBs shows an intriguing possibility for seriously enhancing energy densities. Several relevant reports on aluminum-sulfur batteries (ASBs) have shown the anticipated extremely high initial discharge capacity relative to previously documented carbon-based and other composite cathode materials.<sup>[16–19]</sup> However, one of the obstacles to high-performing ASBs is its limited lifespan. According to the report by Cohn *et al.*, ASBs are believed to have an issue of dissolution of discharge products (polysulfide compounds);<sup>[16]</sup> an appropriate fixer of S and polysulfide is thus required to address this impediment.

Two-dimensional materials have been extensively studied for various applications due to large specific surface area and exposed active sites.<sup>[20–25]</sup> The active sites on surfaces of two-dimensional materials may adsorb elemental sulfur and polysulfide compounds to preserve the electrochemical capacities of ASBs and thus improve the life-span by addressing polysulfide dissolution. To authenticate this hypothesis, it is necessary to classify two-dimensional materials into sulfides such as transition-metal dichalcogenides (MoS<sub>2</sub>, WS<sub>2</sub>, etc.) and non-sulfides such as boron nitride (BN) two-dimensional materials.<sup>[26–28]</sup> Recent studies on the use of these two-dimensional materials as electrodes of different types of batteries have shown highly improved performance; such materials deployed in Li-S batteries have been shown to inhibit the dissolution of polysulfide discharge products.<sup>[29–32]</sup> Deng *et al.* demonstrated that graphene supported BN nanosheets displayed an

enhanced adsorption of polysulfide over a wide temperature range via the synergetic interaction of BN and graphene.<sup>[33]</sup> Additionally, these two-dimensional materials can be directly used as electrode materials for batteries.<sup>[34–38]</sup> Wang *et al.* synthesized the hierarchically free-standing WS<sub>2</sub>/carbon nanotube-reduced graphene oxide aerogel via a facile solvothermal method, which exhibited superior electrochemical properties as an anode for Li- and Na-ion batteries. This strategy apparently benefits from the synergetic effect between WS<sub>2</sub> nanosheets and carbon nanotube/reduced graphene oxide scaffold networks and the three dimensional ordered porous structures.<sup>[39]</sup> Motivated by these advanced results, we demonstrate here the effect of both S-containing (MoS<sub>2</sub> and WS<sub>2</sub>) and S-free (BN) layered materials on preserving electrochemical capacities during repeated charge/discharge cycling of ASBs. The incorporation of ball-milled BN/S/C, MoS<sub>2</sub>/S/C, and WS<sub>2</sub>/S/C as cathode materials, respectively, demonstrates a long-term stability and the highest capacity of BN/S/C among the reported cathode materials for AIBs.

### 1.8.2. Material preparation

Commercially available MoS<sub>2</sub> (CAS no. 1317-33-5), WS<sub>2</sub> (CAS no. 12138-09-9), S (CAS no. 7704-34-9), BN (CAS no. 10043-11-5), and super P powders were directly purchased from Sigma-Aldrich. Ball-milling (using zirconia balls) was performed for MoS<sub>2</sub>/S/C (6:1:2, w:w:w), WS<sub>2</sub>/S/C (6:1:2, w:w:w), BN/S/C (6:1:2, w:w:w), MoS<sub>2</sub>/C (7:2,

w:w), WS<sub>2</sub>/C (7:2, w:w), and S/C (1:2, w:w:w) at 1500 rpm for 2 days to mechanically grind the powders while fixing the S powders on the layered MoS<sub>2</sub>, WS<sub>2</sub>, and BN. The ball-milled powders were further manually ground with poly(vinylidene) fluoride (PVDF, binder) in the ratio of 9:1 (w:w) except S/C mixed with PVDF in the ratio of 3:1 (w:w).

### 1.8.3. Material characterizations

Structural study was performed using XRD (D8-Advance equipped with Cu K $\alpha$  radiation at a fixed incident angle of 2 $^{\circ}$ ). The surface chemical properties were analyzed via XPS (PHI 5000 VersaProbe, Al K $\alpha$  source, Sigma probe, VG Scientifics). The morphologies were observed via field emission-SEM (SUPRA 55VP) and TEM (Tecnai F20). Furthermore, EDX, and EPMA were employed for the analysis of constituent elements. The thermal stability was demonstrated via TGA, which was performed under air flow from room temperature to 900  $^{\circ}$ C with a temperature ramp of 5  $^{\circ}$ C min<sup>-1</sup>.

A slurry was prepared by dispersing the mixed powders into a constantly stirred *N*-methyl-2-pyrrolidinone solution. A working electrode with a mass loading of  $\sim 3$  mg cm<sup>-2</sup> was prepared by spreading the slurry, once sufficiently mixed, on a Pt coated OHP organic polymer film current collector, after which the electrode was dried in a vacuum oven at 60  $^{\circ}$ C overnight.

The electrochemical properties were characterized in pouch cells

assembled with the well-dried electrode as a cathode and an Al metal foil (0.5 mm) as an anode. Between two electrodes, glass-fiber paper (Whatman, 1440-070) soaked with 1-ethyl-3-methylimidazolium chloride ([EMIM]Cl)/AlCl<sub>3</sub> (1/1.3, molar:molar) was inserted to isolate the anode and cathode.

CV measurements were performed on an electrochemical workstation (WBCS3000, Wonatech, Korea) in a potential range of 0.05–2.2 V vs. AlCl<sub>4</sub><sup>-</sup>/Al at a scan rate of 0.5 mV s<sup>-1</sup>. Galvanostatic charge/discharge cycling measurement was performed between 0.05–2.2 V vs. AlCl<sub>4</sub><sup>-</sup>/Al at a current density of 100 mA g<sup>-1</sup>. All current densities and specific capacities in the present study were calculated based on the weight of elemental S active material.

EISs of cathode materials were measured with an Im6ex ZAHNER impedance measurement facility in the same pouch cells. Used frequency range was from 10 mHz to 1 MHz with a voltage amplitude of 10 mV.

The samples for ex-situ SEM, EDX, and XRD characterizations were prepared by disassembling the pouch cells (BN/S/C) charged to 0.05 and 2.2 V vs. AlCl<sub>4</sub><sup>-</sup>/Al, respectively, and then cleaning sufficiently with ethanol.

#### **1.8.4. Results and discussion**

The ultimately assembled pouch cell is schematically shown in Figure 1.48. The representative sulfur decorated BN is inserted as a cathode of

an ASB. In the present report, we demonstrate three types of emerging layered materials ( $\text{MoS}_2$ ,  $\text{WS}_2$ , and BN) as hosts to fix sulfur-active materials. After the pre-ball-milling processing, carbon- and S-nanoparticles are adsorbed on surfaces of layered materials. A uniform dispersion for them is observed in the scanning electron microscopy (SEM) and energy-dispersive X-ray (EDX) mapping results (Figure 1.49a,b), together with a qualitative demonstration by electron probe micro-analyzer (EPMA, Figure 1.49c,d) where corresponding elemental peaks are clearly observed. In addition, phases of S,  $\text{MoS}_2$ ,  $\text{WS}_2$ , and BN are well preserved after the ball-milling processing (Figure 1.49e). Furthermore, a transition electron microscopy (TEM) characterization for the employed components (BN, S, and C) is carried out to provide a more comprehensive study. Interplanar spacing of 0.35 nm measured in the high resolution TEM (HRTEM) image for the layered BN demonstrates a good crystallinity of commercial BN as implied in the electron diffraction pattern (Figure 1.49b inset). Furthermore, spherical C nanoparticles with a size of around 100 nm are observed in the TEM images (Figure 1.49c). Amorphous nature of the C is demonstrated in the diffraction pattern displaying circular halos which corresponds to the distorted lattices (Figure 1.49d). Besides, the spherical S particles are also demonstrated by TEM depicting a particle size of around 200 nm after ball-milling (Figure 1.49e,f). To ensure thermal stability during electrochemical measurements, thermogravimetric analysis (TGA) is performed thus verifying the consumption of only C and S at temperatures over 200 °C and without any other side reactions; slight

evaporation of water molecules being the only exception when the temperature is less than 200 °C (Figure 1.50f and Figure 1.51), thus confirming the adequate thermal stability at room temperature.

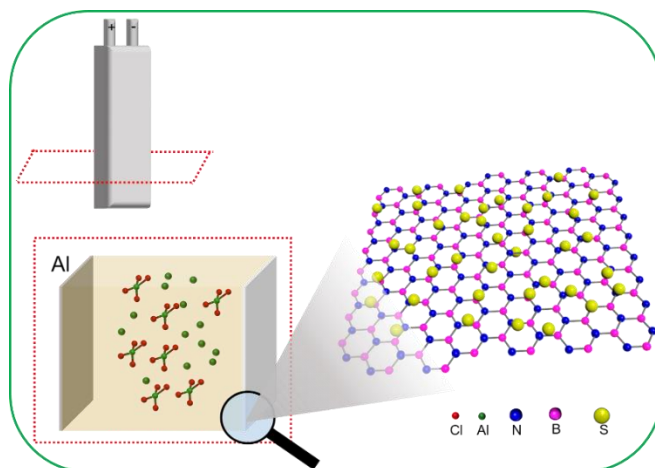


**Figure 1.48.** Schematic illustration of the assembled pouch cell-type ASB, with BN supported S cathode material as an example; one-layered BN here is a representative graphical illustration.

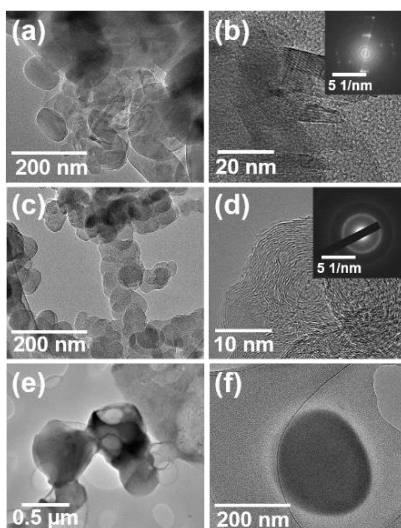


**Figure 1.49.** TEM images of bare (a,b) BN, (c,d) super P, and (e,f) S. Insets depict the electron diffraction patterns.

To determine the subsequent charge/discharge cutoff voltages, a cyclic voltammetry (CV) scan is conducted in which the S reduction peaks at  $\sim 0.8$  and  $2.2$  V vs.  $\text{AlCl}_4^-/\text{Al}$  are displayed (Figure 1.52a). These redox peaks are further shown in another three mixed samples ( $\text{MoS}_2/\text{S}/\text{C}$ ,  $\text{WS}_2/\text{S}/\text{C}$ , and  $\text{BN}/\text{S}/\text{C}$ , Figure 1.52b–d) at similar potentials without other obvious side-reactions. Therefore, in the subsequent electrochemical characterizations, a cutoff voltage of  $0.05$ – $2.2$  V vs.  $\text{AlCl}_4^-/\text{Al}$  is employed.

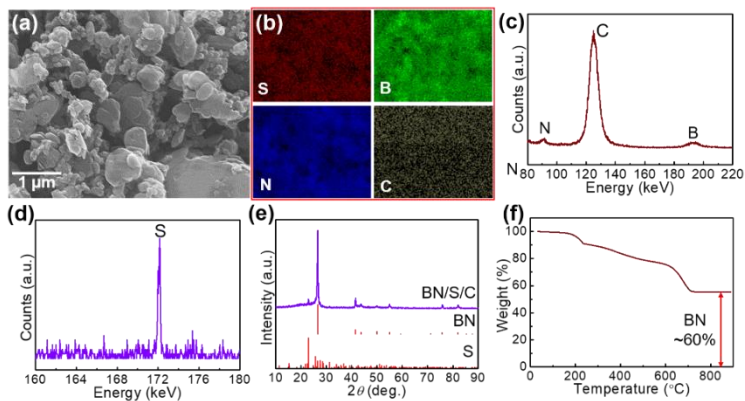


**Figure 1.50.** (a) SEM image, (b) EDX mapping, (c,d) EPMA spectra, (e) XRD spectra, and (f) TGA curve of the BN/S/C sample.

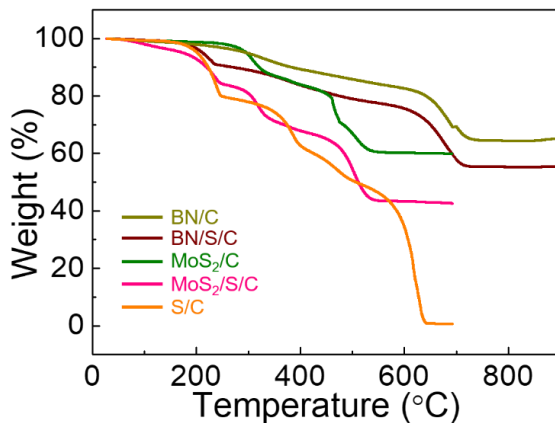


**Figure 1.51.** TGA of the  $\text{MoS}_2/\text{S}/\text{C}$ ,  $\text{MoS}_2/\text{C}$ ,  $\text{S}/\text{C}$ ,  $\text{BN}/\text{S}/\text{C}$ , and  $\text{BN}/\text{C}$  samples demonstrating adequate thermal stability when used as cathode materials for ASBs.

Before measuring the electrochemical capacity of the ball-milled samples, a confirmation of capacities of the bare current collector is

necessary to ensure that the capacities in the subsequent measurements intensively come from the loaded active materials rather than the current collector. The current collector donates negligibly small capacities. Subsequently, capacities of the host materials ( $\text{MoS}_2$ ,  $\text{WS}_2$ , and BN) are measured as cathode materials of ASBs in pouch cells to ensure that these layered materials solely serve as S fixers rather than active materials.

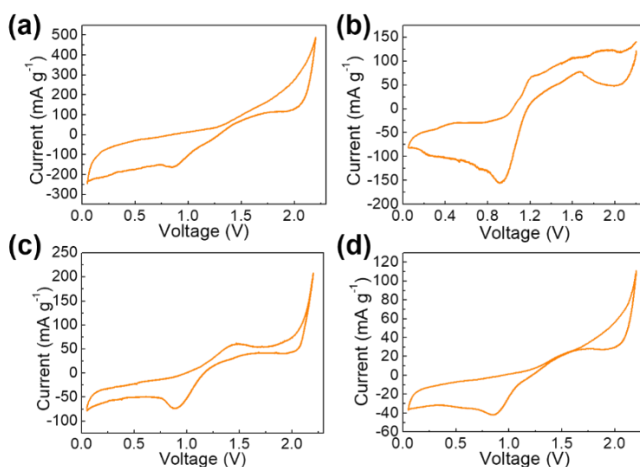


**Figure 1.52.** CV curves of (a) S/C, (b)  $\text{WS}_2$ /S/C, (c)  $\text{MoS}_2$ /S/C, and (d) BN/S/C with a scan rate of  $0.5 \text{ mV s}^{-1}$  and potential window of 0.05–2.2 V vs.  $\text{AlCl}_4^-/\text{Al}$ .

A parallel experiment of S/C as the cathode material of an ASB is conducted for comparison. As seen in the result, S/C (Figure 1.53a) exhibits a rapid decay in capacity ( $\sim 50 \text{ mAh g}^{-1}$  at the 100<sup>th</sup> cycle), although it shows an initial super-high capacity ( $\sim 800 \text{ mAh g}^{-1}$ ).

Correspondingly, the MoS<sub>2</sub>/C, WS<sub>2</sub>/C, and BN/C (Figure 1.53b–d) display negligible capacities in both initial and subsequent repetitions of the charge/discharge cycles (<10 mAh g<sup>-1</sup> after 10 consecutive charge/discharge cycles). This establishes that the adoption of MoS<sub>2</sub>, WS<sub>2</sub>, and BN as support materials agrees with our original proposition of layered materials strictly as S fixers rather than active materials. The effect of MoS<sub>2</sub>, WS<sub>2</sub>, and BN on an inhibition of capacity decay of S is determined by a long-term repeated charge/discharge cycling test. In the case of MoS<sub>2</sub>, a rapid decay from an initial 553 to ~100 mAh g<sup>-1</sup> occurs after the first 20 repeated charge/discharge cycles and further decay until <50 mAh g<sup>-1</sup> after the first 50 repeated charge/discharge cycles (Figure 1.54a) suggests that the S and sulfide compounds may not be captured by the layered MoS<sub>2</sub> via a facile ball-milling process. Similar result of negligibly small capacities for the WS<sub>2</sub>/S/C sample is exhibited in Figure 1.54b where the initial discharge capacity decreases from 526 mAh g<sup>-1</sup> to 54 mAh g<sup>-1</sup> after the first 25 repeated charge/discharge cycles. In contrast, a completely different result is displayed for BN/S/C (Figure 1.54c). A capacity of 532 mAh g<sup>-1</sup> and Coulombic efficiency of 94.3% at the 300<sup>th</sup> charge/discharge cycle have been obtained, although the initial capacity is similar to those of MoS<sub>2</sub>/S/C and WS<sub>2</sub>/S/C.

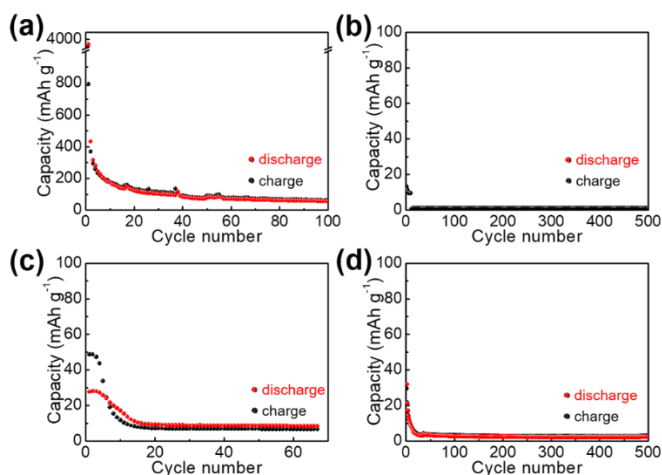


**Figure 1.53.** Repeated galvanostatic charge/discharge cycling measurements for (a) S/C, (b) WS<sub>2</sub>/C, (c) MoS<sub>2</sub>/C, and (d) BN/C within a potential window of 0.05–2.2 V vs. AlCl<sub>4</sub><sup>-</sup>/Al.

To the best of our knowledge, this is the highest capacity value for any graphite-based or other composite cathode materials used for AIBs. This work achieves an unprecedented long-term charge/discharge cycling stability for ASBs.

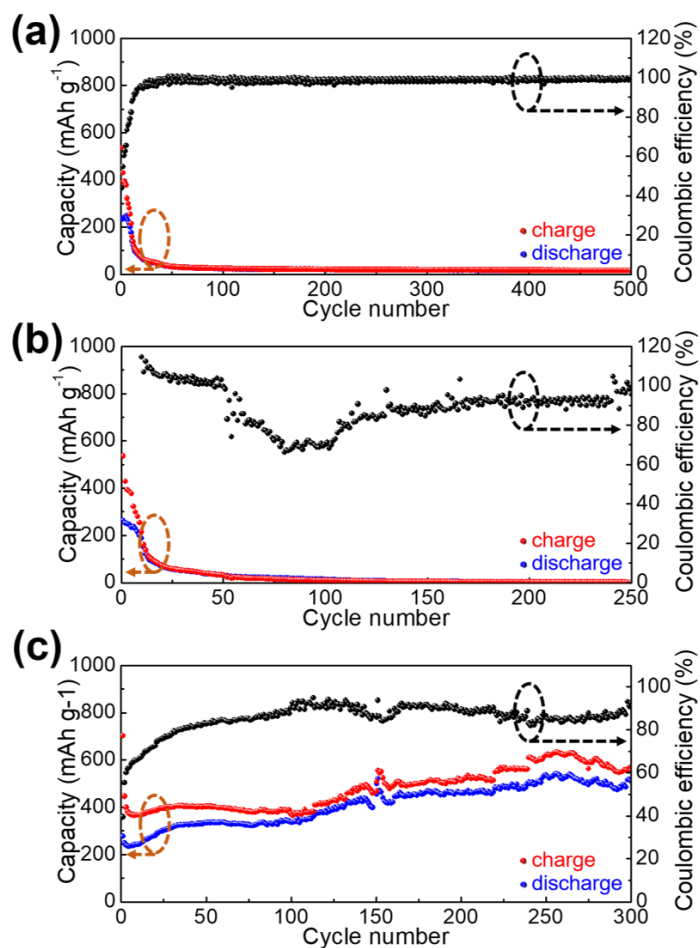


**Figure 1.54.** Long-term repeated charge/discharge cycling measurements for (a) MoS<sub>2</sub>/S/C, (b) WS<sub>2</sub>/S/C, and (c) BN/S/C at a current density of 100 mA g<sup>-1</sup> within a potential window of 0.05–2.2 V vs. AlCl<sub>4</sub><sup>-</sup>/Al.

In another striking result, a clear discharge plateau (~1.15 V vs. AlCl<sub>4</sub><sup>-</sup>

/Al) is shown in each charge/discharge cycle (Figure 1.55a) which is quite different from other discharge plateau-free composite cathode materials for AIBs reported in scientific literature.<sup>[2,7,40,41]</sup> The high-performing ASB shows an open circuit voltage of 1.2 V vs.  $\text{AlCl}_4^-/\text{Al}$  (Figure 1.55b). Notably, the low-cost BN/S/C, prepared by a facile ball-milling process, displaying such high performance is quite attractive for practical applications, although subsequent studies on other properties such as rate performance are warranted.

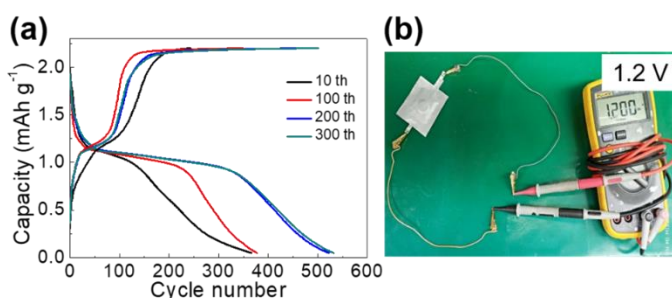


**Figure 1.55.** (a) Voltage profiles of BN/S/C at diverse charge/discharge cycles corresponding Figure 2.54c. (b) An assembled  $\text{Al}/[\text{EMIM}]\text{Cl}/\text{AlCl}_3//\text{BN/S/C}$  pouch cell with an open circuit voltage of 1.2 V vs.  $\text{AlCl}_4^-/\text{Al}$ .

If the underlying mechanism for this well-preserved capacity is consistent with our previous assumption, there should be certain variations in the bonding nature to be reflected in X-ray photoelectron spectroscopy (XPS) results. To test this hypothesis, we performed XPS analysis for the representative  $\text{MoS}_2/\text{S/C}$ , where no obvious peak shift is

revealed for any of the constituent elements (C, Mo, S, and O), indicating the bonding-free feature between S and MoS<sub>2</sub>. However, as we expected, the deconvoluted S 2s peaks of BN/S/C clearly shows a shift towards lower binding energy after ball-milling (Figure 1.56a), demonstrating the electron adsorption from another component (C or BN). Furthermore, peaks of deconvoluted B 1s and N 1s of the BN/S/C sample shift toward higher binding energy than that of the BN/C sample (Figure 1.56b,c) verifying the electron loss of N and B elements. To rule out other possibilities, that the electron transfer may be related to other elements such as C and O, we further analyzed the deconvoluted C 1s and O 1s (Figure 1.56d) where almost consistent peak locations are observed. Thus, we conclude that the ball-milling processing for BN/S/C promotes electron transfer from BN to S. In other words, this facile ball-milling treatment facilitates bonding between S and BN, which can fix the sulfide compounds formed during repeated charge/discharge cycling tests. The structural feature of BN/S/C can be further expounded by TEM images and elemental mapping. The constituent elements of BN/S/C are clearly detected in TEM elemental mapping (Figure 1.57a,b) where, excluding the inherent B, N, and C elements, the loaded S is uniformly distributed throughout samples. The bonding between BN and S can be further inferred by the distortion of BN lattices in HRTEM (Figure 1.57c) where a disordered behavior unlike the circle-like lattice of C (Figure 1.57d) is depicted compared to other well-preserved BN with a lattice spacing of 0.35 nm measured in HRTEM image.

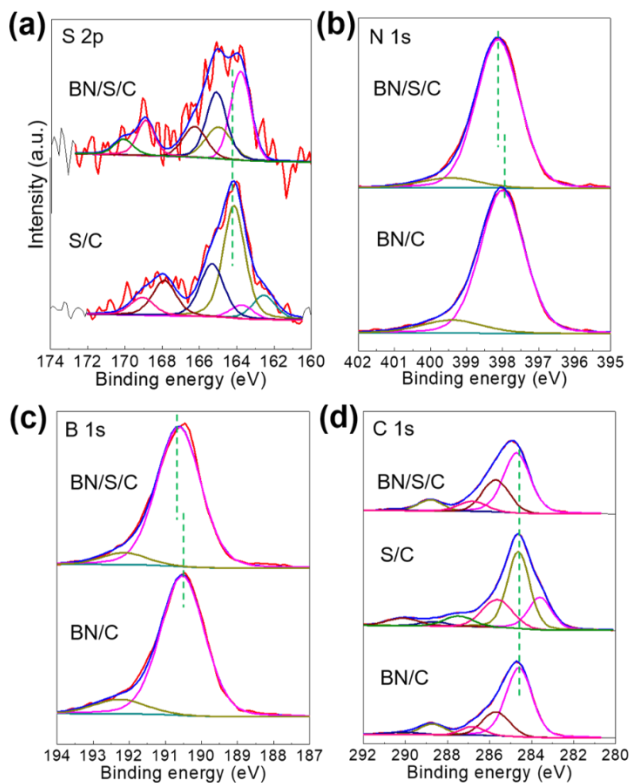


**Figure 1.56.** Deconvoluted XPS spectra (a) S 2p, (b) N 1s, (c) B 1s, and (d) C 1s of BN/S/C.

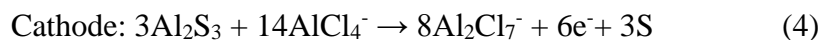
To further reveal the underlying electrochemical reaction mechanism of BN/S/C, we carried out an elemental analysis for such samples charged and discharged till 2.2 and 0.05 V vs.  $\text{AlCl}_4^-/\text{Al}$ , respectively. The elements are consistently distributed throughout the powders, together with Al and Cl from remaining electrolytes and sulfide compounds. Furthermore, the formed sulfide compounds can be also

found in the ex-situ XRD results of BN/S/C at different charge states (Figure 2.58a–d). In which, the formed  $\text{Al}_2\text{S}_3$  in discharge products is indexed at discharge states of both 0.05 and 0.7 V vs.  $\text{AlCl}_4^-/\text{Al}$ . Thus, the effective charge/discharge reactions of batteries, based on the above discussion and other literature,<sup>[17,18]</sup> are formulated by the following equations.

Discharge process



Charge process



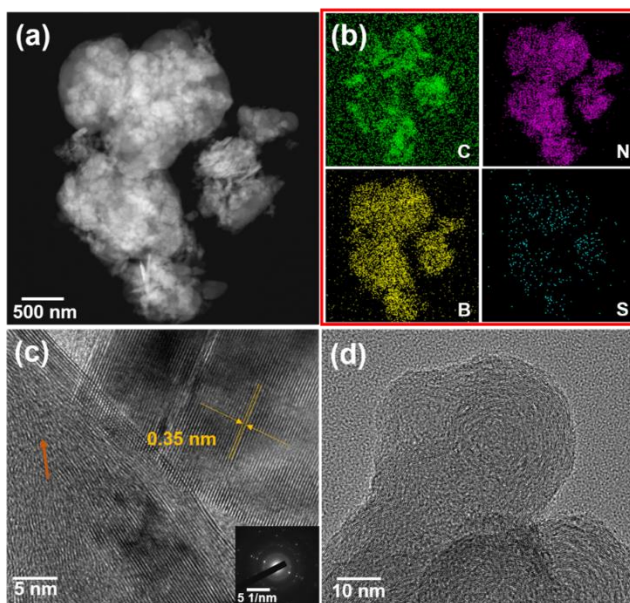


**Figure 1.57.** (a) TEM image, (b) EDX mapping, (c) HRTEM image of BN, and (d) HRTEM image of C in the BN/S/C sample.

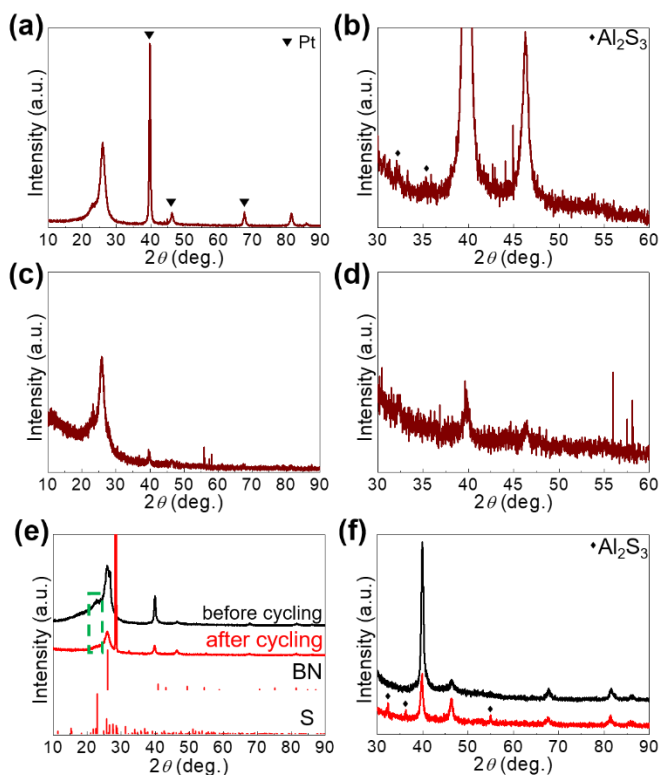


**Figure 1.58.** XRD spectra of BN/S/C discharged to (a,b) 0.05 V vs. AlCl<sub>4</sub><sup>-</sup>/Al and (c,d) 0.7 V vs. AlCl<sub>4</sub><sup>-</sup>/Al. (e) XRD spectra of BN/S/C before and after the repeated charge/discharge cycling measurement. S peak in the fresh electrode disappears after charge/discharge cycling test, while layered BN is well preserved. (f) Magnified XRD spectra of BN/S/C where the formed Al<sub>2</sub>S<sub>3</sub> phase during discharge process is detected.

BN in cathode materials is well preserved after a cycling test (Figure 1.58e). Furthermore, a disappearance of elemental S diffraction peak in

the cathode after a cycling test (Figure 1.58e) suggests the formation of sulfide compounds as shown in Figure 1.58f, where the formed discharge product  $\text{Al}_2\text{S}_3$  is well indexed.<sup>[42]</sup> These analyses further support the proposed effective electrochemical reaction mechanism (Equation 1–4).

### 1.8.5. Conclusions

In this report, we synthesized and comprehensively studied the immobilization effect of layered  $\text{MoS}_2$ ,  $\text{WS}_2$ , and BN to S and sulfide compounds, and established that BN is a promising fixer to protect capacities of S from decaying by bonding with S and/or sulfide compounds. As a result, the unprecedented highest capacity is achieved for BN/S/C:  $532 \text{ mAh g}^{-1}$  with a Coulombic efficiency of 94.3 % and a discharge voltage plateau at  $\sim 1.15 \text{ V}$  vs.  $\text{AlCl}_4^-/\text{Al}$  when charged/discharged at a current density of  $100 \text{ mA g}^{-1}$ . In addition, an unparalleled long-term life-span of 300 cycles is achieved for ASBs. The BN/S/C is validated to be superior to other reported cathode materials for rechargeable ASBs.

### 1.8.6. References

- [1] Zhang, Y. et al. *Adv. Mater.* 2018, 30, 1706310.
- [2] Cai, T. et al. *Energ. Environ. Sci.* 2018, 11, 2341.
- [3] Zhang, K. et al. *Electron. Mater. Lett.* 2019, 15, 444.

- [4] Zhang, K. et al. *J. Alloy Compd.* 791, 2019, 911.
- [5] Zhang, K. et al. *RSC Adv.* 2019, 9, 21363.
- [6] Lin, M.-C. et al. *Nature* 2015, 520, 324.
- [7] Wang, S. et al. *Adv. Energy Mater.* 2016, 6, 1600137.
- [8] Chen, H. et al. *Adv. Mater.* 2017, 29, 1605958.
- [9] Wu, Y. et al. *Adv. Mater.* 2016, 28, 9218.
- [10] Hu, Y. et al. *Adv. Mater.* 2017, 29, 1606132.
- [11] Zhuang, T.-Z. et al. *Small* 2016, 12, 381.
- [12] Liu, D. et al. *Adv. Sci.* 2018, 5, 1700270.
- [13] Hua, W. et al. *ACS Nano* 2017, 11, 2209.
- [14] Liu, M. et al. *Small* 2017, 13, 1602539.
- [15] Shyamsunder, A. et al. *Angew. Chem. Int. Edit.* 2017, 56, 6192.
- [16] Cohn, G. et al. *J. Power Sources* 2015, 283, 416.
- [17] Gao, T. et al. *Angew. Chem. Int. Edit.* 2016, 55, 9898.
- [18] Yang, H. et al. *Angew. Chem. Int. Edit.* 2018, 57, 1898.
- [19] Yu, X. et al. *Chem* 2018, 4, 586.
- [20] Kwon, K. C. et al. *Small Methods* 2019, 3, 1800492.
- [21] Maleki, M. et al. *RSC Adv.* 2016, 6, 51426.
- [22] Lee, I. et al. *J. Catal.* 2015, 36, 1799.
- [23] Zhang, K. et al. *Nano Converg.* 2019, 6, 6.
- [24] Zhang K. et al. *Res. Chem. Intermediat.* 2019, 45, 599.
- [25] Hasani, A. et al. *J. Mater. Chem. A* 2019, 7, 430.

- [26] Maleki, M. et al. *Eur. J. Inorg. Chem.* 2015, 14, 2478.
- [27] Maleki, M. et al. *RSC Adv.* 2015, 5, 6528.
- [28] Maleki, M. et al. *RSC Adv.* 2015, 5, 46823.
- [29] Wang, X. et al. *Adv. Energy Mater.* 2015, 5, 1501106.
- [30] Zhao, C. et al. *ACS Appl. Mater. Inter.* 2016, 8, 2372.
- [31] Fan, Y. et al. *Adv. Energy Mater.* 2017, 7, 1602380.
- [32] Fan, Y. et al. *ACS Appl. Energy Mater.* 2019, 2, 2620.
- [33] Deng, D. R. et al. *ACS Nano* 12, 2018, 11120.
- [34] Li, J. et al. *Nano Energy* 2015, 16, 10.
- [35] Hu, A. et al. *ACS Appl. Mater. Inter.* 2018, 10, 34077.
- [36] Zhou, J. et al. *ACS Nano* 2015, 9, 3837.
- [37] Liu, Y. et al. *ACS Nano* 2016, 10, 8821.
- [38] Tzadikov, J. et al. *ChemSusChem* 2018, 11, 2912.
- [39] Wang, Y. et al. *Adv. Energy Mater.* 2016, 6, 1601057.
- [40] Wang, S. et al. *ACS Nano* 2016, 11, 469.
- [41] Reed, L. D. et al. *Chem. Commun.* 2015, 51, 14397.
- [42] Akhgar, B. N. et al. *J. Alloy Compd.* 2016, 657, 144.

## **1.9. Realization of lithium-ion capacitors with enhanced energy density via the use of gadolinium hexacyanocobaltate as a cathode material**

### **1.9.1. Introduction**

The diminution of fossil fuel resources and the increasing severity of environmental challenges highlight the need for integrating green, sustainable, and renewable energy resources into the electricity supply grid.<sup>[1–3]</sup> However, the intermittent nature and uneven geographical distribution of these clean energy sources necessitate the use of energy storage devices<sup>[4–7]</sup> such as Li-ion batteries (LIBs). Compared to other metal-ion batteries (*e.g.*, Na-, K-, Mg-, and Al-ion), LIBs exhibit fast electrochemical kinetics due to the small ionic radius (3.82 Å in diameter) and low charge of Li<sup>+</sup>.<sup>[8–10]</sup> This advantage has inspired researchers to develop advanced hybrid Li-ion capacitors, which generally comprise battery-type anodes and capacitor-type cathodes exhibiting high potential energy and power densities.<sup>[11,12]</sup> To date, much effort is directed at the optimization of hybrid Li-ion capacitor anodes to improve capacity and rate performance,<sup>[13–16]</sup> while activated carbon or functional carbon-based materials (*e.g.*, graphene) are still widely employed as cathode materials.<sup>[17–19]</sup> The low capacity/capacitance of these carbon-based materials significantly hinders the further development of high-performance hybrid Li-ion storage devices, and the improvement of

cathode material capacity to match that of functional anode materials is a primary demand. Therefore, better materials are still sought after.

Prussian blue analogues (PBAs) have received extensive attention in the field of electrical energy storage due to the capability of their unique crystal structure to accommodate other metal ions *e.g.*,  $\text{Al}^{3+}$ ,  $\text{K}^+$ ,  $\text{Li}^+$ , and  $\text{Na}^+$ .<sup>[20–33]</sup> However, PBAs are poor Li-ion capacitor or LIB electrode materials, typically exhibiting capacities of less than  $200 \text{ mAh g}^{-1}$ . As the first step of enhancing the electrochemical performance of these cathode materials, we closely examined the reported PBAs, revealing that most of them contain fourth-row transition metal ions with 5 d-orbitals realizing various oxidation states.<sup>[34,35]</sup> This finding inspired us to employ metals frequently overlooked such as lanthanides to construct new type of PBAs.<sup>[36]</sup> Gadolinium (Gd), extensively used for the medical imaging, forms a stable trivalent state and salts that are well soluble in water, which allows Gd-based PBAs to be prepared at room temperature by wet chemical methods. Herein, we report a new type of PBA, Gd hexacyanocobaltate:  $\text{GdCo}(\text{CN})_6$  denoted as GdHCCo, that featured an orthorhombic crystal structure instead of the conventional face-centered cubic structure and was therefore expected to exhibit distinctive properties when applied for Li-ion storage as a cathode material. The above compound displayed an excellent capability for Li-ion storage, featuring capacities of up to  $352 \text{ mAh g}^{-1}$  (almost twice higher than that of previously described carbon-based cathode materials for Li-ion capacitors), and therefore being one of the best electrode materials in the PBAs family. Analysis performed by multiple ex-situ techniques

demonstrated that Li-ion storage in GdHCCo is highly reversible and follows a hybrid mechanism. To the best of our knowledge, this study is the first account of using a lanthanide-based PBA as a cathode material for Li-ion storage and presents a breakthrough in the application of PBAs as electrode materials for Li-ion storage.

### **1.9.2. Material preparation**

GdHCCo nanoparticles were prepared by a co-precipitation procedure. Briefly, aqueous  $\text{Gd}(\text{NO}_3)_3$  (Sigma-Aldrich; 0.03 M, 100 mL) and  $\text{K}_3\text{Co}(\text{CN})_6$  (Sigma-Aldrich; 0.03 M, 100 mL) solutions were simultaneously dropwise added to deionized  $\text{H}_2\text{O}$  (200 mL), and the mixture was vigorously stirred at 80 °C to facilitate crystal growth. After the formation of a white precipitate, the mixture was cooled down to room temperature, filtered, and the filter cake was rinsed several times with large amounts of deionized water (to remove impurity ions such as  $\text{K}^+$ ). Finally, the product was dried in a vacuum oven at 60 °C.

### **1.9.3. Material characterizations**

Sample structure was elucidated by X-ray diffraction (XRD) using a Bruker D8 Advance diffractometer. X-ray photoelectron spectroscopy (XPS) was carried out by using an Al  $K_\alpha$  source (PHI 5000 VersaProbe, Japan). Raman and Fourier transform infrared (FT-IR) spectra were recorded using a LabRAM HV Evolution, and a Nicolet iS50, respectively. Field emission scanning electron microscopy (FESEM)

was utilized for the composition and morphology study of the sample using a SUPRA 55VP. Transmission electron microscope (TEM) images were acquired using a JEOL JEM-F200 having an energy-dispersive X-ray spectroscopy (EDX). The thermal stability of the as-prepared GdHCCo was probed by thermogravimetric analysis (TGA) that was performed by heating at a rate of  $10\text{ }^{\circ}\text{C min}^{-1}$  from 25 to  $600\text{ }^{\circ}\text{C}$  in a flow of  $\text{N}_2$ . Quantitative elemental analysis was accomplished by X-ray fluorescence (XRF) utilizing ZSX-PRIMUS.

A slurry including GdHCCo, carbon black (Super P Li), and poly(vinylidene difluoride) (7:2:1, w/w/w) was prepared by grinding the powders and re-dispersing them in *N*-methyl-2-pyrrolidinone, similar to the standard procedure of slurry preparation widely employed in battery research communities and by battery manufacturers. The mixed powders were dried overnight prior to *N*-methyl-2-pyrrolidinone addition at  $80\text{ }^{\circ}\text{C}$  in a vacuum oven. The weight of samples was monitored before and after drying to ascertain the water evaporation as much as possible. A working electrode was prepared ( $\sim 3\text{ mg cm}^{-2}$  mass loading) on a graphite paper current collector (Alfa Aesar) by spreading the slurry and subsequent drying in a vacuum oven at  $60\text{ }^{\circ}\text{C}$ .

A two-electrode cell comprising a GdHCCo working electrode and sufficient Li metal foil (to determine that capacity was restricted only by the GdHCCo mass) was flooded with a 1.0 M solution of  $\text{LiPF}_6$  in a 1:1 (v/v) mixture of diethylene carbonate and ethylene carbonate acquired in a glove box filled with Ar.

Prior to electrochemical characterization, the fresh electrode was subjected to electrochemical impedance spectroscopy (EIS) measurements (IM6ex ZAHNER Elektrik; frequency range = 10 mHz – 1 MHz, amplitude = 10 mV).

Cyclic voltammetry (CV) studies were carried out using an electrochemical workstation instrument (WBCS3000, Wonatech, Korea). The potential range of 2.2–4.5 V *vs.* Li<sup>+</sup>/Li at 0.2 mV s<sup>-1</sup> scan rate was assigned for the measurements. The cycling of galvanostatic charge/discharge was achieved between 2.2 and 4.5 V *vs.* Li<sup>+</sup>/Li using various current densities of 100, 200, 400, 600, 800, and 1,000 mA g<sup>-1</sup>. The all specific capacities and current densities were calculated according to the active material weight (GdHCCo).

Ex situ characterizations were accomplished to investigate the intercalation of Li<sup>+</sup> ions and the mechanism of electrochemical Li-ion storage upon charge/discharge in the GdHCCo. Half-cells at diverse discharge (3.7, 3.1, 2.7, and 2.5 V *vs.* Li<sup>+</sup>/Li) and charge (3.0, 3.5, and 4.0 V *vs.* Li<sup>+</sup>/Li) states were disassembled, and the working electrodes were thoroughly rinsed in a glove box filled with Ar, vacuum-dried overnight, and subjected to ex-situ XRD, Raman spectroscopy, and FT-IR spectroscopy measurements.

#### **1.9.4. Results and discussion**

In the theoretical crystal structure of GdHCCo, cyanide ligands bridge Co<sup>3+</sup> and Gd<sup>3+</sup> ions (Figure 1.59a), and each unit cell comprises of eight

subunits, which can be occupied by  $\text{Li}^+$ . Microscopic imaging (Figures 1.59b,d) revealed that GdHCCo exhibits an orthorhombic structure and strip morphology with Co and Gd elements uniformly distributing throughout products. The XRD pattern of GdHCCo (Figure 1.59c) confirmed that this compound exhibits a  $Cmcm(63)$  orthorhombic crystal structure ( $a = 7.321 \text{ \AA}$ ,  $b = 12.758 \text{ \AA}$ ,  $c = 13.564 \text{ \AA}$ ). The distinctive change from the conventional cubic structure to an orthorhombic one was ascribed to the increase of interplanar spacing due to the increased ion radius of  $\text{Gd}^{3+}$  (93.8 pm).<sup>[37-39]</sup> The XRD patterns were experimentally studied and theoretically calculated exhibiting slight deviation on the intensity, as demonstrated by the ( $Y_{\text{obs}} - Y_{\text{calc}}$ ) line (Figure 1.59c). The background was corrected by pseudo-Voigt function. The allowed Bragg positions are marked as vertical lines. Furthermore, the bridging nature of cyanide ligands in GdHCCo was verified by the observation of a strong  $\text{C}\equiv\text{N}$  stretching vibration at  $2193 \text{ cm}^{-1}$  in the corresponding FT-IR spectrum (Figure 1.59e). The  $\text{C}\equiv\text{N}$  stretching peak was deconvoluted into two signals indicating the stretching of cyanide bond in  $\text{Co}^{3+}-\text{C}\equiv\text{N}$  and  $\text{Co}^{2+}-\text{C}\equiv\text{N}$  environments.<sup>[40-42]</sup> The Raman spectrum of GdHCCo (Figure 1.59f) featured twin peaks of the CN group at  $2165$  and  $2183 \text{ cm}^{-1}$  and was therefore quite different from those of PBAs containing fourth-row transition metal ions.<sup>[43,44]</sup> Coordination of transition metal ions (*e.g.*,  $\text{Co}^{3+}$  in GdHCCo) through the carbon of the cyanide ligand is known to strongly affect the  $\text{C}\equiv\text{N}$  stretching frequency,<sup>[45,46]</sup> *i.e.* this frequency increases with increasing charge of the carbon-bonded transition metal ion. Therefore, the sharp peak at  $2183$

$\text{cm}^{-1}$  (Figure 1.59f) was attributed to  $\text{Co}^{3+}$ -bonded cyanide, while the sideward twin peaks at  $2165 \text{ cm}^{-1}$  (Figure 1.59f) were ascribed to  $\text{Co}^{2+}$ -bonded cyanide. The presence of  $\text{Co}^{2+}$  was ascribed to the reduction of the unstable  $\text{Co}^{3+}$  by water during synthesis. Furthermore, the related FT-IR spectrum (Figure 1.59e) featured an O–H vibration band at  $3672 \text{ cm}^{-1}$ , which reflected the absorption of water from the ambient environment and the presence of coordinated and non-coordinated water molecules within the host framework. The presence of absorbed and coordinated water was confirmed by the initial weight loss in the TGA curve of GdHCCo, whereas sample decomposition started at  $\sim 100 \text{ }^\circ\text{C}$  as shown by the different slope fitted in the TGA curve and rapid decrease in the weight (Figure 1.60).<sup>[47-49]</sup> However, one should keep in mind that the observed thermal stability of GdHCCo makes it well suited for practical application as an electrode material at room temperature.

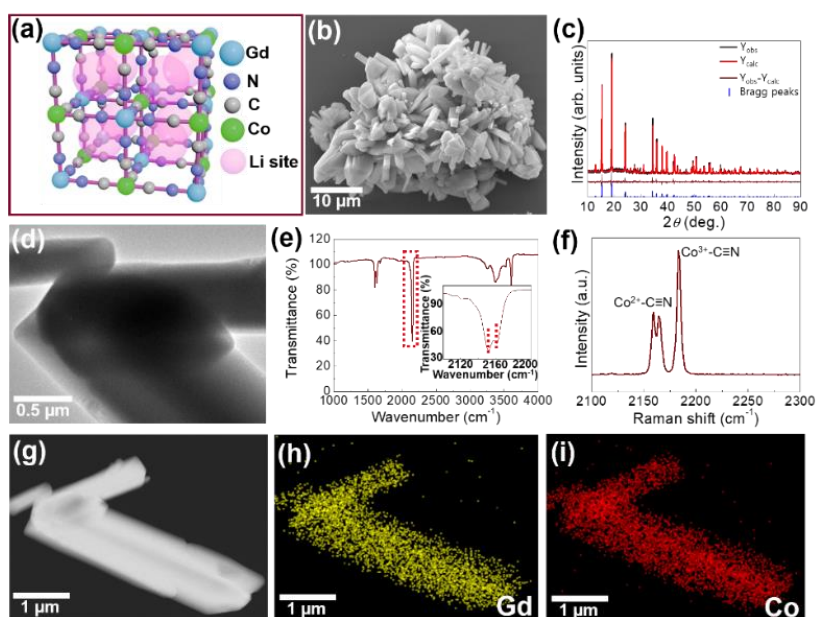


**Figure 1.59.** (a) Theoretical crystal structure of GdHCCo, with pink spheres representing cavities for Li-ion intercalation. (b) FE-SEM image of a GdHCCo particle revealing an orthorhombic crystal structure. (c) XRD pattern of GdHCCo, with standard peaks represented by red lines. (d) TEM image of GdHCCo. (e) FT-IR spectrum of GdHCCo, with the magnified  $\text{C}\equiv\text{N}$  stretching peak shown in the inset. The observed peak splitting demonstrates the co-existence of  $\text{Co}^{2+/3+}$ . (f) Raman spectrum of GdHCCo showing  $\text{Co}^{3+}\text{-CN}$  and  $\text{Co}^{2+}\text{-CN}$  peaks. (g–i) STEM image and representative elemental mapping images of a GdHCCo crystal.

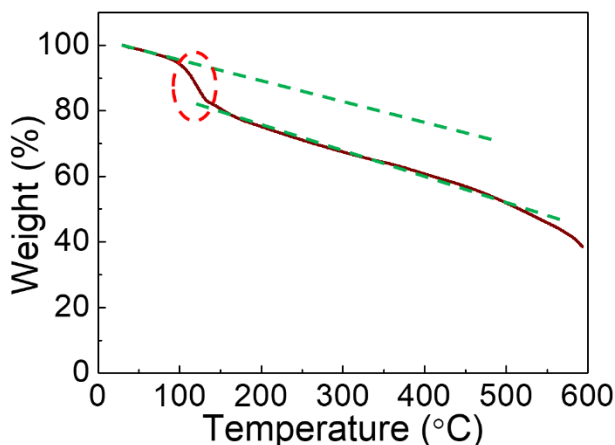


**Figure 1.60.** TGA curve of the as-prepared GdHCCo.

As expected, XPS (Figures 1.61) analysis of GdHCCo confirmed that the valence states of constituent elements (C, N, Co, and Gd) did not significantly change during synthesis, as it involved only a simple co-precipitation. Furthermore, peak deconvolution (Figure 1.61) was

performed for each element, and several satellite peaks were seen in the case of C (Figure 1.61a). The results of  $\text{Co}^{2+}$  signal deconvolution (Figure 1.61d) agreed with those obtained for  $\text{Co}^{2+}$  peaks in FT-IR and Raman spectra. Furthermore,  $\text{GdHCCo}$  was found to contain highly pure  $\text{Gd}^{3+}$  (Figure 1.61c). The larger ionic radius of  $\text{Gd}^{3+}$  may place the cyanide bond under tension and pressure, facilitating the adoption of an orthorhombic crystal structure. Nevertheless, further studies are needed to reveal the in-depth theory behind this behavior.

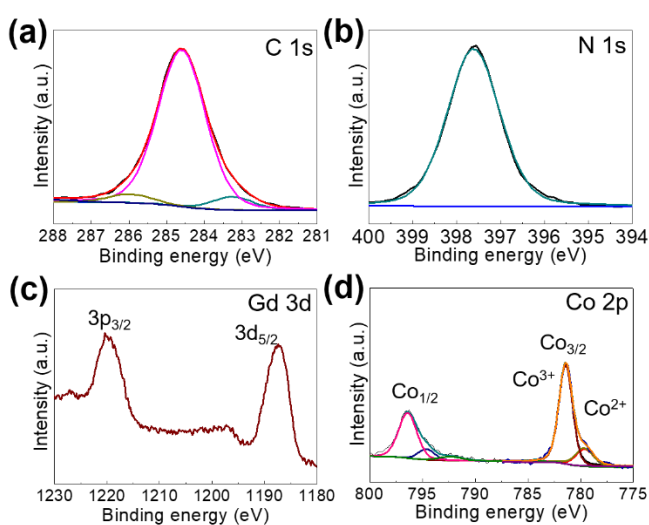


**Figure 1.61.** (a) C, (b) N, (c) Gd, and (d) Co XPS spectra of  $\text{GdHCCo}$ .

To obtain a relatively exact molecular formula of  $\text{GdHCCo}$ , this compound was characterized by XRF and the obtained results were in agreement with those of EDX and EDS. The molecular formula of  $\text{GdHCCo}$  was determined as  $\text{K}_{0.0006}\text{GdCo}(\text{CN})_6$ , and this compound was

therefore concluded to contain much less  $K^+$  impurities than other PBAs.<sup>[50,51]</sup>

The electrochemical properties of GdHCCo were probed by CV. The shape of the obtained CV curve (Figure 1.62a) indicated a primarily capacitive type of Li-ion storage, although two overlaid tiny peaks were observed at  $\sim 3.7$  V vs.  $Li^+/Li$ . Based on the obtained results, the potential window for the operation of GdHCCo as a cathode material was determined as 2.2–4.5 V vs.  $Li^+/Li$ . Even though the active potential window of graphite used for Li-ion storage is less than 1 V, a bare graphite paper current collector was inserted into the half-cell prior to capacity measurements to verify that the observed capacity originates from GdHCCo as the active material. As a result, the contribution of the naked graphite paper current collector to half-cell capacity was found to be negligibly small. The rate performance (Figure 1.62b) of GdHCCo as a half-cell cathode sustainably increased during the initial phase of cycling because of electrode material activation to form smooth channels for the transfer of  $Li^+$  and electrons.<sup>[52,53]</sup> Figure 1.62c presents the corresponding voltage profiles of charge/discharge at diverse specific currents, demonstrating that stable charge/discharge processes were observed in all cases.

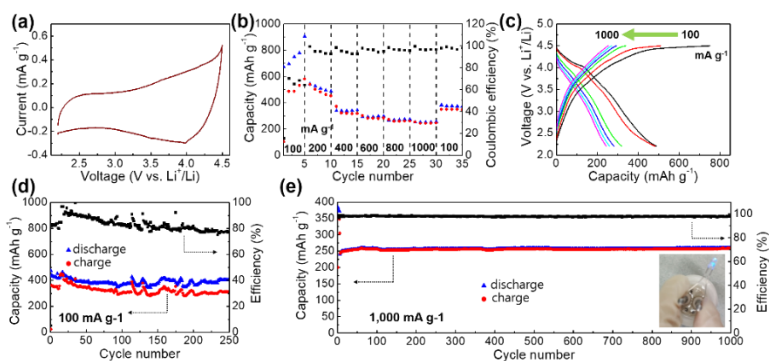


**Figure 1.62.** Electrochemical study of GdHCCo as a half-cell cathode. (a) CV curve, (b) rate performance, (c) charge/discharge curves at various current densities, (d) evolution of capacity upon repeated charge/discharge cycling at  $100 \text{ mA g}^{-1}$  for 250 cycles, (e) evolution of capacity upon repeated charge/discharge cycling at  $1,000 \text{ mA g}^{-1}$  for 1,000 cycles, inset shows the half-cell lighting a blue LED.

Cathode material stability largely determines the lifespan of the corresponding device. Therefore, we subjected two half-cells to long-term cycling tests, which were performed at  $100 \text{ mA g}^{-1}$  for 250 cycles (Figure 1.62d) and at  $1,000 \text{ mA g}^{-1}$  for 1,000 cycles (Figure 1.62e), observing good stability in both cases. Notably, the efficiency (77%) observed after 250 charge/discharge cycles at  $100 \text{ mA g}^{-1}$  increased to 98% when charge/discharge was conducted for 1,000 cycles at  $1,000 \text{ mA g}^{-1}$ . Figure 1.63 shows representative voltage profiles recorded during long-term cycling at  $1,000 \text{ mA g}^{-1}$ , revealing that these profiles did not exhibit distinct distortion and thus demonstrating successful and stable

charge/discharge. 352 and 258 mAh g<sup>-1</sup> capacities were acquired at the 10<sup>th</sup> charge/discharge cycle at 100 and 1,000 mA g<sup>-1</sup>, respectively, while values of 312 and 251 mAh g<sup>-1</sup> were obtained after 250 and 1,000 charge/discharge cycles, respectively, at both current densities. Based on the obtained data, average capacity losses of 0.05 and 0.003% per cycle were calculated for cycling at 100 and 1,000 mA g<sup>-1</sup>, respectively. The inset of Figure 1.62e shows that the assembled half-cell could light a 3-V LED lamp. After long-term cycling, the cathode material was probed for its crystal structure stability by using XRD analysis, and the characteristic (021), (022), (113), (223), and (115) peaks of GdHCCo were found to be well preserved, which indicated great stability of this material (Figure 1.64).

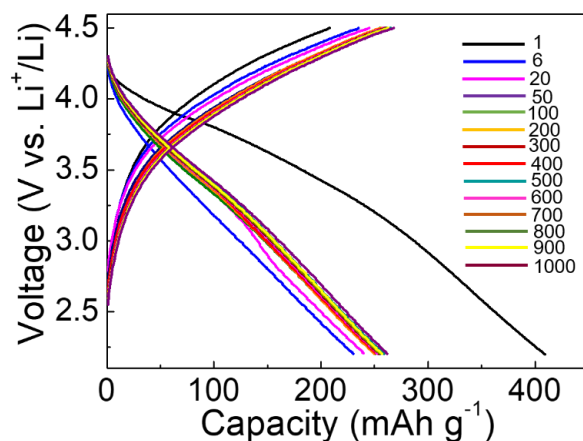


**Figure 1.63.** Representative charge/discharge voltage profiles of the GdHCCo cathode measured at 1,000 mA g<sup>-1</sup> for 1,000 cycles.

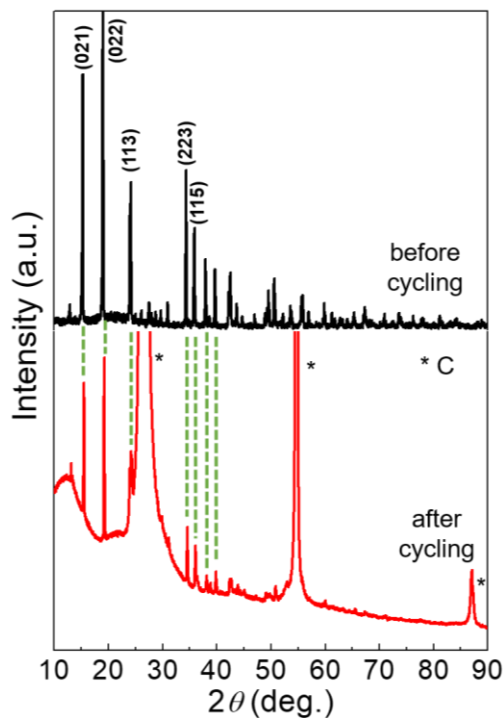


**Figure 1.64.** XRD patterns of GdHCCo recorded before and after long-term charge/discharge cycling at  $1,000 \text{ mA g}^{-1}$  for 1000 cycles.

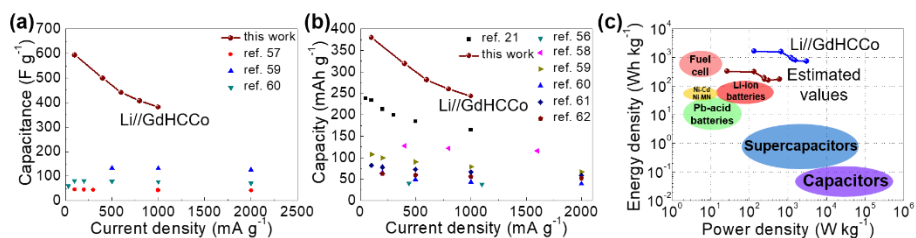


**Figure 1.65.** Dependence of (a) capacitance and (b) capacity on current density for GdHCCo and other cathode materials utilized in Li-ion capacitors. (c) Position of Li/GdHCCo and the estimated corresponding full cell on the energy density–power density map.

It is worth pointing out that the Farad-to-mAh conversion used in the present work is critical for the hybrid battery-capacitor system to remain similar to that conventional battery materials, rather than to materials employed for electric double layer capacitor (EDLC) or for Faradaic pseudo-capacitors.<sup>[54,55]</sup> In Figures 1.65a and b, GdHCCo is compared with other cathode materials recently reported for Li-ion capacitors (see References 56-62 in Figure 1.65). The comparison shows that the capacities/capacitances of GdHCCo at various current densities were almost twice higher than those observed for state-of-the-art cathode materials under identical conditions. It is also worth mentioning that the capacity of GdHCCo was one of the highest among those of PBAs materials. The calculated energy and power densities of the GdHCCo (normalized to single-electrode weight) showed that this material occupies a position between high-performance rechargeable batteries and supercapacitors (Figure 1.65c). Gravimetric energy and power densities at the full-cell level were estimated as 605 Wh kg<sup>-1</sup> and 174 W kg<sup>-1</sup>, respectively, by dividing the half-cell values by a factor of five.<sup>[63,64]</sup> However, as the use of a Li metal anode is not practical, further studies are needed for an in-depth full-cell evaluation of GdHCCo as a cathode material.

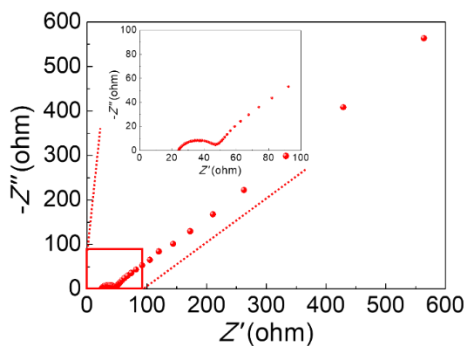


**Figure 1.66.** Electrochemical impedance spectrum of a fresh GdHCCo electrode in an assembled half-cell. Inset shows an expansion of the red-box-marked area.

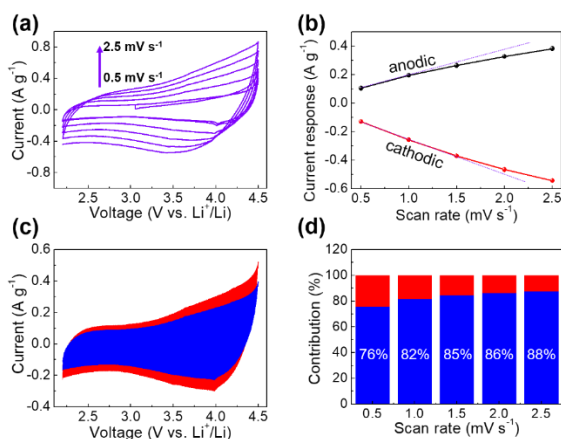


**Figure 1.67.** (a) CV curves of GdHCCo recorded at various scan rates (0.5–2.5 mV s<sup>-1</sup>). (b) Current response measured at 3.5 V vs. Li<sup>+</sup>/Li at various scan rates. (c) Surface (blue region) and diffusion (red region) process co-controlled regions of Li-ion storage obtained for a scan rate of 0.5 mV s<sup>-1</sup>. (d) Relative contributions of the above regions obtained at scan rates of 0.5, 1.0, 1.5, 2.0, and 2.5 mV s<sup>-1</sup>.

To reveal the possible reason of this high performance, the fresh electrode was subjected to EIS measurements (Figure 1.66). In the obtained plots, the depressed semicircle and the sloping line Reflected charge transfer impedance and Warburg impedance, respectively. Based on the semicircle intercept with the  $Z'$ -axis, charge transfer impedance was estimated to be as small as  $25 \Omega$ , which was assumed to be the key reason of superior electrochemical properties. In turn, structural comparison of GdHCCo with other PBAs revealed that this small impedance was related to the dependence of Li-ion diffusion on the framework structure. In contrast to other PBAs, GdHCCo has an orthorhombic crystal structure characterized by increased  $b$  and  $c$  lattice constants that exceed the basic value of  $10.5 \text{ \AA}$ .<sup>[65]</sup> Consequently, the presence of expanded Li-ion transfer channels inside GdHCCo results in increased charge transfer capability.

To qualitatively and quantitatively analyze the contributions of diffusion-controlled and capacitive Li-ion storage to the total Li-ion storage capacity of GdHCCo, we subjected the GdHCCo electrode to CV measurements at different scan rates ( $0.5\text{--}2.5 \text{ mV s}^{-1}$ ) within a constant potential window of  $2.2\text{--}4.5 \text{ V vs. Li}^+/\text{Li}$  (Figure 1.67a). The curves obtained at all scan rates displayed a typical EDLC-type rectangular shape, featuring overlaid humps and no obvious distortion. The response currents measured at  $3.5 \text{ V vs. Li}^+/\text{Li}$  in CV curves for the GdHCCo are represented in Figure 1.67b, which depicts the current dependence on the CV sweep rates. As the scan rates increase from  $0.5$  to  $2.5 \text{ mV s}^{-1}$ , the relationship between CV scan rates and response currents of the

GdHCCo electrode material gradually deviates from the linear manner suggesting the concomitant capacitive and diffusion-limited Li-ion storage. To further disclose this capacitive feature, the dependence of response current ( $i$ ) on scan rate ( $v$ ) was modeled by the power law (Eq. 1):

$$i = av^b \quad (1)$$

Herein, we are interested in the percentage of different capacity contributions at various CV sweep rates. The contribution ratio of the storage mechanisms can be obtained by deriving the Eq. (1) as:

$$i = k_1v + k_2v^{1/2} \quad (2)$$

where  $k_1v$  illustrates the capacitive storage, and  $k_2v^{1/2}$  represents the diffusion-limited contribution. The acquired results are shown in Figure 1.67c, which demonstrates that 76% of the total capacity is related to capacitive Li<sup>+</sup> storage at 0.5 mV s<sup>-1</sup>. This contribution was improved with increasing the scan rate (88% at 2.5 mV s<sup>-1</sup>) indicating that the capacitive storage could be dominant under these conditions and showed that GdHCCo is more suited for use in capacitors.

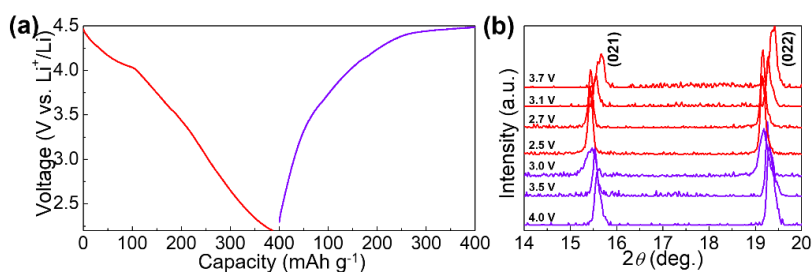


**Figure 1.68.** (a) Charge (purple) and discharge (red) potential curves used to prepare samples charged/discharged at different cutoff voltages.

(b) Ex-situ XRD patterns of the prepared samples showing characteristic (021) and (022) peaks.

To further disclose the origin of structural changes caused by  $\text{Li}^+$  intercalation/de-intercalation during the diffusion process, electrodes in diverse charge/discharge states were characterized by ex-situ XRD (Figure 1.68). The intercalation of  $\text{Li}^+$  into the GdHCCo framework upon discharge was indicated by the shift of characteristic (021) and (022) peaks to lower angles due to concomitant framework expansion. This process was reversed during charging, as Reflected by the shift of the above peaks in the opposite direction. Overall, these peaks were well preserved at each charge/discharge state, which was an indicator of highly reversible local stretching.

### **1.9.5. Conclusions**

In conclusion, we described an unprecedented synthesis of an orthorhombic Prussian blue analogue, namely GdHCCo, and demonstrated its high performance as a cathode material for Li-ion capacitors. High capacities of 352 and 258  $\text{mAh g}^{-1}$  were obtained at the 10<sup>th</sup> charge/discharge cycle at 100 and 1,000  $\text{mA g}^{-1}$ , respectively, while values of 312 and 251  $\text{mAh g}^{-1}$  were obtained after 250 and 1,000 charge/discharge cycles, respectively, at both current densities. The energy and power densities were estimated to be 605  $\text{Wh kg}^{-1}$  and 174

W kg<sup>-1</sup>, respectively. Both surface- and diffusion-controlled processes were found to contribute to Li-ion storage, and the contribution of the former increased from 76% at 0.5 mV s<sup>-1</sup> to 88% at 2.5 mV s<sup>-1</sup>. Finally, the highly reversible nature of Li-ion intercalation/deintercalation into/from GdHCCo was demonstrated by ex-situ instrumental characterizations.

### 1.9.6. References

- [1] Xu, Q. et al. *Adv. Energy Mater.* 2017, 7, 1601481.
- [2] Zhou, J. et al. *ACS Nano* 2015, 9, 3837.
- [3] Wang, J. et al. *Nat. Commun.* 2016, 7, 12032.
- [4] Larcher, D. et al. *Nat. Chem.* 2015, 7, 19.
- [5] Lu, Z. et al. *ACS Nano* 2015, 9, 2540.
- [6] Shang, H. et al. *Angew. Chem. Int. Edit.* 2018, 57, 774.
- [7] Tabassum, H. et al. *Adv. Mater.* 2018, 30, 1705441.
- [8] Wu, X. et al. *ACS Appl. Mater. Inter.* 2016, 8, 23706.
- [9] Ding, Y.-L. et al. *Nano Lett.* 2015, 15, 1388.
- [10] Song, H. et al. *J. Power Sources* 2016, 328, 599.
- [11] Wang, F. et al. *J. Mater. Chem. A* 2017, 5, 14922.
- [12] Tao, Y. et al. *Appl. Mater. Today* 2019, 15, 18.
- [13] Wang, H. et al. *Small* 2015, 11, 1470.
- [14] Zhang, S. S. *J. Power Sources* 2017, 343, 322.

- [15] Yang, M. et al. *Adv. Energy Mater.* 2015, 5, 1500550.
- [16] Wang, H. et al. *Adv. Mater.* 2017, 29, 1702093.
- [17] Wang, F. et al. *Small* 2016, 12, 6207.
- [18] Stoller, M. D. et al. *Phys. Chem. Chem. Phys.* 2012, 14, 3388.
- [19] Ma, Y. et al. *Adv. Mater.* 2015, 27, 5296.
- [20] Nie, P. et al. *J. Mater. Chem. A* 2014, 2, 5852.
- [21] Yu, S.-H. et al. *ECS Electrochem. Lett.* 2013, 2, A39.
- [22] Shokouhimehr, M. et al. *Nanosci. Nanotech. Lett.* 2013, 5, 770.
- [23] Yu, S.-H. et al. *RSC Adv.* 2014, 4, 37365.
- [24] Yu, S.-H. et al. *RSC Adv.* 2014, 4, 12087.
- [25] You, Y. et al. *Energy Environ. Sci.* 2014, 7, 1643.
- [26] Yue, Y. et al. *Angew. Chem. Int. Edit.* 2014, 53, 3134.
- [27] Wu, X. et al. *Nano Energy* 2015, 13, 117.
- [28] Zhang, C. et al. *Adv. Funct. Mater.* 2017, 27, 1604307.
- [29] Wessells, C. D. et al. *Nano Lett.* 2011, 11, 5421.
- [30] Wu, X. et al. *Electrochem. Commun.* 2017, 77, 54.
- [31] Reed, L. D. et al. *Chem. Commun.* 2015, 51, 14397.
- [32] Zhang, K. et al. *Electron. Mater. Lett.* 2019, 15, 444.
- [33] Han, L. et al. *Adv. Mater.* 2016, 28, 4601.
- [34] Zhang, K. et al. *J. Alloy Compd.* 2019, 791, 911.
- [35] Mizuno, Y. et al. *J. Mater. Chem. A* 2013, 1, 13055.
- [36] Islamoglu, T. et al. *Inorg. Chem.* 2018, 57, 13246.

- [37] Hu, M. et al. *Eur. J. Inorg. Chem.* 2012, 2012, 4795.
- [38] Zhou, L. et al. *Electrochim. Acta* 2017, 232, 106.
- [39] Okubo, M. et al. *Dalton T.* 2013, 42, 15881.
- [40] Wang, Q. et al. *Dalton T.* 2015, 44, 12878.
- [41] Lezna, R. O. et al. *J. Phys. Chem. B* 2002, 106, 3612.
- [42] Shimamoto, N. et al. *Inorg. Chem.* 2002, 41, 678.
- [43] Moretti, G. et al. *J. Raman Spectrosc.* 2018, 49, 1198.
- [44] Lukey, G. C. et al. *React. Funct. Polym.* 2000, 44, 121.
- [45] Huang, Y. et al. *Nano Energy* 2017, 39, 273.
- [46] Grandjean, F. et al. *Dalton T.* 2016, 45, 18018.
- [47] Prabakar, S. J. R. et al. *RSC Adv.* 2015, 5, 37545.
- [48] Zhang, H. et al. *CrystEngComm* 2017, 19, 2057.
- [49] Shokouhimehr, M. Kent State University, 2010.
- [50] Takahashi, A. et al. *Chem. Eng. Res. Des.* 2016, 109, 513.
- [51] Wessells, C. D. et al. *Nano Lett.* 2011, 11, 5421.
- [52] Omarova, M. et al. *Electrochim. Acta* 2015, 184, 58.
- [53] Mizuno, Y. et al. *J. Phys. Chem. C* 2013, 117, 10877.
- [54] Mazinani, B. et al. *JOM* 2019, 71, 1499.
- [55] Wang, Y. et al. *Chem. Soc. Rev.* 2016, 45, 5925.
- [56] Deng, B. et al. *Adv. Funct. Mater.* 2018, 28, 1704330.
- [57] Yu, X. et al. *Nano Energy* 2015, 15, 43.
- [58] Li, B. et al. *Adv. Energy Mater.* 2016, 6, 1600802.

- [59] Xia, Q. et al. *Adv. Energy Mater.* 2017, 7, 1701336.
- [60] Lee, W. S. V. et al. *Nano Energy* 2016, 27, 202.
- [61] Wang, H. et al. *Adv. Funct. Mater.* 2016, 26, 3082.
- [62] Li, S. et al. *Small* 2017, 13, 1602893.
- [63] Dudney, J. N. *Electrochem. Soc. Interf.* 2008, 17, 44.
- [64] Lee, S. W. et al. *Nat. Nanotechnol.* 2010, 5, 531.
- [65] Lee, H.-W. et al. *Nat. Commun.* 2014, 5, 5280.

## 2. Chapter 2

### 2.1. Introduction

#### 2.1.1. Reduciton of nitro-aromatics to amino-aromatics

Reduction process is a fundamental and important chemical transformation in organic synthesis <sup>[1-3]</sup> and industrial chemistry,<sup>[4-6]</sup> the key step being the electrons transform from a donor to the target substance. The reduction of nitroaromatics (NAs) is a common and facile route to produce aminoaromatics (AAs), which are very significant intermediates for the synthesis of several nitrogen-containing compounds, such as agrochemicals, pharmaceuticals, polymers, dyes, pesticides, and cosmetics.<sup>[7-12]</sup> Several toxic NAs are responsible for serious environmental pollutions.<sup>[13]</sup> However, they can be transformed into AAs, *e.g.* nitrophenols (NP) conversion into harmless aminophenols (AP), which are potential intermediates for accessing pharmaceutical and dyes via the reduction process (Figure 2.1a). Accordingly, various NAs can be reduced to their amino counterparts through the use of catalysts wherein applied catalysts play significant role.<sup>[14-19]</sup> Consequently, the suitable design of the catalyst structure and their prudent selection can remarkably improve the reduction efficiency thus providing better catalytic sustainability and recoverability.

The description of the catalysts these days can be simply and ideally stated as nanoparticles (NPs) with or without supports. Nano-sized catalysts with high specific surface area and without supports provide a

ready contact with the reactants, thereby improving the catalytic activity.<sup>[20–22]</sup> However, the high surface energy of nano-structures escalates their instability and leads to aggregation which results in the loss of catalytic activity.<sup>[23,24]</sup> An inevitable loss of nanocatalysts appears during their tedious separation from the products. Therefore, the deployment of supports effectively prevents their aggregation and undesirable loss, thereby enlarging the total surface area and assuring their sustained catalytic activity and reusability; the positioning of supports with a high specific surface area generally provide a promoted adhesion to reactants.<sup>[25–27]</sup>

Regarding the greener aspect of the catalytic processes, it is highly desirable to develop environmentally benign procedures which can be conducted preferably in aqueous media thus avoiding the use of volatile organic solvents; sodium borohydride ( $\text{NaBH}_4$ ) is one such favored water-soluble reductant for representative reductions.<sup>[28–30]</sup> In the reduction process of NA to AA with aqueous  $\text{NaBH}_4$ , electrons from  $\text{BH}_4^-$  transfer to NA when both of the species are absorbed on the surface of the catalyst.<sup>[31–33]</sup>

### 2.1.2. Characterizations

X-ray diffraction (XRD), scanning electron microscopy (SEM), field emission SEM (FESEM), transmission electron microscopy (TEM), X-ray photoelectron spectroscopy (XPS), and infrared radiation (IR), *etc.* are the most commonly used characterization techniques for the synthesized catalysts while ultraviolet visible spectroscopy (UV-Vis) is a convenient way for monitoring the conversion process; 4-NP has a typical absorption peak at 317 nm. However, after adding aqueous NaBH<sub>4</sub>, a red shift of the maximum absorption peak occurs immediately from 317 nm to 400 nm due to the formation of 4-nitrophenolate ions under alkaline conditions. Thereafter, these peaks at 400 nm are reduced over time.<sup>[34–38]</sup> Moreover, the gas chromatography-mass spectrometer is needed for the measurement of accurate conversion-percentage and for verifying the ensuing reaction products.<sup>[39,40]</sup>

### 2.1.3. Classification of nanocatalysts

Consequently, the compatibility of the applied catalysts effects the overall reduction productivity.<sup>[41]</sup> In view of their importance, we present recent methods for the synthesis of nanocatalysts as directed for the reduction of NAs with focus on the advances in nano-structured catalysts for the hydrogenation of NA with aqueous NaBH<sub>4</sub>. The general strategies for the synthesis of representative heterogeneous nanocatalysts, their advantages, limitation, and challenges are also discussed. For the sake of differentiation and ease of understanding, the nanocatalysts are classified with or without supports for mono-metal and bi- or multi-metal nano-structured catalysts. Additionally, we have categorized separately the supported nanocatalysts with and without magnetic properties in view of their ease of separation and reuse (Figure 2.1b). The first category of nanocatalysts in this article, mono-metallic nanocatalysts, possess solely one metal element as the catalyst for expediting the reduction of NAs to AAs. Subsequently, bi-metallic and solid supported non-magnetic nanocatalysts are discussed, emphasizing their designs to overcome the low efficiency and aggregation issues of the mono-metal nanocatalysts.<sup>[42]</sup> Although these catalysts demonstrate considerable improved catalytic activity, their reusability stays challengeable. Consequently, the magnetic nanostructured catalysts are presented as comfortably separable and sustainable catalysts for reduction of NAs.<sup>[43]</sup>

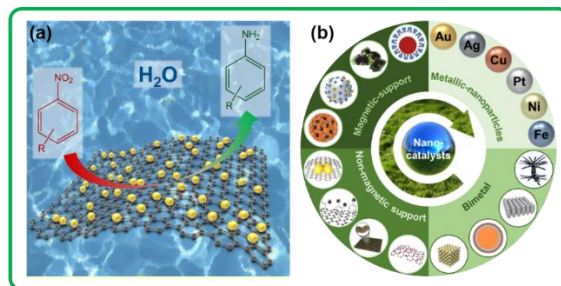


**Figure 2.1.** (a) Schematic design for the reduction of nitrobenzene with aqueous NaBH<sub>4</sub> using nanocatalysts. (b) The classification of various nanocatalysts applied for the reduction of NAs to AAs.

#### 2.1.4. References

- [1] Varma, R. S. *Green Chem.* 2014, 16, 2027.
- [2] Goswami, A. et al. *ACS Appl. Mater. Inter.* 2017, 9, 2815.
- [3] Shokouhimehr, M. et al. *Chem. Commun.* 2013, 49, 4779.
- [4] Datta, K. J. et al. *ChemCatChem* 2016, 8, 2351.
- [5] Kabalka, G. W. et al. *Tetrahedron* 1990, 46, 7443.
- [6] Shokouhimehr, M. et al. *Appl. Catal. A-Gen.* 2014, 476, 133.
- [7] Blaser, H. U. et al. *Adv. Synth. Catal.* 2003, 345, 103.
- [8] Ayad, M. M. et al. *Mol. Catal.* 2005, 439, 72.
- [9] Datta, K. J. et al. *Sci. Rep.* 2017, 7, 11585.
- [10] Rathi, A. K. et al. *Catal. Sci. Technol.* 2016, 6, 152.
- [11] Vass, A. et al. *Tetrahedron Lett.* 2001, 42, 5347.
- [12] Qin, G. W. et al. *J. Phys. Chem. C* 2010, 114, 6909.
- [13] He, S. et al. *ChemistrySelect* 2016, 1, 2821.

- [14] Mahmoud, M. A. et al. *J. Am. Chem. Soc.* 2008, 130, 4590.
- [15] Zhang, J. et al. *Appl. Catal. B* 2013, 132-133, 107.
- [16] Narayanan, R. et al. *Nano Lett.* 2004, 4, 1343.
- [17] Gelder, E. A. et al. *Chem. Commun.* 2005, 4, 522.
- [18] Shokouhimehr, M. *Catalysts* 2015, 5, 534.
- [19] Ansar, S. M. et al. *ACS Catal.* 2016, 6, 5553.
- [20] Zeng, H. C. *Acc. Chem. Res.* 2013, 46, 226.
- [21] Shokouhimehr, M. et al. *Synlett.* 2006, 4, 618.
- [22] Shokouhimehr, M. et al. *J. Mater. Chem. A* 2014, 2, 7593.
- [23] Murray, C. B. et al. *Rev. Mater. Sci.* 2000, 30, 545.
- [24] Astruc, D. et al. *Chem. Int. Ed.* 2005, 44, 7852.
- [25] Choi, K. H. et al. *Bull. Korean Chem. Soc.* 2013, 34, 1195.
- [26] Han, C. et al. *Adv. Funct. Mater.* 2015, 25, 221.
- [27] Shokouhimehr, M. et al. *Res. Chem. Intermed.* 2018, 44, 1617.
- [28] Herves, P. et al. *Chem. Soc. Rev.* 2012, 41, 5577.
- [29] Ghosh, S. K. et al. *Appl. Catal. A-Gen.* 2004, 268, 61.
- [30] Hailes, H. C. *Org. Process Res. Dev.* 2007, 11, 114.
- [31] Tang, S. C. et al. *J. Mater. Chem.* 2010, 20, 5436.
- [32] Lu, Y. et al. *ACS Nano* 2010, 4, 7078.
- [33] Layek, K. et al. *Green Chem.* 2012, 14, 3164.
- [34] Liu, X. et al. *Appl. Surf. Sci.* 2014, 292, 695.
- [35] Rathore, P. S. et al. *Catal. Sci. Technol.* 2015, 5, 286.
- [36] Farooqi, Z. H. et al. *Russ. J. Phys. Chem. A* 2016, 90, 2600.
- [37] Yanhe, H. et al. *J. Hazard. Mater.* 2018, 365, 448.
- [38] Saikia, H. et al. *ChemistrySelect* 2017, 2, 10524.

- [39] Richard, W. et al. *Electrochim. Acta* 2018, 283, 1640.
- [40] Iwase, K. et al. *Chem. Lett.* 2017, 47, 304.
- [41] Zhang, N. et al. *Chem. Mater.* 2013, 25, 1979.
- [42] Shah, M. et al. *Catal. Commun.* 2015, 65, 85.
- [43] Shang, L. et al. *Angew. Chem.* 2014, 126, 254.

## **2.2. Facile synthesis of monodispersed Pd nanocatalysts decorated on graphene oxide for reduction of nitroaromatics in aqueous solution**

### **2.2.1. Introduction**

Aromatic amines as essential raw materials for the production of pharmaceuticals, textile dyes, pigments, plastics, and pesticides play a significant role in chemical related industries.<sup>[1–4]</sup> Hydrogenation of the relatively toxic nitroaromatics to the eco–friendly aminoaromatics is a promising green approach producing high product yields with convenient operability. The current practical methods generally require hydrogen gas pressure and high temperature, which highly increase the cost of aminoaromatics production.<sup>[5–7]</sup> In addition, these processes are achieved predominantly by using toxic reductants *e.g.* hydrazine, and organic solvents, which are not environmentally compatible.<sup>[8]</sup> Nowadays, the researchers are focusing on the exploration of nanocatalysts with high catalytic activity, good sustainability, and environmental friendly characteristics.<sup>[9–11]</sup> Thus, diverse nanocatalysts have been synthesized using a series of transition metals such as Pt, Ru, and Rh, by wet chemical and high temperature synthesis.<sup>[12–15]</sup> However, the development of effective, nontoxic, and handle–convenient procedure to produce active nanocatalysts for this transformation is still highly desirable.<sup>[16]</sup>

Considering the eco–friendly concept, the exploration for the

reduction of nitroaromatics in a green approach with a high efficiency is still arduous.<sup>[17]</sup> Although several innovative methods have been introduced to circumvent these issues, the environmental-friendly conversion of nitroaromatics to aminoaromatics is still very challenging.<sup>[18]</sup> The utilization of catalysts is very necessary for this conversion process, which can be simply classified as metal particle catalysts,<sup>[19]</sup> bimetal catalysts,<sup>[20]</sup> solid-supported catalysts,<sup>[21]</sup> and magnetic supported catalysts.<sup>[22]</sup> However, many of these catalysts are prepared via complicated approaches hampering their proficiency and practicability.<sup>[23]</sup>

Atomic layer graphene simply fabricated by using the scotch tape in 2004<sup>[24]</sup> has been highlighted due to the good thermal conductive ( $5,000 \text{ W mK}^{-1}$ ), stable benzene ring structures, outstanding mobility of charge carrier ( $200,000 \text{ cm}^2 \text{ Vs}^{-1}$ ), exhibition of high theoretical specific surface area ( $2600 \text{ m}^2 \text{ g}^{-1}$ ), and feasible large-scale production.<sup>[25]</sup> Graphene is a desirable support material for stabilizing catalytic nanoparticles (NPs) such as Au, Pd, and Pt to synthesis supported nanocatalysts with high activity, durability, and reusability. Such heterogeneous catalysts have been applied for variable organic transformations.<sup>[26–28]</sup> However, synthesis of uniform and well-dispersed Pd NPs on graphene oxide (Pd/GO) for the reduction of nitroaromatics to aminoaromatics by green and simple technique has been confined.

To pursue a facile method for the synthesis of supported nanocatalysts, we prepared the heterogeneous Pd/GO nanocatalyst by the stabilization of the Pd NPs on the surface of GO using Pluronic F127, which is a mild

reductant and surfactant, and a water solvable copolymer. Then, we verified the prepared catalyst efficiency on catalytic activity, recyclability, and selectivity by reducing the nitroaromatics to aminoaromatics with aqueous sodium borohydride ( $\text{NaBH}_4$ ) solution. The nitroaromatics were totally converted to aminoaromatics in 10 min using very small amount of Pd NPs. The hybrid heterogeneous nanocatalyst showed 83% of conversion rate after 6 cycles reuse in the reduction of nitrobenzene to aminobenzene. Furthermore, various nitroaromatics possessing different functional groups were selectively reduced into their corresponding aminoaromatics in 10 min, exclusively.

### **2.2.2. Nanocatalyst preparation**

#### **Preparation of graphene oxide**

Graphene oxide was synthesized from graphite using the modified hummer's approach.<sup>[29]</sup> In a typical synthesis, commercial graphite powder (10 g) was added into 230 mL concentrated  $\text{H}_2\text{SO}_4$  that had been cooled to below of 20 °C with a circulator. 300 g potassium permanganate was added while stirring. Then, the temperature of the reaction was adjusted to 40 °C and the mixture was stirred for 1 h. Water (500 mL) was added to the mixture and the temperature was increased to 100 °C. After that, 2.5 mL  $\text{H}_2\text{O}_2$  (30 wt.%) was slowly added to the mixture. For purification, the suspension was washed with HCl solution (200 mL) using a filter and a funnel. The suspension was washed with water several times until the filtrate became neutral.

### **Preparation of Pd/GO nanocatalyst**

Pd/GO nanocatalyst was simply synthesized via a mixing process at room temperature. In a typical synthesis, 30 mL of GO solution (5 mg mL<sup>-1</sup>) was added in a beaker and stirred at room temperature, followed by the introduction of Pluronic F-127 aqueous solution (2 g). Finally, K<sub>2</sub>PdCl<sub>4</sub> (100 mg) was added in the above solution and stirred for 10 hours at room temperature to produce Pd NPs supported on the GO. The suspension was filtered and thoroughly washed with hot water and ethanol. The prepared heterogeneous catalyst was finally redispersed in water. The total concentration of the prepared Pd/GO solution was 30 mg mL<sup>-1</sup>.

#### **2.2.3. Catalytic characterization**

The reduction of nitrophenol to aminophenol with NaBH<sub>4</sub> was catalyzed using Pd/GO nanostructured catalyst at room temperature. This reaction was thoroughly achieved within 10 min. The hydrogenation process from nitrophenol to aminophenol was monitored by measuring the UV-vis absorption spectra of the reactants and products. Similarly, the reduction of other nitroaromatics was performed in water at room temperature. In a typical procedure, the Pd/Go nanocatalyst (20 μL) was dispersed in 15 mL H<sub>2</sub>O. Then, a nitroaromatic (1 mmol), NaBH<sub>4</sub> (1.2 mmol) and a small stirring bar were added into a

glass flask. The reaction mixture was stirred at room temperature for 10 min under air atmosphere. After completion of reaction, the Pd/GO nanostructured catalyst was separated using a centrifuge. The yields of the reduced products were determined by a GC–MS.

#### **2.2.4. Material characterization**

Water was deionized by a Nano Pure System (Barnsted). The organic reagents and F127 used in this work were purchased at the highest possible grade from Samchun Co., Ltd. and Daejung Co., Ltd. Potassium tetrachloropalladate ( $K_2PdCl_4$ ) and  $NaBH_4$  were purchased from SigmaAldrich. X–ray photoelectron spectroscopy (XPS) was performed using an Al  $K\alpha$  source (Sigma probe, VG Scientifics). The nanostructure of the prepared Pd/GO was studied using a high resolution X–ray diffraction (XRD, D8–Advance), a transmission electron microscope (TEM, JEOL JEM–3010) equipped with an energy–dispersive X–ray spectroscopy (EDX) detector, a scanning TEM (STEM, JEOL JEM–2100F), a thermal gravimetric analysis (TGA, simultaneous DTA/TGA analyzer), and an infrared radiation (IR, Nicolet iS50). The loading amount of Pd NPs on the graphene was measured through an inductively coupled plasma atomic emission spectroscopy (ICP–AES, ICPS–8100). The ICP samples were prepared by dissolving the dried Pd/GO samples in a 4 mL of *aqua regia* solution. Ultraviolet–visible (UV–vis) absorption spectra (V–770 JASCO) and gas chromatography–mass spectrometry (GC–MS, Agilent 7890A Gas chromatograph and 5977A

Mass selective detector) were employed to monitor the reduction processes and the conversion rate of the nitroaromatics to aminoaromatics, respectively.

### **2.2.5. Results and discussion**

The overall synthetic procedure is illustrated in Figure 1.2. Pd NPs were simply inlaid on the surface of the GO sheets to produce highly catalytic active heterogeneous Pd/GO nanostructured catalyst. The small Pd NPs (~5 nm) could be decorated on the surface of GO uniformly and discretely, which enhance their exposed active sites and specific surface area of Pd/GO nanocatalyst. TEM images (Figure 2.3b,c) also confirmed a similar result of uniform Pd NPs decorated on GO. The density of Pd NPs distribution is about  $510 \mu\text{m}^{-1}$ . The presence of Pd NPs on GO support does not show any detachable damage and we can clearly see the existence of ripples in GO sheets. In addition, the HRTEM image (Figure 2.4d) shows fine crystalline Pd NPs with ~5 nm of diameter. The small-size Pd NPs on the GO surface significantly contribute to widen the specific surface area to enhance the contact with nitroaromatics in the reduction process. TEM images also shows the similar results so that Pd NPs uniformly are loaded on the GO. The EDX spectrum distinctly confirms the existence of carbon and Pd species in Pd/GO.



**Figure 2.2.** Procedure for the synthesis of Pd/GO nanocatalyst.

We employed XRD characterizations in order to further study the crystal structure of both GO and Pd/GO catalyst. The XRD result of GO shows a peak at  $10.90^\circ$  indicating a disorder stack of the GO layers (Figure 2.4). However, the appearance of major peaks at  $2\theta = 40.02^\circ$ ,  $46.59^\circ$ ,  $68.08^\circ$ ,  $82.90^\circ$  in XRD patterns of the Pd/GO corresponding to (111), (200), (220), (311) (JCPDS 01–087–0641) clearly demonstrates the successful decoration of Pd NPs loading on GO. The surface stabilities of the GO and Pd/GO were confirmed by the FT–IR (Figure 2.5). A strong absorption band at  $3450\text{ cm}^{-1}$  (O–H stretching vibrations) in the case of GO indicates a heavy residual of  $\text{H}_2\text{O}$  than Pd/GO even after sufficient drying. In addition, the characteristic absorption bands are at  $1725\text{ cm}^{-1}$  for the C=O stretching vibrations,  $1600\text{ cm}^{-1}$  for the C=C (skeletal vibrations of graphene) in GO. However, those two peaks decreased in Pd/GO denoting the reduction of F127. The differences in FT–IR demonstrate the changes in the structures after Pd loading, which is also captured in the TGA analysis for both GO and Pd/GO (Figure 2.6). The weight loss ( $\sim 16\%$ ) in the GO is due to the loss of intercalated water molecules, followed by the second rapid drop corresponding to the

decomposition of functional groups at around 200 °C. Whereas, the weight loss of ~5% for Pd/GO suggests the presence of a little moisture in the prepared nanostructured catalyst. It demonstrates that the moisture and labile oxygen functional groups were removed after the introduction of the mild F127. An abrupt increase in the weight loss at ~400 °C for the Pd/GO can be ascribed by the remove of F127. We assumed the mechanism of the loading Pd NPs on the GO is due to the reduction effect of F127 with OH functional groups, which is the reducing agent for the Pd ions. After this process, the OH functional groups were transferred into carbonyl groups.

The XPS analysis for the Pd/GO nanocatalyst is shown in Figure 2.7. The XPS spectrum demonstrates the surface composition of the Pd/GO nanocatalyst, and the existence of Pd NPs on the GO. It also indicates a significant reduction of the oxygen functional groups as the consequence of the reduction process with Pluronic F127. The Pd ions in the solution interacted with the oxygen functional groups of the GO due to the electrophilic property of Pd generating Pd-O linkage, which facilitate the anchoring of Pd on the surface of GO. In addition, the existing functional defect sites on the GO can reduce the mobility of Pd ions, which further avoids the aggregation and facilitate the retaining of Pd NPs.

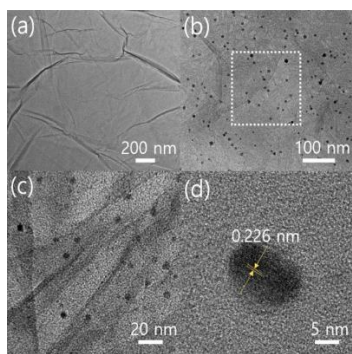


**Figure 2.3.** TEM images of (a) GO, and (b) and (c) Pd/GO nanocatalyst. (d) HRTEM image of Pd/GO nanocatalyst.

The catalytic reduction of the nitrophenol with  $\text{NaBH}_4$  by Pd/GO was chosen as a model reaction for the evaluation of catalytic activity. Figure 2.8 shows the UV–vis absorption spectra emerging the change in concentration of the nitrophenol. The original adsorption peak of nitrophenol at 317 nm red shifted to 400 nm after the addition of  $\text{NaBH}_4$  solution accompanied with the color change from green yellow to bright yellow (Figure 2.8, insets), which is due to the formation of nitrophenolate ions.  $\text{NaBH}_4$  appears alkaline in aqueous, therefore, the  $\text{H}^+$  from the hydroxyl of nitrophenol will be captured within a short time, causing the formation of nitrophenolate.<sup>[30–33]</sup> After the injection of Pd/GO, the peak intensities at 400 nm suddenly decreased due to the conversion and an absorption peaks of aminophenol shown at 300 nm.<sup>[34]</sup> The complete reduction of nitrophenol to aminophenol took ~10 min. This process was fulfilled very fast considering using very small amount of Pd NPs in water. This excellent catalytic activity can be explained by

two main reasons. First, the nano-sized Pd particles anchored on graphene without obvious aggregation enabled active sites sufficiently exposed in the ambient, which provided enough electron transfer channels during the hydrogenation. Second, the employment of the nanocatalysts in the reduction processes reduced the barrier energy, and a decreased barrier energy was provided by a small-sized Pd nanocatalysts, which affords a rapid electron transfer rate.<sup>[35–39]</sup> The reduction process of nitrophenol with NaBH<sub>4</sub> in this study can be explained according to the previously proposed mechanism.<sup>[40,41]</sup>

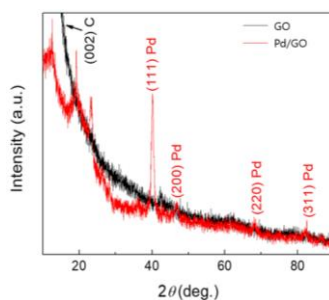


**Figure 2.4.** XRD patterns of GO and Pd/GO nanocatalyst.

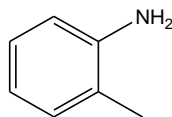
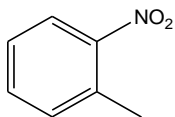
We also investigated the reductive activity of Pd/GO nanocatalyst for the nitroaromatics with various substituents as shown in table 1.1. Pd/GO nanocatalyst presented a high catalytic activity for the reduction of diverse functionalized nitroaromatic compounds in 10 min. The high hydrogenation activity of the Pd/GO nanocatalyst can be ascribed due to the  $\pi$  bond between the nitroaromatics and graphene oxide and the reactants accumulation on the surface of the supported Pd NPs,

promoting the contact of reactants and the nanocatalysts.<sup>[42]</sup>

**Table 2.1.** Heterogeneous reduction of nitroaromatics by Pd/GO nanocatalyst.



Entry	Substrate	Product	Yield (%)
1			99
2			99
3			97
4			94
5			99
6			85



Reaction conditions: substituted nitroarenes (1 mmol), NaBH<sub>4</sub> (1.2 mmol), Pd/GO nanocatalyst (20 μL), H<sub>2</sub>O (15 mL), room temperature, 10 min. The yields were determined by GC–MS.

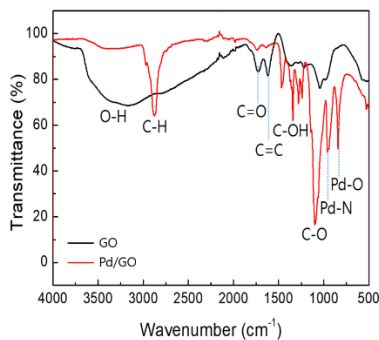


**Figure 2.5.** FT–IR spectra of GO and Pd/GO nanocatalyst.

When we compared the catalytic activity of the Pd/GO nanocatalyst with the previously published nanocatalysts in the reduction of nitrophenol, a very competitive yield of aminophenol was obtained (Table 2.2). The Pd/GO nanocatalyst also presented higher catalytic activity than the commercially available Pd/C catalyst. The commercial catalyst provided a much lower yield (39%) when it was used in the reduction of nitrobenzene with NaBH<sub>4</sub> under the identical reaction conditions.

**Table 2.2.** Catalytic comparison studies of known heterogeneous catalysts in the reduction of nitrophenol using NaBH<sub>4</sub>.



Entry	Catalyst	Amount (mg)	Time (min)	Refs.
1	Ni@Pd/KCC-1	0.4	5	[44]
2	Pd@black tea	2	1.3	[45]
3	Pd loaded TiO <sub>2</sub> nanotube	1	7	[46]
4	Aluminum hydroxide supported Pd NPs	25	6	[47]
5	CeO <sub>2</sub> /Pd	10	1	[48]
6	Pd/GO	5	10	[this work]

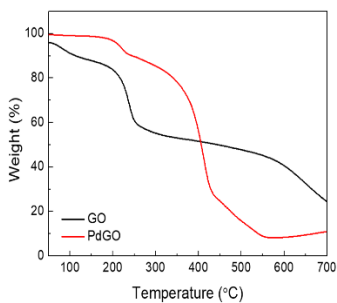


**Figure 2.6.** TGA results of GO and Pd/GO nanocatalyst.

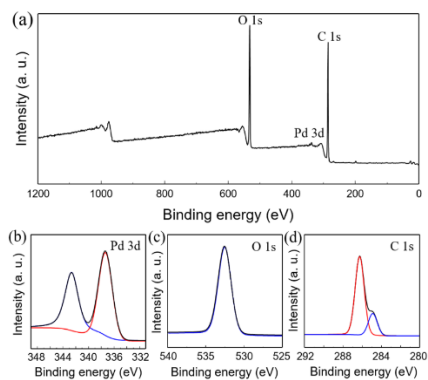


**Figure 2.7.** XPS analysis of (a) survey scan, and (b) Pd 3d, (c) C 1s, and (d) O 1s for the Pd/GO nanocatalyst.

Recycling and reusing the precious nanocatalysts are very important criteria for their practical applications.<sup>[43]</sup> The reusability of the Pd/GO nanocatalyst was conducted for the reduction of nitrobenzene. We repeated the same reduction process for 6 runs. The Pd/GO nanocatalyst were collected using a centrifuge and washed with deionized water for several times. Subsequently, the Pd/GO nanocatalyst was dried in an oven and applied for the next catalytic processes. The yields showed a gradually decrease in conversion rate so that 83% of conversion ratio was observed after six run (Figure 2.9). The centrifugation assisted to achieve an almost thoroughly separation of Pd/GO nanocatalyst from the aqueous, by which resulting in the loss of Pd/GO nanocatalyst due to the adhesion on the centrifuge tube. This inevitable loss reduced the conversion of nitroaromatics to aminoaromatics.

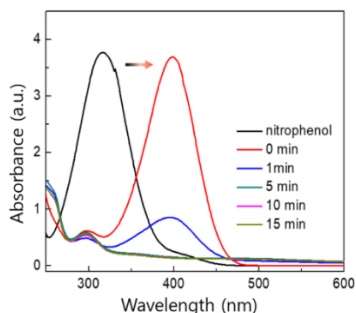


**Figure 2.8.** UV–visible spectra of the catalytic reduction using Pd/GO nanocatalysts. Nitrophenol (1 mmol) was reduced in the presence of NaBH<sub>4</sub> (1.2 mmol) by Pd/GO nanocatalyst (20 μL) in water.

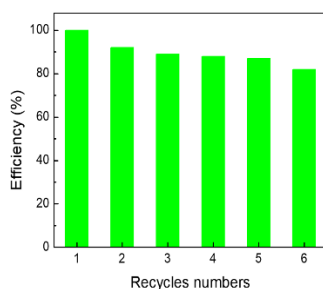


**Figure 2.9.** The conversion of nitrobenzene to aminobenzene. Nitrobenzene (1 mmol) was reduced in the presence of NaBH<sub>4</sub> (1.2 mmol) by Pd/GO nanocatalyst (20 μL) in 10 min.

### 2.2.6. Conclusions

In this study, we prepared the graphene oxide supported Pd nanoparticles (Pd/GO nanocatalyst) by employing the cost–efficient Pluronic F127 via a simple and green one–step preparation. A remarkable high catalytic activity was shown for the selective reduction of nitroaromatics to aminoaromatics. Of particular note of this procedure

is that the Pd/GO nanocatalyst could be reused for six consecutive cycles in the reduction of nitrobenzene. The excellent catalytic activity of Pd/GO nanocatalyst for the nitroaromatic reductions can be ascribed to the uniform dispersion and high surface area/volume ratio of Pd nanoparticles on GO. This work provided a modifying concept for hydrogenation of nitroaromatics that may stimulate further exploration of nanocatalysts with low-cost and high-efficiency for nitroaromatics reduction.

### 2.2.7. References

- [1] Blaser, H. U. et al. *Adv. Synth. Catal.* 2003, 345, 103.
- [2] Verho, O. *et al. ChemCatChem* 2014, 6, 3153.
- [3] Rahaim, R. J. et al. *Org. Lett.* 2005, 7, 5087.
- [4] Westerhaus, F. A. et al. *Nat. Chem.* 2013, 5, 527.
- [5] Shokouhimehr, M. et al. *Appl. Catal. A.* 2014, 476, 133.
- [6] Shokouhimehr, M. et al. *Chem. Commun.* 2013, 49, 4779.
- [7] Dong, Z. et al. *J. Mater. Chem. A* 2014, 2, 18775.
- [8] Dong, Z. et al. *Appl. Catal. B-Environ.* 2014, 158, 129.
- [9] Zaera, F. *Chem. Soc. Rev.* 2013, 42, 2746.
- [10] Shokouhimehr, M. *Catalysts* 2015, 5, 534.
- [11] Kim, A. et al. *Energy Environ. Focus* 2015, 4, 18.
- [12] Cui, X. et al. *Green Chem.* 2018, 20, 1121.

- [13] Sharma, S. et al. *Adv. Synth. Catal.* 2018, 360, 2131.
- [14] Yilmaz, E. et al. *J. Iran Chem. Soc.* 2017, 14, 2503.
- [15] Zhang, P. et al. *Catal. Commun.* 2017, 100, 214.
- [16] Yilmaz, E. et al. *J. Iran. Chem. Soc.* 2018, 15, 1721.
- [17] Tafesh, A. M. et al. *Chem. Rev.* 1996, 96, 2035.
- [18] Wu, H. et al. *Appl. Catal. A* 2009, 366, 44.
- [19] Datta, K. J. et al. *Sci. Rep.* 2017, 7, 11585.
- [20] Li, H. et al. *J. Mater. Chem.* 2010, 20, 4366.
- [21] Shokouhimehr, M. et al. *Synlett.* 2006, 4, 618.
- [22] Shokouhimehr, M. et al. *J. Mater. Chem. A* 2014, 2, 7593.
- [23] Gawande, M. B. et al. *Chem. Soc. Rev.* 2013, 42, 3371.
- [24] Allen, M. J. et al. *Chem. Rev.* 2009, 110, 132.
- [25] Geim, A. K. *Science* 2009, 324, 1530.
- [26] Moussa, S. et al. *ACS Catal.* 2012, 2, 145.
- [27] Siamaki, A. R. et al. *J. Catal.* 2011, 279, 1.
- [28] Gomez–Martinez, M. et al. *J. Mol. Catal. A Chem.* 2015, 404, 1–7.
- [29] Hummers, W. S. et al. *J. Am. Chem. Soc.* 1958, 80, 1339.
- [30] Anna, M. M. D. et al. *J. Mol. Catal. A Chem.* 2014, 395, 307.
- [31] Krogul–Sobczak, A. et al. *Catal. Commun.* 2018, 104, 86.
- [32] Kotha, S. S. et al. *Tetrahedron Lett.* 2016, 57, 1410.
- [33] Hu, Q. et al. *RSC Adv.* 2017, 7, 7964.

- [34] Ayad, M. M. et al. *Mol. Catal.* 2017, 439, 72.
- [35] Wang, W. et al. *Catalysts* 2018, 8, 60.
- [36] Menumenov, E. et al. *Nano Lett.* 2016, 16, 7791.
- [37] Wu, Z. et al. *Sci. Rep.* 2016, 6, 25638.
- [38] Shokouhimehr, M. et al. *Res. Chem. Intermed.* 2018, 44, 1617.
- [39] Haghightatzadeh, A. et al. *Desalin. Water Treat.* 2018, 92, 145.
- [40] Du, Y. et al. *Appl. Catal. A Gen.* 2004, 277, 259.
- [41] Huang, J. et al. *Angew. Chem. Int. Ed.* 2004, 43, 1397.
- [42] Kuwano, R. et al. *Org. Lett.* 2006, 8, 2653.
- [43] Shokouhimehr, M. et al. *Green Chem.* 2018, 20, 3809.
- [44] Dong, Z. et al. *Apply. Catal. B Environ.* 2015, 162, 372.
- [45] Lebaschi, S. et al. *J. Colloid Inter. Sci.* 2017, 485, 223.
- [46] Kalarivalappil, V. et al. *Catal. Lett.* 2016, 146, 474.
- [47] Goksu, H. *New J. Chem.* 2015, 39, 8498.
- [48] Ma, R. et al. *Ceram. Int.* 2015, 41, 12432.

## **2.3. Copper oxide–graphene oxide nanocomposite: efficient catalyst for hydrogenation of nitroaromatics in water**

### **2.3.1. Introduction**

Catalysts play deterministic roles in the hydrogenation of nitroaromatics to aminoaromatics.<sup>[1–3]</sup> The development of highly active catalysts has attracted remarkable attention for the next-generation green, cost-effective and efficient reduction processes. In particular, the engineered metal nanoparticles (NPs) and nanocomposites have significantly improved the efficiency of catalytic systems. Consequently, various approaches have been utilized to fabricate the inexpensive nanostructured catalysts.<sup>[4–7]</sup> Varma *et al.* has emphasized the importance of the greener methods to synthesize nanocomposite catalysts.<sup>[8]</sup> Virkutyte *et al.* has reviewed various approaches for the fabrication of stable, environmentally benign, and active metal NPs for catalytic applications.<sup>[9]</sup> A summary of nanocatalysts utilized for the environmentally friendly reduction of nitroaromatics has also been reviewed by Zhang and colleagues, emphasizing the advantages of the introduced heterogeneous catalysts.<sup>[10]</sup> However, several drawbacks of the present catalysts need to be circumvented namely enhancing the specific surface area, long-term stability, production cost diminution, and ecological concerns pertaining to their industrial applications.<sup>[11–14]</sup> To fabricate such catalysts possessing the aforementioned competencies, various nanostructured catalysts have been designed and synthesized; <sup>[15–17]</sup> metal NPs have been stabilized on variable robust nanostructures,

producing active nanocomposite catalysts for reduction of nitroaromatics.<sup>[18-20]</sup> These heterogeneous catalysts generally comprise precious metal nanocatalysts *e.g.* Pd, Pt, Rh, Ru *etc.* to achieve efficient hydrogenation of nitroaromatics.<sup>[20-22]</sup> However, they are not broadly utilized in the chemical industries due to their high costs which is critical issue from the economical viewpoint.<sup>[23]</sup> In comparison, earth abundant elements *e.g.* Cu, Co, Fe, Mn, and Ni are inexpensive and may serve as appropriate catalysts for several catalytic transformations, but with low catalytic activity.<sup>[24-26]</sup> The nano-sized counterparts of these catalysts also get aggregated quickly in the reaction media due to their high surface-to-volume ratio, limiting their efficiency and reusability.<sup>[27,28]</sup> Consequently, engineering hybrid catalysts consist of nanocatalysts integrated susceptible supports is necessary to promote their activities. The nanocomposite catalysts often present improved catalytic properties by exhibiting synergetic effects between the supports and nanocatalysts.<sup>[29-31]</sup>

Graphene has been extensively employed as a stable and excellent nanocatalysts support for synthesizing efficient heterogeneous catalysts;<sup>[32,33]</sup> its exceptional conductivity can facilitate the electron transfer during the transformations.<sup>[34]</sup> Consequently, metal nanocatalysts supported on the graphene may potentially promote the reductants' electrons donation in the reaction media enhancing the reduction efficiency. Indeed, the synergetic effect between less-reactive nanocatalysts and graphene leads to highly active hybrid nanocomposite catalysts.<sup>[35]</sup>

Motivated by the aforementioned advantages, we synthesized an efficient nanocomposite catalyst consist of graphene oxide (GO) supported copper oxide NPs (CuO-GO) via a facile hydrothermal self-assembly process for the reduction of nitroaromatics. The CuO-GO nanocomposite catalyst exhibited high yields for the reduction of various nitroaromatics using aqueous sodium borohydride ( $\text{NaBH}_4$ ) at room temperature.

### **2.3.2. Nanocatalyst preparation**

Water was deionized by a Nano Pure System (Barnsted). The reagents used in this research were purchased from SigmaAldrich, Samchun, and Daejung and used without any further purification.

Graphene oxide was synthesized from graphite using the modified hummer's approach.<sup>[36]</sup> Commercial graphite powder (10 g) was added into 230 mL concentrated  $\text{H}_2\text{SO}_4$  and cooled to  $\sim 20^\circ\text{C}$  with a circulator. 300 g potassium permanganate was added while stirring. Then, the temperature of the reaction was adjusted to  $40^\circ\text{C}$  and the mixture was stirred for 1 h. Water (500 mL) was added to the mixture and the temperature was increased to  $100^\circ\text{C}$ . 2.5 mL  $\text{H}_2\text{O}_2$  (30 wt.%) was slowly added to the mixture. For purification, the suspension was washed with HCl solution (200 mL) using a filter and a funnel. The suspension was washed with water several times until the filtrate became neutral.

CuO-GO nanocomposite catalyst was successfully synthesized using

a facile hydrothermal self-assembly process by modifying a previously reported method.<sup>[36]</sup> CuCl<sub>2</sub> (2 mmol) was dissolved in deionized water and mixed with the as-synthesized GO solution (15 mL) and transferred into a clean Teflon-lined container. Thereafter, the Teflon-lined container was filled (70% in volume) with deionized water, placed in an autoclave and tightly sealed, followed by heating up to 150 °C for 12 h. After gradually cooling down, the product was washed with sufficient deionized water and filtered for several times to remove the non- and/or poor-anchored copper oxide NPs on the GO.

### **2.3.3. Materials characterization**

X-ray photoelectron spectroscopy (XPS) was performed using an Al K $\alpha$  source (Sigma probe, VG Scientifics) to characterize the surface chemical composition. The nanostructure of the prepared CuO-GO nanocomposite catalyst was studied using a high resolution X-ray diffraction (XRD, D8-Advance), a transmission electron microscope (TEM, JEOL JEM-3010) equipped with an energy-dispersive X-ray spectroscopy (EDX) detector, a scanning TEM (STEM, JEOL JEM-2100F), a thermal gravimetric analysis (TGA, simultaneous DTA/TGA analyzer), Raman technology (LabRAM HV Evolution), and a Fourier Transform-Infrared Radiation spectroscopy (FT-IR, Nicolet iS50). Gas chromatography-mass spectrometry (GC-MS, Agilent Technologies 7693 Autosampler and 5977A Mass selective detector) was employed to monitor the conversion ratio of the nitroaromatics to aminoaromatics.

#### **2.3.4. Catalytic reduction of nitroaromatics**

The reduction of nitroaromatics to aminoaromatics was carried out using CuO-GO nanocomposite catalyst with aqueous NaBH<sub>4</sub> as a reductant at room temperature. In a typical procedure, nanocomposite catalyst (50 mg) was dispersed in deionized H<sub>2</sub>O (30 ml). Then, a nitroaromatics (1 mmol), NaBH<sub>4</sub> (1.2 mmol) and a small stirring bar were added into the reaction glass flask. The reaction mixture was stirred at room temperature for 30 min under air atmosphere. After completion of the reaction, the CuO-GO nanostructured catalyst was separated using a centrifuge. The yields of the aminoaromatics products were measured using a GC-MS. For the reusability evaluation of the nanocomposite catalyst, the separated catalyst was washed with deionized water and dried in an oven for the following runs. The cycling performance was achieved by repeating the above reduction process.

#### **2.3.5. Results and discussion**

Figure 2.10 depicts the overall synthetic procedure accomplished using a low-cost synthesis for CuO-GO nanocomposite catalyst. The XRD peaks (Figure 2.11a) of the nanocomposite catalyst display are well indexed with GO and CuO (JCPDS Card no. 89-2530). The composition of the catalyst was further characterized by Raman technology to verify the GO support (Figure 2.11b). The G line (first-order scattering of the

$E_{2g}$  phonons of  $sp^2$  orbital) at  $1580\text{ cm}^{-1}$  and D line ( $\kappa$ -point phonons of  $A_{1g}$  symmetry) at  $1350\text{ cm}^{-1}$  are clearly acquired for the nanocomposite catalyst as specific characteristics of graphene.<sup>[37]</sup> The thermal-stability of the catalyst was ascertained using TGA (Figure 1.11c) under the nitrogen atmosphere with a temperature ramp of  $10\text{ }^\circ\text{C min}^{-1}$ , demonstrating the presence of  $\sim 15\text{ wt.}\%$  moisture according to the first weight decrease and  $\sim 45\text{ wt.}\%$  graphene based on the second weight loss. Accordingly, weight percentage ratio of graphene to copper oxide species in the nanocomposite catalysts was found to be  $\sim 1:1$ .



**Figure 2.10.** Schematic illustration for the synthesis of the CuO-GO nanocomposite catalyst.

The composition of the nanocomposite catalyst was further confirmed by FT-IR (Figure 2.11d). A strong peak at  $3450\text{ cm}^{-1}$  (O-H stretching vibrations) in the case of GO indicates  $\text{H}_2\text{O}$  residual compared with CuO-GO nanocomposite catalyst even after sufficient drying. In addition, the characteristic bands of GO are clearly revealed at  $1725\text{ cm}^{-1}$  for C=O stretching vibrations and  $1600\text{ cm}^{-1}$  for C=C (skeletal vibrations of graphene). These peaks disappeared in the



determined the existence of Cu and O elements distribution on GO support (Figure 2.12f).

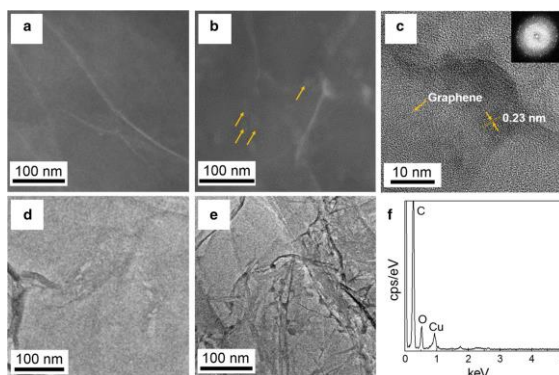


**Figure 2.12.** (a,d) TEM and STEM images of GO. (b,e) TEM and STEM images of the CuO-GO nanocomposite catalyst. (c) HRTEM image of the CuO-GO nanocomposite catalyst. The inset shows the relevant FFT image. (f) EDX spectrum of the CuO-GO nanocomposite catalyst.

The surface composition and existing elements on the nanocomposite catalyst were confirmed by XPS (Figure 2.13). The survey spectrum shows the surface binding situation, ascertaining the presence of Cu, O, and C elements in the nanocomposite catalyst (Figure 2.13b-d). Carbon peaks are deconvoluted into three peaks, where the primary C-C bond generated by  $sp^2$  orbital hybridization shown at 284.6 eV. The oxide graphene is further verified by the C-O bond at 286.2 eV. Cu has binding energy of 944.3 eV (Cu  $2p_{1/2}$ ) and 935.8, 932.8 eV (Cu  $2p_{3/2}$ ) with O 1s possessing binding energy of 530.6 eV thus demonstrating the existence

of copper oxide in the nanocomposite catalyst. The other two peaks with binding energies of 533.2 eV and 531.8 eV can be ascribed to the absorption of water and oxygen molecules from environment. Others deconvoluted peaks with much lower intensities (536.6 eV and 535.8 eV) are the satellite peaks of C.

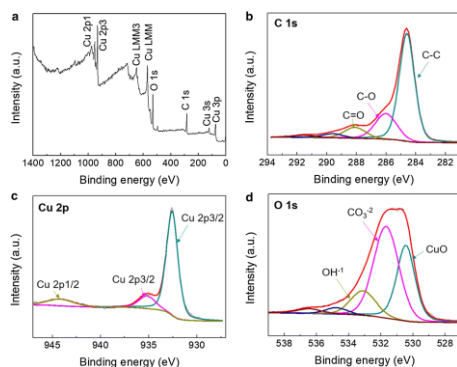


**Figure 2.13.** XPS analysis (a) survey scan, (b) C 1s, (c) Cu 2p, and (d) O 1s for the CuO-GO nanocomposite catalyst.

The catalytic activity of the nanocomposite catalyst was first examined in the reduction of 4-nitrobenzene with aqueous NaBH<sub>4</sub> as a model reaction; high yield of conversion of 4-aminobenzene (98%, Table 2.3) was achieved. Although the selective reduction of a nitro moiety in the nitroaromatic compounds comprising another reducible functional group is a difficult transformation, nanocomposite catalyst selectively reduced the nitro to the amino moiety (Table 2.3, entries 2–7), demonstrating the feasibility of the

synthesized catalyst for broad catalytic reduction applications. The excellent catalytic activity of the catalyst can be ascribed by the synergetic effect between copper oxide NPs and graphene oxide.<sup>[38]</sup> To highlight the catalytic activity of the CuO-GO nanocomposite catalyst in reduction of nitroaromatics, we compared the previously reported articles (Table 2.4) with the current catalyst. The CuO-GO nanocomposite catalyst showed less catalytic activity in comparison with other heterogeneous catalysts having noble-metals *e.g.* Pd, Pt *etc.* However, considering the low price of copper, a competitive catalytic activity was exhibited by the CuO-GO nanocomposite catalyst. Furthermore, the reusability of heterogeneous catalysts is necessary for its pragmatic usages.<sup>[39–45]</sup> The CuO-GO nanocomposite catalyst was successfully reused for six consecutive cycles of the reduction of 4-nitrotoluene with a good yield of 85% (Figure 2.14).

**Table 2.3.** Heterogeneous reduction of substituted nitroaromatics catalyzed by CuO-GO nanocomposite catalyst in aqueous solution.



Entry	Substrate	Product	Yield (%)
1			98
2			97
3			94
4			97
5			92
6			98
7			95

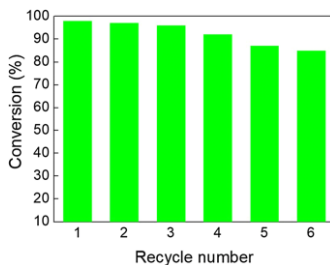


**Figure 2.14.** Reuse of the CuO-GO nanocomposite catalyst in the heterogeneous reduction of 4-nitrotoluene. Reaction conditions: 4-nitrotoluene (1 mmol), NaBH<sub>4</sub> (1.2 mmol), catalyst (50 mg), room temperature, aqueous solution, and 30 min. The yields were determined by GC-MS.

**Table 2.4.** Catalytic comparison study of known heterogeneous catalysts in the reduction of nitrophenol.

Entry	Catalyst	Reductant	Time (min)
1	Graphene–Cu <sub>36</sub> Ni <sub>64</sub>	NH <sub>3</sub> BH <sub>3</sub> (3 mmol)	30 [37]
2	Cu–Ni–AAPTMS@GO	NaBH <sub>4</sub> (1.5 mmol)	4 [38]
3	Ru50Ni50/RGONCs	NH <sub>3</sub> BH <sub>3</sub> (2 mmol)	4.5 [39]
4	Pt/RGO	H <sub>2</sub> (1 MPa)	120 [40]
5	(Co <sub>6</sub> )Ag <sub>0.1</sub> Pd <sub>0.9</sub> /RGO	HCOONH <sub>4</sub> (4 mmol)	20 [41]
6	Pd/GO	NaBH <sub>4</sub> (1.2 mmol)	10 [42]
7	MRN–Pd	NaBH <sub>4</sub> (1.2 mmol)	45 [43]
8	CuSO <sub>4</sub> /GO	NaBH <sub>4</sub> (1.2 mmol)	30 [This work]

### 2.3.6. Conclusions

Small copper oxide NPs (~10 nm) formed nanocomposite with graphene oxide by a facile and cost-efficient hydrothermal self-assembly approach. Although GO and CuO NPs separately showed low catalytic activities in the reduction of nitroaromatics, their composite presented excellent reduction performance with high yield and selectivity for the conversion of various nitroaromatics bearing different functional groups, which can be described by the synergetic effect. In addition, the nanocomposite catalyst could be recycled for up to six uses. This

system can be a promising heterogeneous catalyst for the future reduction of nitroaromatics premeditated in large scale wherein the low-cost and facile fabrication are demanded.

### 2.3.7. References

- [1] Zeng, T. et al. *Appl. Catal. B-Environ.* 2013, 134, 26.
- [2] Shokouhimehr, M. et al. *Chem. Commun.* 2013, 49, 4779.
- [3] Shokouhimehr, M. et al. *Appl. Catal. A Gen.* 2014, 476, 133.
- [4] Gawande, M. B. et al. *Chem. Soc. Rev.* 2013, 42, 5522.
- [5] Choi, K. H. et al. *Bull. Korean Chem. Soc.* 2013, 34, 1195.
- [6] Polshettiwar, V. et al. *Green Chem.* 2010, 12, 743.
- [7] Shokouhimehr, M. et al. *Res. Chem. Intermed.* 2018, 44, 1617.
- [8] Varma, R. S. *Curr. Opin. Chem. Eng.* 2012, 1, 123.
- [9] Virkutyte, J. et al. *Chem. Sci.* 2011, 2, 837.
- [10] Zhang, K. et al. *ACS Omega* 2019, 4, 483.
- [11] Hu, Y. et al. *J. Phys. Chem. C* 2013, 117, 8974.
- [12] Shokouhimehr, M. et al. *Synlett.* 2006, 04, 618.
- [13] Hagen, J. *Industrial Catalysis: a Practical Approach*, Wiley-VCH (2006).
- [14] Shokouhimehr, M. *Catalysts* 2015, 5, 534.
- [15] Nasir Baig, R. B. et al. *Green Chem.* 2013, 15, 398.
- [16] Verho, O. et al. *ChemCatChem* 2014, 6, 3153.

- [17] Lu, Y. M. et al. *J. Mater. Chem. A* 2013, 1, 3783.
- [18] Kuroda, K. et al. *J. Mol. Catal. A* 2009, 298, 7.
- [19] Dong, Z. et al. *Appl. Catal. B* 2014, 158, 129.
- [20] Dong, Z. et al. *J. Ma, Appl. Catal. B* 2015, 162, 372.
- [21] Kim, A. et al. *Energy Environ. Focus* 2015, 4, 18.
- [22] Lee, I. et al. *Chin. J. Catal.* 2015, 36, 1799.
- [23] He, S. et al. *ChemistrySelect* 2016, 1, 2821.
- [24] Karthik, M. et al. *ChemistrySelect* 2017, 2, 6916.
- [25] Wu, Y. G. et al. *J. Phys. Chem. C* 2014, 118, 6307.
- [26] Tang, B. et al. *RSC Adv.* 2017, 7, 1531.
- [27] Zhang, N. et al. *Mater.* 2013, 25, 1979.
- [28] Kadam, R. G. et al. *ChemPlusChem* 2015, 82, 467.
- [29] Wu, Z. S. et al. *J. Am. Chem. Soc.* 2012, 134, 9082.
- [30] Liang, Y. et al. *Nat. Mater.* 2011, 10, 780.
- [31] Shi, J. *Chem. Rev.* 2013, 113, 2139.
- [32] El-Hout, S. I. et al. *Appl. Catal. A Gen.* 2015, 503, 176.
- [33] Cheng, Y. et al. *Catal. Sci. Technol.* 2015, 5, 3903.
- [34] Ma, B. et al. *Catal. Sci. Technol.* 2017, 7, 2805.
- [35] Goswami, A. et al. *ACS Appl. Mater. Interfaces* 2017, 9, 2815.
- [36] Hummers, W. S. et al. *J. Am. Chem. Soc.* 1958, 80, 1339.
- [37] Beams, R. et al. *J. Phys. Condens. Mat.* 2015, 27, 083002.
- [38] Sarkar, C. et al. *RSC Adv.* 2015, 5, 60763.

- [39] Choi, K. H. et al. *Bull. Korean Chem. Soc.* 2013, 34, 1477.
- [40] Zhang, K. et al. *Res. Chem. Intermed.* 2019, 45, 599.
- [41] Shokouhimehr, M. et al. *Green Chem.* 2018, 40, 3809.
- [42] Rafiaei, S. M. et al. *Nanosci. Nanotech. Let.* 2014, 6, 309.
- [43] Shokouhimehr, M. et al. *J. Mater. Chem. A* 2014, 2, 7593.
- [44] Laali, K. K. et al. *Curr. Org. Chem.* 2009, 6, 193.
- [45] Moon, C. W. et al. *RSC Adv.* 2018, 8, 18442.

## **Acknowledgments**

Thank my advisors professor Jang Ho Won, professor Choi Ji-Won, and professor Mohammadreza Shokouhimehr and their valuable advising and supporting during the Ph.D course. My academic capabilities including writing papers, designing and proceeding experiments have been greatly improved, which will be extremely helpful for future research career. I would like to thank the whole lab members in both Seoul National University and Korea Institute of Science and Technology for having a pleasant experience with them. In addition, I also want to thank the instrument operators in different characterization centers of Seoul National University and Korea Institute of Science and Technology. During my Ph.D course, their professional techniques assist to my analysis on experimental results. Finally, I would like to thank again my advisors, professor Jang Ho Won, professor Choi Ji-Won, and professor Mohammadreza Shokouhimehr for their full support and valuable instructions, which will be an important part of my life experience. I am grateful to the Seoul National University and Korea Institute of Science and Technology give me a wonderful experience.

## **List of Publications**

1. K. Zhang, T. H. Lee, H. W. Jang, M. Shokouhimehr and J.-W. Choi, *Electronic Materials Letters* 15, 444–453 (2019).
2. K. Zhang, R. S. Varma, H. W. Jang, J. W. Choi and M. Shokouhimehr,

Journal of Alloys and Compounds 791, 911–917 (2019).

3. K. Zhang, T. H. Lee, B. Bubach, M. Ostadhassan, H. W. Jang, J.-W. Choi and M. Shokouhimehr, RSC Advances 9, 21363–21370 (2019).
4. K. Zhang, T. H. Lee, H. Noh, T. Islamoglu, O. K. Farha, H. W. Jang, J.-W. Choi and M. Shokouhimehr, ACS Applied Materials & Interfaces 11, 31799–31805 (2019).
5. M. Shokouhimehr, K. Hong, T. H. Lee, C. W. Moon, S. P. Hong, K. Zhang, J. M. Suh, K. S. Choi, R. S. Varma and H. W. Jang, Green Chemistry 20, 3809–3817 (2018).
6. K. Zhang, J. M. Suh, J. W. Choi, H. W. Jang, M. Shokouhimehr and R. S. Varma, ACS Omega 4, 483–495 (2019).
7. K. Zhang, K. Hong, J. M. Suh, T. H. Lee, O. Kwon, M. Shokouhimehr and H. W. Jang, Research on Chemical Intermediates 45, 599–611 (2019).
8. K. Zhang, J. M. Suh, T. H. Lee, J. H. Cha, J.-W. Choi, H. W. Jang, R. S. Varma and M. Shokouhimehr, Nano Convergence 6, 6 (2019).
9. M. Shokouhimehr, K. Hong, T. H. Lee, C. W. Moon, S. P. Hong, K. Zhang, J. M. Suh, K. S. Choi, R. S. Varma and H. W. Jang, Synfacts 14, 1209 (2018).
10. K. Zhang, T. H. Lee, B. Bubach, H. W. Jang, M. Ostadhassan, J.-W. Choi and M. Shokouhimehr, RSC Advances 9, 26668–26675 (2019).

11. K. Zhang, T. H. Lee, B. Bubach, H. W. Jang, M. Ostadhassan, J.-W. Choi and M. Shokouhimehr, *Scientific Reports* 9, 1–9 (2019).
12. K. Zhang, T. H. Lee, J. H. Cha, R. S. Varma, J.-W. Choi, H. W. Jang and M. Shokouhimehr, *Scientific Reports* 9, 1–10 (2019).
13. K. Zhang, T. H. Lee, J. H. Cha, H. W. Jang, J.-W. Choi, M. Mahmoudi and M. Shokouhimehr, *Scientific Reports* 9, 1–8 (2019).
14. K. Zhang, T. H. Lee, J. H. Cha, H. W. Jang, M. Shokouhimehr and J.-W. Choi, *Electronic Materials Letters* 1-7 (2019).
15. K. Zhang, T. H. Lee, J. H. Cha, H. W. Jang, M. Shokouhimehr and J.-W. Choi, *Electronic Materials Letters* 1-6 (2019).
16. K. Zhang, J. M. Suh, A. Kim, H. W. Jang, J.-W. Choi, R. S. Varma and M. Shokouhimehra, *Renewable & Sustainable Energy Reviews*, Revision submitted.
17. K. Hong, M. Sajjadi, J. M. Suh, K. Zhang, A. Kim, M. Nasrollahzadeh, H. W. Jang, R. S. Varma and M. Shokouhimehr, *ACS Sustainable Chemistry & Engineering* Submitted.
18. K. Zhang, T. H. Lee, J. H. Cha, H. W. Jang, J.-W. Choi, R. S. Varma and M. Shokouhimehr, *ACS Omega*, Submitted.
20. K. Zhang, T. H. Lee, O. K. Farha, H. W. Jang, J.-W. Choi and M. Shokouhimehr, *ACS Crystal Growth & Design*, submitted.

## Abstract (in Korean)

---

이 논문은 다양한 합성 방법과 특성화 전략을 사용하여 니트로 텐을 아미노 아렌으로 수소화하기 위한 나노 촉매 및 전기 화학 에너지 저장 응용을 위한 전극의 재료 설계 및 합성을 제시합니다.

산업용 제품에서 효율적인 화학적 전환을 위해 촉매가 끊임없이 연구되고 있으며 저렴한 비용 효율성을 갖춘 녹색 및 손쉬운 방법을 통한 고도의 활성 및 선택적 불균일 나노 촉매의 개발은 어려운 제안이었습니다. 산화 그래핀 (GO) 상에 산화 구리 (CuO) 나노 입자를 함유하는 저비용의 나노 복합체 촉매를 용이 한 열수 자기 조립 공정에 의해 제조 하였다. 분리 된 CuO NP 및 GO는 니트로 방향족의 감소를 위해 무시할만한 촉매 활성을 나타냈다. 그러나, 그들의 하이브리드 복합물은 NaBH<sub>4</sub> 수용액에서 여러 치환 된 니트로 방향족에 대한 높은 전환율로 용이 한 감소를 달성 하였다; 나노 복합체 촉매에서 CuO NP와 GO의 상승적 결합 효과는 우수한 촉매 활성을 제공 하였다. 나노 복합체 촉매는 반응 혼합물로부터 분리되어 연속적으로 재순환 될 수 있다.

더욱이, 본 발명자들은 단순하고 녹색 인 공정을 통해 GO-

지지 된 팔라듐 NP의 재현 가능한 불균일 촉매를 합성 하였다. 합성 된 이중 촉매의 구조, 형태 및 물리 화학적 특성은 고해상도 투과 전자 현미경, 주사 투과 전자 현미경, 에너지-분산 X-선 분광법, X-선 회절 분석 및 X-와 같은 최신 기술에 의해 특징 지워졌다. 광선 광전자 분광법. GO-지지 된 Pd NP (Pd/GO 나노 촉매)는 수성 나트륨 보로 하이드 라이드에서 니트로 방향족을 아미노 방향으로 환원시키기 위한 우수한 촉매 활성을 나타냈다. 니트로 방향족은 수용액에서 Pd/GO 나노 촉매를 사용하여 높은 수율 (최대 99%)로 상응하는 아미노 방향으로 전환되었다. 하이브리드 불균일 촉매는 니트로 벤젠에서 아미노 벤젠으로의 환원에서 6 회 사이클 후 전환의 83%를 나타냈다. 이들 특징은 도입 된 산화 그래핀 지지 된 Pd 나노 촉매의 높은 촉매 활성을 보장 하였다.

요구되는 지속 가능성과 환경 친 화성을 달성하기 위해 풍력 에너지 및 태양 에너지와 같은 청정 에너지 원을 사용하는 것은 현재의 화석 연료 에너지 위기를 해결하기 위한 한 가지 가능한 솔루션입니다. 그러나, 재생 에너지의 산발적인 품질은 현재 청정 에너지 자원의 사용에 있어 일반적인 장애물이다. 이 문제를 해결하기 위해 전기 화학 배터리 및 커패시터는 안정적인 전원 공급을 위한 유용한 솔루션으로 간주되었습니다. 따라서, 습식 화학 법을 통해 합성 된 나노 물질에 중점을두고 Li-이온 배터리, Li-이온 커패시터 및 Al-

이온 배터리의 응용을 위한 여러 에너지 저장 물질이 소개되었다.

리튬 이온 배터리는 대규모 에너지 저장 및 변환 시스템과 관련하여 이론적으로 유망한 것으로 간주된다. 그러나 중요한 문제는 LIB를 위한 비용 효율적인 고성능 음극 재료가 부족하다는 것입니다. 프러시안 블루 유사체 (PBA)는 리튬 이온 배터리의 매력적인 전극 재료 후보이며, 조정 가능한 기공 크기 및 흥미로운 전기 화학적 특성으로 인해 상당한 관심을 받고 있다.

헥사시 아나이드 링커로 형성된 PBA는 수십 년 동안 연구되어 왔다. PBA의 골격 결정 구조는 주로 6 배 배위의 시아 노 작용기로부터 유리하다. In-plane tetracyanonickelate는 유기 링커를 설계하고 4 배의 조율 된 PBA (FF-PBA;  $\text{Fe}^{2+}\text{Ni}(\text{CN})_4$ ,  $\text{MnNi}(\text{CN})_4$ ,  $\text{Fe}^{3+}\text{Ni}(\text{CN})_4$ ,  $\text{CuNi}(\text{CN})_4$ ,  $\text{CoNi}(\text{CN})_4$ ,  $\text{ZnNi}(\text{CN})_4$  및  $\text{NiNi}(\text{CN})_4$ ). 이 FF-PBA는 Li-이온 배터리의 음극 재료로 사용될 수 있으며, Ni/Fe<sup>2+</sup> 시스템은 100 mA g<sup>-1</sup> 에서 137.9 mA hg<sup>-1</sup>의 용량으로 다른 시스템에 비해 우수한 전기 화학적 특성을 나타 냈습니다. 또한, 5000 사이클의 장기간 반복 된 충 방전 측정 후, Ni/Fe<sup>2+</sup> 시스템은 전류 밀도 1000 mA g<sup>-1</sup>에서 쿨롱 효율 98.8%로 60.3 mA hg<sup>-1</sup>의 용량을 나타냈다. 또한, 86.1%의 용량은 100 mA g<sup>-1</sup>에서의 용량과 비교하여 1000 mA g<sup>-1</sup>에서 보존되었으며, 이는 양호한 속도 성능을 암시한다.

이러한 잠재적인 용량은 X-XRD 특성에 따라 호스트 물질로 다른 화합물을 형성하는 대신 Ni/Fe<sup>2+</sup>의 중간층에서 Li<sup>+</sup>의 인-시튜 환원에 기인 할 수 있다. 이러한 특수 설계된 FF-PBA는 전기 화학 및 2D 재료를 필요로 하는 기타 응용 분야에서 새로운 개념에 영감을 줄 것으로 기대됩니다.

그 후, 국경이 풍부한 철 (Fe<sup>3+</sup>) 헥사시 아노 코발 테이트 (FeHCCo) PBA를 용이하고 저렴한 공 침법을 통해 합성하고 LIB의 캐소드 물질로서 평가한다. PBA는 각각 0.63 및 6.25 °C에서 136 및 57 mAh g<sup>-1</sup>에 상응하는 가역 용량을 제공 하였다. 또한, 1.25 °C에서 116 mAh g<sup>-1</sup>의 리튬 화 용량을 99.6 %의 쿨롱 효율로 유지시켰다. 높은 전기 화학적 성능은 경계가 풍부한 FeHCCo의 가역적인 개방 프레임 워크 결정 텍스처에 기인 할 수 있으며, 이는 재충전 가능한 LIB에서 실용적인 전극 재료로서 PBA를 적용하는 것에 대한 새로운 통찰력을 제공 할 수 있다.

또한, LIB 용 저비용 및 고성능 캐소드 물질로서 PBA, 아연 헥사시 아노 코발 테이트 (ZnHCCo). ZnHCCo의 오픈 프레임 워크 결정 구조는 호스트의 자발적 원자가 변화와 함께 가역적 양이온 삽입 및 추출에 기여합니다. 구체적으로, 제조 된 ZnHCCo는 1.25C의 전류 밀도에서 121.5 mAh g<sup>-1</sup>의 높은 가역 용량, 6.25C에서 60.5 mAh g<sup>-1</sup>의 우수한 속도 용량, 및 쿨롱

효율의 안정적인 사이클링 안정성을 나타낸다. 96.5%. 따라서, 잘 결정화되고 저렴한 ZnHCCo는 그리드-스케일 에너지 저장 및 변환 시스템에 사용되는 LIB의 잠재적인 캐소드 물질 일 것으로 예상된다. 또한, 전극 물질의 합성 공정은 상온 습식 화학 법을 통해 지구 풍부하고 환경 친화적인 전구체를 사용하여 용이하게 스케일 업될 수 있다.

알루미늄 이온 배터리 (AIB)는 다른 금속 이온 배터리와 비교할 수 있는 가연성 및 전기 화학적 성능이 없기 때문에 리튬 이온 배터리의 유망한 후보로 간주됩니다. 그러나, 적절한 캐소드 물질의 부족은 고성능 AIB의 개발을 방해했다.

우리는 원소 금속 NP의 AIB에 대한 음극 재료로서의 호환성을 시연했다. 현장에서 성장하는 PBA ( $\text{Co}[\text{Co}(\text{CN})_6]$ ,  $\text{Fe}[\text{Fe}(\text{CN})_6]$  및  $\text{Co}[\text{Fe}(\text{CN})_6]$ )에 의해 3 가지 유형의 금속 NP ( $\text{Co}@C$ ,  $\text{Fe}@C$ ,  $\text{CoFe}@C$ )가 형성되었습니다. 수성 조에서 실온 습식 화학 법에 의해 천연 수세미 (L)에 이어서 탄화 공정으로 수행 하였다. 사용 된 L은 열처리 후 흑연 C-캡슐화 된 금속 NP를 효과적으로 형성 하였다.  $\text{CoFe}@C$ 의 방전 용량은 다른 것보다 우수했다 ( $372 \text{ mAh g}^{-1}$ ) ( $\text{Co}@C$ 의 경우  $103 \text{ mAh g}^{-1}$ ,  $\text{Fe}@C$ 의 경우  $75 \text{ mAh g}^{-1}$ ). 새로운 디자인으로  $\text{CoFe}@C$ 는 쿨롱 효율이 94.1% 인 뛰어난 장기 충전/방전 사이클링 성능 (1,000 회 이상)을 제공합니다. Ex-situ X-ray 회절 연구에 따르면

이러한 금속 NP 용량은 고체 확산 제한 AI 저장 공정을 통해 달성됩니다.

전극 물질로서 금속 산화물을 사용하는 것은 리튬-이온 배터리에서 큰 성공을 거두었다. 그러나, 이러한 유형의 전극 재료는 황화물 및 셀레 나이드와 비교하여 재충전 가능한 AIB에 대한 부적절한 옵션으로 여겨져서 거의 버려졌다. 여기, 우리는 AI 이온 저장에 대한 높은 전기 화학적 활동을 보여주는 AIBs의 음극 재료로 금속 산화물의 적합성을 보여줍니다. AIB를 위해 경제적인 금속 산화물 음극 ( $\text{Co}_3\text{O}_4@\text{rGO}$ ,  $\text{Fe}_2\text{O}_3@\text{rGO}$  및  $\text{CoFe}_2\text{O}_4@\text{rGO}$ )을 설계했습니다.  $\text{Co}_3\text{O}_4@\text{rGO}$ 는 과학 문헌에 의해 보고된 현재의 최신 캐소드 물질에 대해 용량 및 수명 모두에 대해 우수한 전기 화학적 특성을 나타냈다. 또한,  $\text{CoFe}_2\text{O}_4@\text{rGO}$ 는 합리적인 전기 화학 용량과 99.6%의 우수한 쿨롱 효율로 매우 안정적인 충 방전 공정을 보여줍니다. 제안된 연구는 연구원들이 고성능 AIB를 위한 경쟁 캐소드 재료로서 간과된 금속 산화물에 집중하도록 자극 할 것으로 기대합니다.

황은 전기 화학 특성이 뚜렷한 비용 효율적인 재료이며 AIB의 매력적인 음극 재료로 간주됩니다. 여러 선구적인 보고서에 따르면 알루미늄-황 배터리 (ASB)는 AIB의 다른 음극 재료보다 우수한 전기 화학 용량을 나타냅니다. 그러나

용량의 급격한 감소는 실제 애플리케이션에 큰 장애가됩니다. 여기서, 2 차원 층상 물질 (예를 들어,  $\text{MoS}_2$ ,  $\text{WS}_2$  및  $\text{BN}$ )이 반복 된 충전/방전 공정 동안 S 및 황화물 화합물의 정착제로서 작용할 수 있다는 것을 체계적으로 입증 하였다;  $\text{BN/S/C}$ 는 현재 AIB 용 최신 음극 재료와 비교하여  $532\text{mAh g}^{-1}$  (전류 밀도  $100\text{mA g}^{-1}$ )의 최고 용량을 표시합니다. 또한 우리는 94.3%의 높은 쿨롱 효율로 ASB의 수명을 전례없는 300 주기로 향상시킬 수있었습니다. 반복 된 충 방전 사이클 동안  $\sim 1.15\text{ V}$  에서의 방전 안정기가 명확하게 관찰되었다. 우리는이 작업이 고성능 ASB를 달성하기위한 새로운 방법을 열었다 고 생각합니다.

금속 이온 배터리 외에도 금속 이온 커패시터는 또 다른 새로운 문제입니다. 1 회 충전 장기 응용 제품에는 에너지 밀도가 우수한 리튬 이온 저장 커패시터가 중요합니다. 현재, 많은 연구 노력이 하이브리드 Li-이온 커패시터의 에너지 밀도를 향상시키는 데 주력하고 있으며, 여기에는 Li-이온 슈퍼 커패시터의 높은 전력 밀도와 기존의 Li-이온 배터리의 높은 에너지가 통합되어있다. 여기에서, 우리는 새로운 PBA로서 사방 정계  $\text{GdCo}(\text{CN})_6$ 를 준비하여, 이 화합물이 우수한 에너지/전력 밀도 (각각  $605\text{ Wh kg}^{-1}$  및  $174\text{ W kg}^{-1}$ )를 제공하고 Li-이온 저장 용량 (352 및 하이브리드 리튬 이온 커패시터에 사용되는 다른 캐소드 물질보다 거의 두 배 높은

100 및 1,000 mA g<sup>-1</sup>에서 각각 258 mAh g<sub>electrode</sub><sup>-1</sup>. 따라서, GdCo(CN)<sub>6</sub>에 대한 연구는 새로운 유형의 PBA를 탐색하기 위한 새로운 문을 열뿐만 아니라 에너지 저장 분야에서 란타나 이드의 사용에 대한 통찰력을 제공합니다.

**키워드:** 나노 촉매, 환원, 금속 이온 배터리, 금속 이온 커패시터, 습식 화학, 프러시안 블루 아날로그, 금속 산화물, 황, 층상 물질, 란타나 이드.

학번: 2017-33502

장개강